

# Injection molding of microfeatured polymer components

Doctoral Dissertation by

*TERJE ROSQUIST TOFTEBERG*

Submitted to the Faculty of Mathematics and Natural Sciences at the  
University of Oslo in partial fulfilment of the requirements for the degree  
Philosophiae Doctor (PhD)

2009



© Terje Rosquist Tofteberg, 2010

*Series of dissertations submitted to the  
Faculty of Mathematics and Natural Sciences, University of Oslo  
No. 937*

ISSN 1501-7710

All rights reserved. No part of this publication may be reproduced or transmitted, in any form or by any means, without permission.

Cover: Inger Sandved Anfinssen  
Printed in Norway: AiT e-dit AS.

Produced in co-operation with Unipub.  
The thesis is produced by Unipub merely in connection with the thesis defence. Kindly direct all inquiries regarding the thesis to the copyright holder or the unit which grants the doctorate.

---

“There’s Plenty of Room at the Bottom”

*Richard P. Feynman*

---

# ABSTRACT

During the 20<sup>th</sup> century, injection molded parts went from non-existence to omnipresence. From LEGO to DVDs, from cell phone covers to ketchup bottles, polymers are finding novel applications and are replacing other materials. Injection molding is a rapid method for mass production of plastic parts. The main focus of this thesis is how the injection molding process can be used to replicate microscale features (0.1  $\mu\text{m}$  – 100  $\mu\text{m}$ ).

We have worked together with Norwegian industry and SINTEF ICT in the development of new optical sensors and lab-on-a-chip platforms. Products that would not have been commercially realizable without accurate replication of polymer microfeatures. An original design for a microfluidic mixer is presented, especially tailored for rapid replication using injection molding. The mixer has been shown to effectively laminate streams of different fluids both numerically and experimentally.

This thesis investigates in detail how the injection molding conditions, such as the mold temperature, injection speed and cavity pressure influence the replication of microfeatures. A new method has been developed for rapidly assessing the replication quality of optical gratings. Using this method it was seen that a high injection velocity and a high mold temperature are beneficial for microfeature replication. A high holding pressure can have both positive and negative effects on the replication of optical gratings. The results in this thesis indicate that the negative effect is due to elastic recoil after the holding pressure has been released.

A novel simulation method for the injection molding filling phase has been developed, coupling the macroscale polymer flow with the filling of the smallest structural details. The simulations capture well how changes in mold temperature and injection velocity influence the replication.



# PREFACE

This thesis is based on results obtained during a five year project (2005 – 2009) regarding microfeatured polymer components. The project was funded by the Research Council of Norway as a Strategic Institute Program and run by SINTEF Materials and Chemistry. The project addresses challenges regarding the use of thermoplastic polymers in high-precision mass-produced components, based on input from industry and R&D institutions. Focus is on components with the largest outer dimension in the centimeter range, but with features (e.g. channels and optical structures) typically 3 – 4 orders of magnitude smaller than this, i.e. down to about 1 micrometer.

I entered the project in the fall of 2006 with a PhD scholarship and have spent the last three years at SINTEF Materials and Chemistry in Oslo working full time with it. My supervisors have been professor Hans Petter Langtangen at the University of Oslo and senior scientist Erik Andreassen at SINTEF Materials and Chemistry. The papers that constitute the main part of this thesis are given in Part II. Part I is an introduction which places the articles into context. In the first section, present and some possible future applications of microfeatured polymer components will be presented. An overview is also given of the injection molding process, characterization methods and simulation tools needed to understand the injection molding of microfeatured polymer components.

Oslo, December 2009  
Terje Rosquist Tofteberg



# ACKNOWLEDGEMENTS

Thanks to all the people who have contributed to this thesis. Even though this thesis is an individual work, it would never have been realized in the present form without fruitful input from many colleagues.

Especially, I would like to express my gratitude to Erik Andreassen whose office door has always been open for me. His accurate way of working has inspired me and he has been a great supervisor. I would also like to thank Hans Petter Langtangen whose occasional bursts of enthusiasm were much appreciated.

Thanks to research team leader Einar Hinrichsen for truly letting me feel part of the research team, to Frode Grytten for being a great sparring partner on mathematics and parenting, to Mariusz Blochowiak for rheology measurements and for always being ready for a challenging discussion, to H el ene Am edro for your accurate and truly valuable characterization work and to Susie Jahren for helping me with my English and for making work more cheerful. I have had the pleasure of sharing office with Jakub Kalus and Hamid Daiyan and would like to thank you both for being splendid company.

During the fall 2008, I spent two months at the Danish Polymer Center where Henrik K. Rasmussen welcomed me warmly into his group. I appreciate the hospitality of all the people in the department and especially Maciej Skolimowski, who accompanied me to the PPS conference in Goa, India.

Thanks to Michal Mielnik and Liv Furuberg from SINTEF ICT and Anja Gulliksen from NorChip for involving me in exiting projects on microfluidics and medical diagnostics and to Odd L ovhaugen and Matthieu Lacolle from SINTEF ICT and Nils Ragnar Liholt from OptoSense for introducing me to novel applications of diffractive optics.

I am grateful to all my friends and family who have supported me throughout the work with this thesis.

Most of all I would like to thank my lovely wife Hannah and my son Elliot. The two of you make my life complete and have helped putting the work with this thesis in the right perspective.



# LIST OF PAPERS

This thesis includes the following papers, referred to by capital letters in the text:

- A** Terje Tofteberg, H el ene Am edro and Erik Andreassen  
*Injection molding of a diffractive optical element*  
Polymer Engineering & Science, Volume 48, 2134 – 2142 (2008)
- B** Terje Tofteberg, Maciej Skolimowski, Erik Andreassen and Oliver Geschke  
*A novel passive micromixer: lamination in a planar channel system*  
Microfluidics and Nanofluidics, Volume 8, 209 – 215 (2010)
- C** Terje R. Tofteberg and Erik Andreassen  
*Multiscale Simulation of Injection Molding of Parts with Low Aspect Ratio Micro-features*  
International Polymer Processing, Volume 25, 63 – 74 (2010)
- D** Michal M. Mielnik, Ib-Rune Johansen, Terje R. Tofteberg, Britta G. Fismen, Erik Andreassen, Dag Aussen, Lutz Riegger, Peter Koltay, Roland Zengerle, Anja Gulliksen, Lars A. Solli, Frank Karlsen, Petter Gr onn, Rainer Gransee, Tobias Baier, Thomas Hansen-Hagge, Helen Keegan, Cara Martin, John O’Leary and Liv Furu-berg  
*A microfluidic platform for fluorescence-based multi-target biochemical assays*  
(Submitted for possible journal publication 2009)
- E** Erik Andreassen, Terje R. Tofteberg and Mariusz Blochowiak  
*New data testing the universality of chain dynamics in polymers*  
(Submitted for possible journal publication 2009)
- F** Terje R. Tofteberg, H el ene Am edro, Frode Grytten and Erik Andreassen  
*Effects of injection molding holding pressure on the replication of surface micro-features*  
Accepted for publication in International Polymer Processing (2010)



# CONTENTS

PART I	INTRODUCTION	3
1	THESIS TITLE	5
2	APPLICATIONS	7
2.1	Microfluidics.....	7
2.2	Microoptics.....	10
3	INJECTION MOLDING	13
3.1	The injection molding process .....	13
3.2	Polymer materials .....	17
3.3	Mold making .....	20
4	SURFACE CHARACTERIZATION	23
4.1	White light interferometry .....	23
4.2	Scanning electron microscopy .....	25
4.3	Atomic force microscopy .....	26
5	FILLING SIMULATIONS	29
5.1	Model description .....	29
5.2	Simulation conclusions .....	35
6	CONCLUSIONS	37
	BIBLIOGRAPHY	39
PART II	INCLUDED PAPERS	41
	PAPER A	43
	PAPER B	55
	PAPER C	65
	PAPER D	81
	PAPER E	93
	PAPER F	99



# PART I

## INTRODUCTION



# 1 THESIS TITLE

The title of this thesis is “Injection molding of microfeatured polymer components”.

**Injection molding** is a manufacturing process used to form objects by first heating a molding material to a fluid state and then injecting it into a mold. All the parts produced in this work are either made using injection molding or designed with injection molding in mind. The reason why injection molding is not exclusively used, is because the one time cost for the mold is relatively large. Hence, injection molding is usually not cost effective for series consisting of less than thousand items.

**Microfeatured** is an adjective referring to something with microfeatures. In this work a microfeature is a feature with at least two dimensions in the  $\mu\text{m}$ -range (100 nm – 100  $\mu\text{m}$ ). This means that parts with features where only one dimension is in the  $\mu\text{m}$ -range, such as thin films or coatings, are excluded. It does, however, not say anything about the overall size of the injection molded parts. The typical size range of the parts described in this thesis is in the centimeter range.

A polymer is a macromolecule consisting of a large number of repeating subunits linked by covalent chemical bonds. When referring to **polymer components** in this work, it means parts made in a polymer material. A polymer material mainly consists of polymer molecules but may in addition include other non-polymeric additives.



## 2 APPLICATIONS

Polymer materials have been seen as ideal candidates for replicating microfeatures since at least the middle of the 20th century. In the talk “There’s plenty of room at the bottom” held at Caltech in 1959, Richard P. Feynman suggested how the entire Encyclopædia Britannica could be printed on the tip of a needle, letter by letter, for then to be replicated in a polymeric material [1]. Not using binary code, but by plainly downscaling the font, this would require letters written with a line width of 8 nm. Using injection molding, it has been shown that fibrillar structures with details down to 10 nm can be successfully replicated [2]. At least in some special cases, replicating this famous encyclopedia at the tip of a needle could be possible using today’s industrial polymer processing techniques.

Optical storage media, such as the CD, DVD and Blu-Ray Disc, are used to store data densely on a microfeatured polymer substrate. These are fabricated using replication techniques at a very low cost per unit. The dimensions of the features that can be fabricated in polymers are still decreasing. A recent study has reported a storage density of 10 Terabit per square inch [3]. This compares well with the around 10 Gigabit per square inch on a single layer Blu-Ray Disc. The limit for how densely data is stored on a optical disc is not determined by how densely information can be packed on the polymer surface, but rather the density which can be read out using consumer lasers.

In this section, it will be discussed how microfeatured polymer components can be used in other high value/low cost applications. A change in the topography can for example be used to alter the physical properties of the surface. By introducing a microscale pattern, the effective surface area of a substrate can be increased by orders of magnitude. Inspired by the structure of the Lotus leaf, this can be used to produce superhydrophobic surfaces [4]. Potential applications of such structures include self cleaning, anti-icing and anti-bacterial surfaces. Also mimicking nature, by reproducing the sub-wavelength structure found on the cornea of the night-flying moths, it is possible to make almost perfect anti-reflective surfaces [5], applicable in many optical applications.

### 2.1 Microfluidics

In a recent overview article, George M. Whitesides defines microfluidics as “... the science and technology of systems that process or manipulate small ( $10^{-9}$  to  $10^{-18}$  liters) amounts of fluids, using channels with dimensions of tens to hundreds of micrometers” [6]. Replicating features at this size, and also much smaller, is possible using injection molding. One promising application of microfluidics, is so called, lab-on-a-chip applications. As the name implies, this involves downscaling of laboratory functionality to the

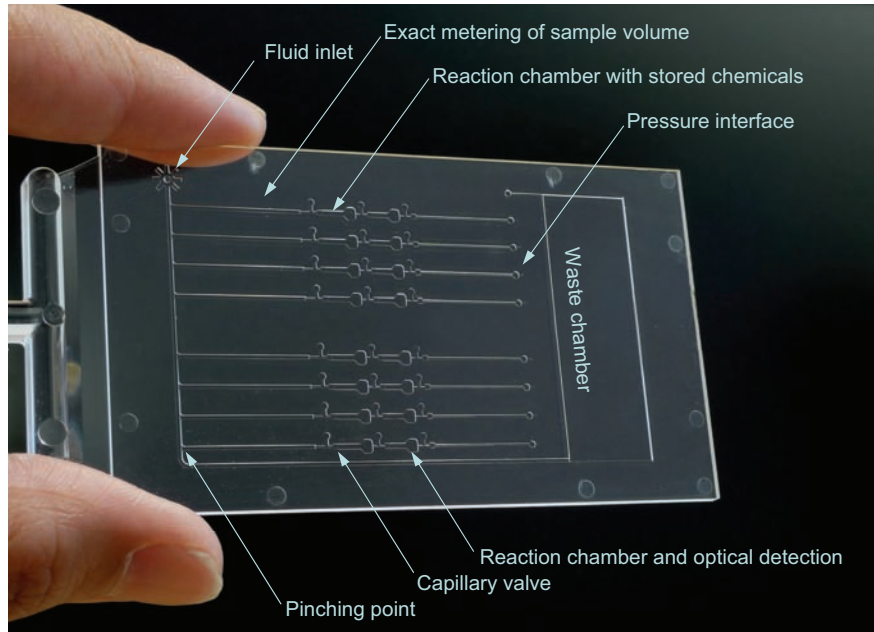


Figure 2.1: Photo of the NASBA chip, a lab-on-a-chip device molded as part of this work and described in detail in Paper D. The specific chip shown is used to simultaneously detect eight different strands of the human papilloma virus, which are linked to the onset of cervical cancer. The photo has been altered to demonstrate the working principle of the chip.

chip level. Depending on the specific application, some of the typical advantages are:

1. Smaller fluid volumes mean less waste, lower chemical costs and smaller sample volumes.
2. Faster response time thanks to smaller thermal mass and shorter diffusion times, gives faster analysis and better process control.
3. Parallelization is easier due to the compactness of the system.
4. Decentralization is possible, since much of the infrastructure needed in a laboratory is included on the chip.

### 2.1.1 The NASBA chip

In the current project we have worked with a system developed by SINTEF ICT, the Norwegian company NorChip and other European partners. The system detects traces of viral RNA in whole blood samples and consists of two parts; the first part isolates viral RNA from whole blood and the second amplifies and detects targeted RNA strands. Our work has involved developing and fabricating a microfluidic chip in the latter system. A sketch of the chip is shown in figure 2.1. The detailed functionality of the chip is described in Paper D. The RNA is amplified using an isothermal replication technique termed Nucleic-Acid Sequence Based Amplification (NASBA) described in [7] and the chip will be referred to as the NASBA chip.

The NASBA chip is to be used together with an instrument that controls the pressure at the pressure interface, controls the temperature of the reaction chambers and performs

the optical detection of the fluorophore in the last reaction chamber. The working principle goes:

1. The sample is injected into the inlet. Capillary forces draw the fluid into each of the eight parallel channels up to the first capillary valve. The liquid is cut off at the pinching point, so that an exact volume of fluid is measured. Excess fluid is drained into the waste chamber by a filter paper working as a capillary pump.
2. A pressure pulse is actuated through the pressure interface, breaking the first capillary valve. The fluid in each chamber is mixed with stored chemicals and moved to the first reaction chamber.
3. After the first reaction, a new pressure pulse breaks the second capillary valve and moves the fluid to the second reaction chamber where it is mixed with new chemicals.
4. After the second reaction, a fluorophore is excited by an external light source and the resulting fluorescence signal is measured with an external optical system.

When designing a laboratory or a chemical plant today, a common procedure is to divide the functionality of the plant or lab into smaller tasks. These tasks can be carried out by simpler units, for example distillation columns, reaction vessels or mixers. Such unit operations are available in a great variety on the lab scale and also on the chemical plant scale. On the microscale, however, the methods used to perform these tasks are not yet well established. At the same time as complete analysis systems such as the NASBA chip are developed, much work is done on optimizing the functionality of the individual unit operations.

### 2.1.2 A novel micromixer

The micromixer presented in Paper B is a typical microfluidic module performing a single unit operation. On the microscale, viscous forces will dominate over inertia. This can be illustrated by considering the dimensionless Reynold number used to characterize the fluid flow. It is defined by the ratio of inertial forces to viscous forces as

$$Re = \frac{\rho u d}{\eta}, \quad (2.1)$$

where  $\rho$  is the fluid density,  $u$  a characteristic velocity,  $d$  a characteristic length and  $\eta$  the viscosity. On the microscale, both the velocity and the length scale will typically be much smaller than on the macroscale and the flow will be characterized by a low Reynolds number. Many situations occur where  $Re < 1$  and momentum effects typically can be disregarded.

Low Reynolds number flows can also be found on the macroscale when dealing with highly viscous fluids, for example in polymer processing. Because of this, polymer flow will often have similarities to microscale flow. For example, will it in both cases be almost impossible to achieve turbulent flow conditions and in both cases will mixing be a challenge.

In Paper B, an example of a split-and-recombine-mixer is presented. The mixer exponentially increases the interfacial area between two or even more fluids, by splitting

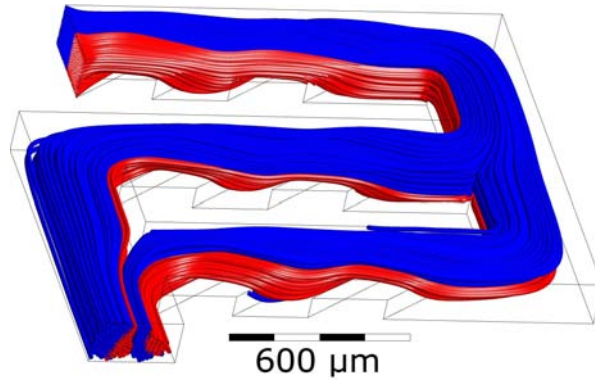


Figure 2.2: One module of a new micromixer presented in Paper B. The image shows simulated stream lines and illustrates the mixing principle. The process is repeated until the desired degree of mixing is achieved.

and recombining fluid streams. The simulated streamlines in one unit of the micromixer is shown in figure 2.2. The working principle goes:

1. The pattern on the channel bed is used to rotate the fluid cross section  $90^\circ$
2. The fluid is split into two substreams
3. The substreams are rotated another  $90^\circ$  before recombination

Several split-and-recombine-mixers have been proposed earlier, see for example the review article on micromixers by Nguyen and Wu [8]. The mixers presented there, however, rely on three dimensional networks of channels for functionality. Fabrication of a chip with three-dimensional networks of channels requires at least two structured parts that have to be precisely aligned during assembly. The main advantage of the present mixer is the open layout which allows easy replication by for example injection molding.

## 2.2 Microoptics

Two of the papers in this thesis relate to a diffractive optical element (DOE) developed by SINTEF ICT in cooperation with the Norwegian recycling company Tomra Systems ASA.

Diffraction describes in general the phenomena occurring when a wave encounters an obstacle. Diffractive optics utilize the diffraction pattern created when light interferes with a structured surface. This diffraction pattern is due to interference of light waves that have traveled different optical paths on the way to the observer.

This is different from conventional refractive optics, used in classical lenses and prisms, which employ the change in direction of light when crossing an interface between two materials of different optical densities. Even though light at different wavelengths behave slightly different in refractive optics, diffractive optics will in general be much more sensitive to the wavelength.

The diffraction pattern of the Tomra DOE implements three different optical functions: 1) It spreads light depending on the wavelength, just as a conventional optical grating, 2) it splits light in five different beams and 3) it focuses light. The DOE can

sequentially focus 5 different predetermined wavelengths onto a detector, by physically rotating the DOE. This is described in detail by Løvhaugen et al. [9].

By measuring how much radiation a sample absorbs at these five wavelengths, a coarse spectrometric measurement can be performed. In the Tomra DOE, these five wavelengths are all in the near IR part of the electromagnetic spectrum. The spectrometer is used in automated recycling centers to automatically separate different polymers handed in by consumers. The different polymers can then be recycled individually, thus enhancing the value of plastic waste.

The optical functionality of the DOE is obtained by patterning the surface with an optical grating on the micrometer scale. In Paper A, it is experimentally investigated how material choice and injection molding processing conditions influence the replication of the optical grating. It was found that good replication could be achieved using different amorphous polymers. However, the replication was very sensitive to small changes in the mold temperature, especially as the mold temperature was close to the glass transition of the polymer. Higher mold temperatures improve replication, but will also increase cooling and cycle time and thus also the cost of the molded product. It was also seen that a high injection velocity had a positive effect on the replication.

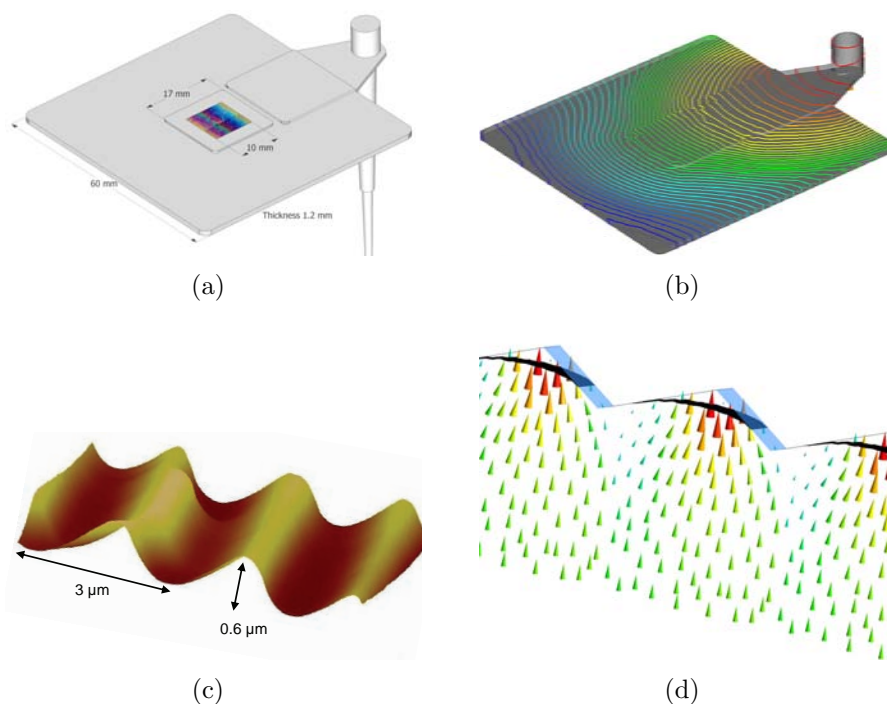


Figure 2.3: Geometry of Tomra DOE studied in Paper A and C. (a) Macroscale geometry with the location of the optical grating indicated by color (b) Filling simulation of the macro geometry showing the flow front at different times. (c) AFM measurement of the optical grating on a molded part. (d) Filling simulation on the microscale showing velocity vectors of the polymer flow field.

In Paper C, the injection molding filling process is simulated and a new method is proposed to couple filling simulations on the micro and macroscale. The simulations also include how the mold wall is heated as it comes in contact with the hot polymer melt. This heating effect is usually neglected in injection molding simulations since both the thermal conductivity and thermal mass of the mold material is so large compared to the

polymer. The temperature increase is indeed quite low, typically below 5 °C, but since it had been observed in Paper A that a change in mold temperature of this magnitude could lead to substantial change in replication, it was concluded that the mold heating did have a significant effect on the replication. The main feature of the DOE geometry and illustrations of the filling simulations performed in Paper C are shown illustrated in figure 2.3.

In a second DOE study, parts were molded and characterized for the Norwegian company OptoSense AS. They have commercialized a CO<sub>2</sub> gas sensor, working by the same principle as the Tomra DOE. One specific wavelength at a time is reflected and focused on a detector. Which wavelength is determined by the angle of incident light. To change the angle, however, a different principle is used. Instead of having a separate unit to perform the swinging motion, the part is molded with a hinge as can be seen in figure 2.4. In the sensor, one side of the plastic part is fixed. On the flexible side with the optical structure, a magnet is attached. An oscillating magnetic field, similar to the working principle of a loudspeaker, is then applied to make the OptoSense DOE oscillate. During each oscillation, all target wavelengths are sequentially focused on a detector.

The hinge and the diffractive optics are molded in one shot. This poses some challenges in the molding process, as the requirements for the two parts of the systems are different. The DOE area should remain flat during part life and the hinge itself should withstand fatigue during billions of scanning cycles (20 years at 2 Hz). At the same time, the replication of the features needs to be sufficient for the optical functionality. To optimize the molding conditions and material choice for part performance, detailed knowledge about how processing settings influence the replication of the optical grating as obtained in Paper A, C and F is essential.

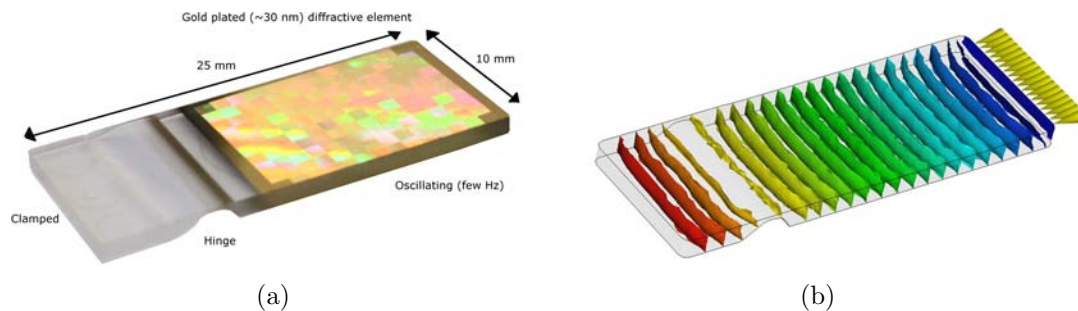


Figure 2.4: The OptoSense DOE used as a CO<sub>2</sub> gas sensor. (a) Photo of a molded part made in polycarbonate. A thin layer of gold has been sputtered on top of the diffractive element. (b) Filling simulation showing the flow front at different times.

## 3 INJECTION MOLDING

In this chapter an overview of injection molding will be given. The chapter is split in three sections describing first the physical injection molding process. Special emphasis will be on steps in the process that are found to be critical for microfeature replication quality. A sketch of an injection molding machine can be found in figure 3.1 and a photo of the machine used in this work (Battenfeld EM 50/120) can be seen in figure 3.2. The second section gives an overview of the different polymer materials used in this thesis. In the last section we show some of the possible methods that can be used to fabricate microfeatured molds and mold inserts.

### 3.1 The injection molding process

#### 3.1.1 Drying the material

Some polymers are hygroscopic to such an extent that absorbed moisture from the air can be a problem in the injection molding process. The problems can be either due to polymer degradation as it is heated in contact with water or due to water trapped in the polymer which expands as it is vaporized. In general, the polymer manufacturer recommends drying such materials for a given time at a given temperature before processing. If high surface quality is an issue, the recommendation is to dry the material for a longer time. The material was dried in a 5 liter container mounted directly on the hopper using a dedicated drying system (WINsystem MicroD from Helios Gerätebau für Kunststofftechnik GmbH). Usually, it was found sufficient to use hot air for drying, but when fabricating polycarbonate products, less polymer degradation was observed when using nitrogen instead.

#### 3.1.2 Melting and metering the material

The screw on the injection molding machine has three main tasks; 1.) melt the polymer pellets and distribute the material to a uniform melt, 2.) meter an exact material volume and 3.) inject the melt into the mold.

Most of the work of heating the polymer to a melted state is done by viscous dissipation within the screw itself. The heating bands surrounding the screw control the polymer temperature. A single general purpose screw with diameter 25 mm was used for all the studies in this work.

It is essential for injection molding that the temperature and material properties are uniform throughout the injected melt. Our products were typically small with micro-

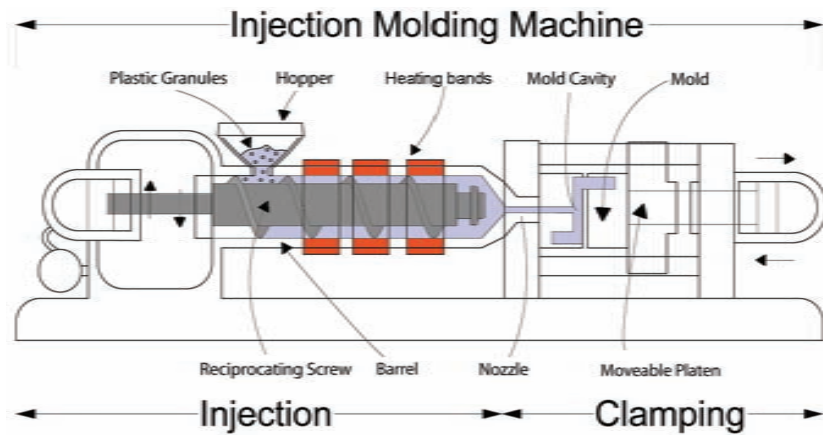


Figure 3.1: Sketch of an injection molding machine. (Created by Brendan Rockey, licensed under the Creative Commons Attribution 3.0 License)

features located only in a limited area and no problems indicating a non-uniform melt were encountered during this project. However, if molding large products containing large areas filled with microfeatures this could be expected to be a challenge.

It is possible to improve replication of microfeatures by increasing the melt temperature [10, 11], but the possible improvement within the processing window is relatively limited. A too high melt temperature can lead to polymer degradation. In this work, we typically held the melt temperature within the manufacturers recommended range, starting at the higher end of the interval and decreasing the melt temperature if any sign of polymer degradation was seen in the product.

### 3.1.3 Melt injection

The polymer melt is injected into the mold by moving the screw forward inside the barrel. The injection profile is controlled until a designated switchover criterion has been met (either a given volume has been filled or the pressure has risen to a given level).

Increasing the injection velocity will lead to an increased pressure build-up during filling and a shorter time before the holding pressure is applied. This will lead to an improvement in replication as has been seen experimentally [12, 13] and verified in the experimental study in Paper A. In general, there is a maximum injection velocity that the machine can achieve. It will be limited by the speed at which the screw can be moved forward. The clamping force of the machine (the force that holds the mold closed during molding) is also limited. If the injection velocity is too high, the mold will open during injection and so called flash will be observed. Studies from the literature have reported results with dedicated high speed injection molding machines. It is showed that the replication of microfeatures can still be improved by increasing the injection velocity far above what can commonly be achieved using conventional injection molding machines [14].

At the flow front, during injection, there will be a fountain flow region. In this region, material is transported outwards towards the mold wall and will at the same time be oriented and stretched. This will cause the polymer to be in a state of tension as it hits the polymer wall. Depending on the microfeature geometry, this tension might lead to

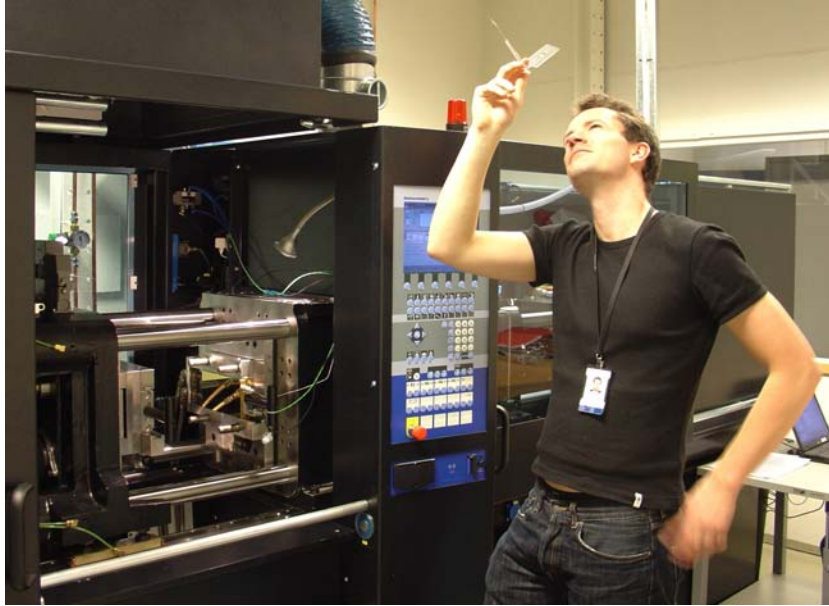


Figure 3.2: Visual inspection of a newly molded component with microfeatures. The Battenfeld EM 50/120 in the background.

improved filling of the microfeatures [15].

### 3.1.4 Holding pressure

After switchover, a controlled pressure is applied. This pressure is set to compensate for the polymer shrinkage as it cools down. The results in Paper C indicate that by the time the holding pressure was applied, the polymer surface temperature was close to the glass transition temperature. When using the glass transition as a no-flow temperature, which is common in injection molding simulations, an increase in holding pressure will therefore not influence the replication.

Still it has been shown that increasing the holding pressure applied after filling will have a positive effect on replication of microfeatures [12, 10]. This can partly be explained by the polymer still being warm enough to be deformed elastically by the holding pressure. Given that the pressure is applied for a sufficient time, there will also be some relaxation of the elastic deformation.

Other studies again have reported a negative effect of higher holding pressure [16, 17]. In Paper F, this effect is studied in detail. We find that an increased holding pressure can have a positive effect, similar in nature to what is found when increasing the injection velocity. However, we also find that there is a maximum in replication as a function of holding pressure. Above this maximum, the replication decreases with increasing holding pressure. The experimental results in Paper F indicate that the parts molded with the highest holding pressure did indeed fill the mold completely during the holding pressure phase but after the holding pressure was released, the polymer recoiled.

### 3.1.5 Part cooling

The holding phase ends when the cavity pressure decreases to zero. This happens either as the gate (the thinnest section connecting the polymer part to the runner system) freezes or the holding pressure is removed. During the cooling phase, the polymer must be cooled down to a temperature that allows demolding of the part. Naturally this goes faster if the mold is colder. This phase is probably the least eventful phase of the injection molding cycle, but also the phase that takes the most time. Often more than 50 % of the cycle time is spent cooling the product. There is some room to optimize the cooling process by ensuring good thermal contact between the mold and the polymer. A uniform part thickness will also be beneficial to avoid hot spots, but the most efficient step is to reduce the mold temperature during cooling.

### 3.1.6 Controlling the mold temperature

In general, the replication of microfeatures is sensitive to a change in mold temperature. An increased mold temperature has been shown to improve replication in several experimental studies [18, 19, 20] and in the experimental study in Paper A, we find that this sensitivity to mold temperature is especially large when the mold temperature is close to the glass transition temperature of the polymer. The glass transition acts as an effective no-flow temperature, below which the viscosity of the polymer is so high that it effectively ceases to flow. If the mold temperature is kept above the glass transition, the mold will fill completely as long as a pressure is applied for a long enough time. However, the polymer needs to be solid during demolding. By increasing the mold temperature the cooling time and also cycle time will be increased. This will in turn increase the cost of the molded product. Ideally, the temperature of the mold should be high during filling and then low during cooling. Unfortunately for this purpose, injection molds are usually heavy structures with a high thermal mass, designed to withstand the clamping forces needed to close the mold during filling. Heating and cooling the entire mold during molding is therefore not cost effective. Several suggestions on how to modulate the temperature during molding with minimal impact on cycle time are discussed in a review of so-called variotherm processes by Yao and coauthors [21]. Some of the most promising methods involve heating only the surface layer of the mold directly before injecting the melt. This can be done for example by induction heating.

In all the published studies in this thesis we have used tempered water to control the mold temperature. The water temperature was controlled externally (using HB-Therm Series 4 from HB-Therm GmbH) in a closed loop system. The water temperature as it leaves the controller is set at a given value. It was observed that the return water temperature deviated less than 1 °C from this. The measured mold temperature could deviate more and would also vary during the injection molding cycle. As a part of the study in Paper A and Paper F it was confirmed that the mold surface temperature just before the polymer melt was injected deviated less than 2 °C from the set water temperature.

### 3.1.7 Demolding

When the part has been cooled down to below its solidification temperature it has to be removed from the mold. The most common way to eject the part is to use ejector

pins that push the part out of the mold. This can be a critical step when fabricating parts with microfeatures. To help facilitate this step, most conventional molds are made with a draft angle of  $1 - 2^\circ$ . Such angles can be difficult to fabricate for microfeatures, especially for high aspect ratio structures.

For the NASBA chip, it was possible to mill the mold with a draft angle. For the blazed gratings on the Tomra DOE, an angle was inherent in the structure design. Hence, demolding was in general not a big issue in the current study. The interested reader could refer to the work of Michaeli and Gartner for a discussion on some of the problems regarding demolding and some new concepts on how to demold parts with microstructures [22].

## 3.2 Polymer materials

In this thesis, all the polymers used have been optical grade, low molecular weight, amorphous thermoplastics. Amorphous means that the polymers do not crystallize when cooled from the melted state. Thermoplastic means that the polymer, in contrast to a thermoset, do not go through a chemical transformation when solidifying. In this project amorphous polymers were chosen over semi crystalline ones, partly because polymers from the latter group have a larger change in volume when solidifying. This gives less control over dimensional stability. Thermosets can also be used for making microfeatured parts, but the cycle time will usually be longer since the chemical curing typically is slower than the rapid cooling of thermoplastics in injection molding.

One general remark will be made before describing the polymers used in this work individually. At least for diffractive optics with low aspect ratio microfeatures, all the materials tested have been shown to successfully replicate micrometer and sub-micrometer sized features. This requires individual tuning of the process parameters and often a somewhat higher mold temperature than what is recommended from the manufacturer. Nevertheless, the fact that all these polymers are found suitable for replication of microfeatures means that the part designers can choose from a relatively wide selection of polymers when designing microfeatured components. The material can then often be chosen to meet other design criteria, which in turn gives a broader application window for microfeatured parts made in polymers.

### 3.2.1 Polycarbonate

Polycarbonate (PC) is an often used group of polymers because of its mechanical toughness and optical clarity. The term carbonate does not refer to the monomer of PC, but rather to the  $-O-(CO)-O-$  group linking the monomers together. This means that there is a large group of possible structures that could justifiably be called PC. However, the vast majority of PCs, also the ones used in this study, are polymers of bisphenol A [23] with the molecular formula shown in figure 3.3.

In this work two optical grade polycarbonates have been used. One DVD grade (Lexan OQ1026 from SABIC Innovative Plastics) and one intended for use in car headlight systems (Lexan LS2 from SABIC Innovative Plastics). OQ1026 is a low molecular weight PC with very good flow properties, optimized for the mass production of DVDs. LS2 has a higher molecular weight giving better impact resistance, needed for example

when pieces of debris hits the car lightning system at relatively high speeds. The higher molecular weight also gives LS2 a higher viscosity which makes it slightly more difficult to process.

Even though only the low molecular weight PC is especially made for replicating microfeatures, it was observed that also the LS2 could be used for this application. It was, for example, possible to achieve good replication of the Tomra DOE using the same values for injection velocity, mold and melt temperature as for the OQ1026 . We presented these results at the PPS conference in Salerno [24]. However, since the viscosity of the LS2 is so much higher than the OQ1026, the same injection velocity gives a much higher cavity pressure, which might be a limiting factor in the fabrication process. When investigating the effect of holding pressure in Paper F, we also used these two PCs. In the OptoSense study, small scale commercial production was done making diffractive optical elements in OQ1026.

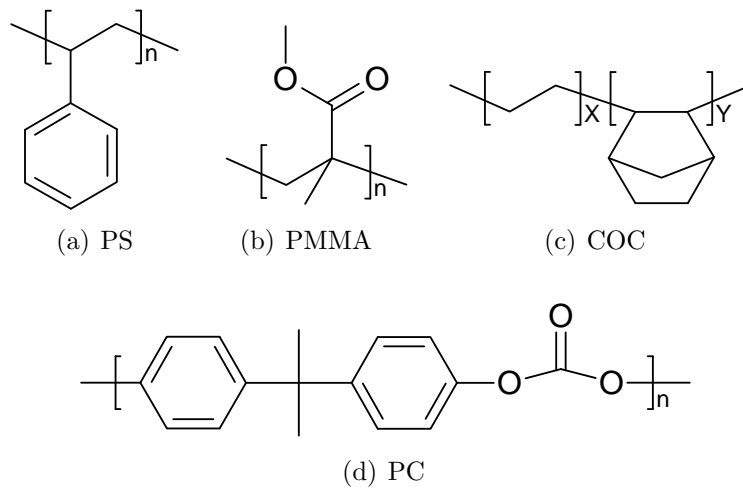


Figure 3.3: The chemical structure of four transparent amorphous thermoplastics used in this thesis,  $n$  is an integer specific for each molecule in the material.  $X$  and  $Y$  are also integers but they will also vary within a single polymer chain. The COC is a random copolymer with about 50 mol% norbornene

### 3.2.2 Poly(methyl methacrylate)

Poly(methyl methacrylate) (PMMA) is the polymer of methyl methacrylate. The chemical formula is given in figure 3.3. As is the case with PC, PMMA is also used in many applications as a substitute for glass because of good optical properties and low density.

When replicating the Tomra DOE in Paper A we used an optical grade PMMA with low molecular weight (Plexiglas POQ62 from Röhm GmbH & Co.).

A special property of PMMA, is that its IR absorption spectrum makes it applicable for laser ablation. In the study with the micromixer in Paper B, a  $\text{CO}_2$  laser with wavelength 10.6  $\mu\text{m}$  was used to produce prototype microchannels directly in PMMA. The laser could then also be used to seal off the channels.

### 3.2.3 Cyclic olefin copolymer

The cyclic olefin copolymer (COC) used in this study is a copolymer of norbornene and ethylene as shown in figure 3.3. The name copolymer states that the polymer is built up by more than one monomer. One of the monomers, in this case norbornene, is cyclic. COC materials have become popular in use for lab-on-a-chip applications because of low water permeability, good bio-compatibility, optical properties and low autofluorescence. One attractive property of COC is that by using grades with increasing norbornene content, a higher glass transition temperature can be obtained. This way, several polymers can be made that are chemically similar but with different temperature response. This can for example be used when bonding a lid on top of a lab-on-a-chip device. A low  $T_g$  grade lid can be thermally bonded on top of a high  $T_g$  grade without damaging the features of the latter. This can be done without introducing any different surface chemistry than what is already present.

In the NASBA chip study described in Paper D, parts were made in a low molecular weight grade COC with around 50 mol% norbornene content. (5013S-04 from TOPAS Advanced Polymers). The same grade was also used to fabricate the Tomra DOEs described in Paper A and for the simulations study in Paper C.

### 3.2.4 Universality of chain dynamics in polymers

It has been claimed recently that there is an almost universal temperature dependence of chain relaxation times for different polymers above the glass transition [25, 26, 27]. After a comment from Ngai et al [28], the universality has later been toned down by the original authors [29]. The universality claimed, states that the chain relaxation time  $\tau_n$  follows the same trend for all polymers,

$$\log \tau_n = f\left(\frac{T_g}{T}\right) - A, \quad (3.1)$$

where  $f$  is the same function for all polymers,  $T$  is the absolute temperature,  $T_g$  is the absolute glass transition temperature and  $A$  is a polymer specific constant. Such universalities are of great interest in general polymer processing since the knowledge of the relaxation time at one temperature could be used to determine the relaxation time at all other temperatures.

Similar universalities have been proposed earlier. The perhaps most well known is the universality proposed in 1955 by Williams, Landel and Ferry [30] of the WLF parameters (after the authors' initials). They proposed that all mechanical and dielectrical relaxation times have the same temperature dependence.

$$\log_{10} \left( \frac{\tau(T)}{\tau(T_g)} \right) = - \frac{C_1 (T - T_g)}{C_2 + (T - T_g)} \quad (3.2)$$

After experimental investigation of several polymers, polymer solutions and organic glass forming liquids they suggested that the constants  $C_1 = 17.44$  and  $C_2 = 51.6$  K were universal. The form of the equation originates from the assumption that free volume is a linear function of temperature. Later, after more extensive experimental testing of different polymers, it became clear that the constants were not universal. It was for example stated by Ferry, one of the original authors [31]

It is evident that the actual variation from one polymer to another is too great to permit use of these “universal” values except as a last resort in the absence of other specific data.

The WLF equation is still in much use, but then with the parameters individually fitted for each polymer as we also do in Paper C and E. If the WLF parameters were universal, one implication would be that equation 3.1 is correct. However, the opposite relation does not hold. Equation 3.1 can be valid without universal WLF parameters. When stating the universality it is claimed that the  $T_g/T$  dependence has an energetic interpretation [25].

In paper E, we have tested this universality experimentally for four low viscous amorphous polymers by measuring the zero shear rate viscosity at different temperatures. As discussed in the paper, the zero shear rate viscosity will have approximately the same temperature dependence as the chain relaxation time. The glass transition was determined using dynamic rheometry. Unfortunately, our findings suggest that such a universality does not exist.

### 3.3 Mold making

Injection molding is a replication technique. This means, that to mold a microfeatured part, a microfeatured mold is required. There are naturally numerous ways to fabricate such a mold. The methods used in this work will be introduced in this section.

#### 3.3.1 Milling

Milling is a subtractive fabrication method used to produce parts in metals and other solid materials. Material is removed from a workpiece by bringing it in contact with a tool, rotating at high speed.

As the accuracy of milling machines and the tools used has improved, the field of micromilling has gradually evolved. In the NASBA study, most features of the mold were milled in brass using a diamond tool by the Austrian company Z-Microsystems as seen in figure 3.4. The accuracy of the milling was typically better than 10  $\mu\text{m}$ , but the inner corner radius of the features that can be produced is limited by the tool radius. To avoid tool breakage during milling, it is difficult to go below a tool diameter of 200  $\mu\text{m}$ . On the NASBA chip, there were capillary valves that required a corner radius of less than 50  $\mu\text{m}$ . This could not be achieved using milling and was made using electrical discharge machining (EDM) instead.

It was desired to keep the surface roughness of the chip as small as possible. A diamond tool was chosen for this purpose. This in turn required the mold insert to be machined in a rather soft metal and brass was chosen in this case.

It is also possible to do milling directly in polymer materials, which was done in the work with the micromixer in Paper B. However, since polymer materials usually are much softer than metals and have a lower melting temperature, directly milled surfaces will in general have higher surface roughness than what can be achieved by first milling in metal and then molding a replica.

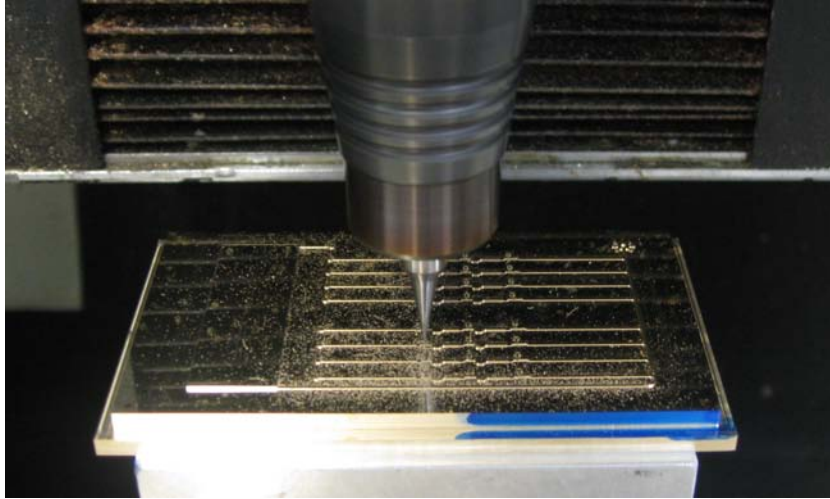


Figure 3.4: Milling of the insert for the NASBA-study performed by the Austrian company Z-Microsystems

### 3.3.2 Electrical discharge machining

Electrical discharge machining (EDM) is a process based on an electrical discharge (spark) between an electrode and a workpiece which erodes material from the workpiece. This is also, as the milling process, a technology that has been gradually adapted to the microscale. The forces acting on the electrode during EDM are much smaller than the forces acting on the end mill during milling. Hence, it is possible to use an electrode with a relatively small radius. For the capillary valves on the NASBA chip, it was necessary to have a sharp corner to temporarily stop a liquid meniscus. The valve is seen in figure 3.5. This valve was made by first milling with a large radius and then using die sinking EDM to sharpen the corners.

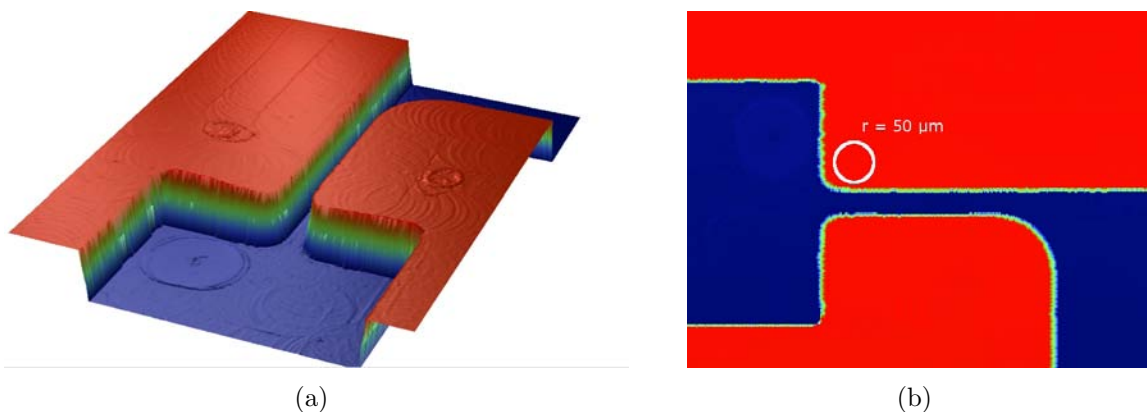


Figure 3.5: Topography of a molded capillary valve on the NASBA chip measured using white light interferometer. Sharp corners were required in order to stop a liquid meniscus moving forward. This could not be achieved using micromilling so these specific features were made using EDM. (a) 3D view of the valve with the milling pattern visible ( $R_a \approx 50 \text{ nm}$ ) (b) top view of the valve with the design criterion that the corner radius should be less than  $50 \mu\text{m}$  indicated.

The main reason why milling and EDM are so much used when producing microfea-

tured molds is that it is possible to work directly in a durable material when making the mold. Also, most mold makers already have the equipment ready for performing these processing steps since they are commonly used in many workshops.

### **3.3.3 Electron beam lithography**

Electron beam lithography (EBM) is used to make very fine details, often smaller than the diffraction limit of light. The working principle is similar to that of the scanning electron microscope. A beam of electrons is focused onto a workpiece (typically a polymer, a so called resist) using electrostatic or magnetic lenses. Then, in the development process, material is removed from either the exposed or unexposed regions depending on the resist. Several electromagnetic lithographic techniques also exist, but they will, as optical microscopes have a limited resolution due to the diffraction limit of the electromagnetic radiation.

The diffractive optical elements in the Tomra and OptoSense cases were made using e-beam lithography of a resist, followed by electroplating in nickel to produce a durable material for molding. The resulting nickel shim is clamped in a mold for replication using injection molding.

## 4 SURFACE CHARACTERIZATION

The goal of the surface characterization in this thesis was typically to provide precise and accurate measurements of a surface topography. The features that should be characterized varied in size down to sub micrometer and often included sharp steps. Both contact and non-contact methods were used for characterization and the methods will be presented in this section. The resolution desired was often in the nanometer range, which set special requirements on the measurements.

### 4.1 White light interferometry

A white light interferometer (WLI) is used to characterize the surface topography of a part. The instrument consists of an optical microscope in connection with a beam-splitter. One beam is sent through the objective lens of the microscope and reflected from the sample. The other beam is reflected by a reference mirror. Before being registered at a CCD camera, the two beams are recombined. If the optical paths traveled by the two beams differ by an integer number of wavelengths, there will be constructive interference. If the path difference is an odd integer of half wavelengths, destructive interference will be observed. If the surface of the sample is in focus, the two beams will recombine to create bright and dark bands called fringes, representing the topography of the sample.

The optical microscope has a very limited depth of field. This typically means that the focus length in the vertical direction is only a few hundred nanometers. The instrument used for measuring the parts in Paper A (WYKO NT-2000 from Veeco Instruments) has two modes of operation. The first determines the vertical location based on the position of the fringe with the best contrast, termed vertical scanning interferometry (VSI). VSI can facilitate a long vertical scan range (up to 7 mm) and a good resolution in the vertical direction, down to 3 nm according to the manufacturer. The other mode of operation, termed phase shifting interferometry (PSI) determines the phase of the fringe pattern and uses this to reconstruct the vertical location. PSI has a better resolution going down to 0.3 nm, but suffers by a much lower vertical scan range of only 160 nm. The reason for the short scan length of PSI is that, given the phase of the fringe pattern, there will always be an ambiguity as to whether a point has the vertical location  $z$  or  $z + \frac{1}{2}n\lambda$ , where  $n$  is an integer and  $\lambda$  is the wavelength of the lightsource. The lateral resolution of a WLI is similar to what can be achieved with an optical microscope, meaning that it is possible to distinguish objects separated by a distance similar to the wavelength of visible light.

A DOE typically have dimensions similar in size to the wavelength of the radiation that it is supposed to be working at. The size of the structures are thus on the limit of

what can be detected with a white light interferometer. This means that a measurement of a single peak on a DOE using WLI will be subject to a large uncertainty. In order to achieve better statistics when reporting the degree of replication, a method using the power spectrum density of the part topography was utilized in Paper A. The part surface can be described by a function  $z = f(x, y)$  describing the vertical height in each point. The power spectral density  $\Phi(\omega)$  of this function is defined as:

$$\Phi(\omega) = \frac{1}{L_y} \int_0^{L_y} \left| \frac{1}{\sqrt{2\pi}} \int_0^{L_x} f(x, y) e^{-i\omega x} dx \right|^2 dy, \quad (4.1)$$

where  $L_x$  and  $L_y$  are the dimensions of the captured image. This is similar in form to the Fourier transform of the signal averaged in  $y$  direction. An illustration of the PSD can be seen in figure 4.1. The diffractive optical element has period of  $3 \mu\text{m}$  and a peak to valley distance of  $600 \text{ nm}$ . The PSD takes this periodic pattern and transforms it into the frequency domain. The maximum is found at the inverse of the wavelength  $(3 \mu\text{m})^{-1}$ . The PSD will be proportional to the height of the topography squared as can be seen by multiplying  $f(x, y)$  in equation 4.1 with a constant factor. To define the degree of replication of the optical gratings molded in Paper A we compare the PSD of the molded parts with the PSD of the shim. The degree of replication is defined as the ratio of the square root of the area colored green in figure 4.1b measured on the molded part to the same quantity measured on the shim. This procedure made it relatively easy to compare the replication of microfeatures using different materials at a range of processing settings.

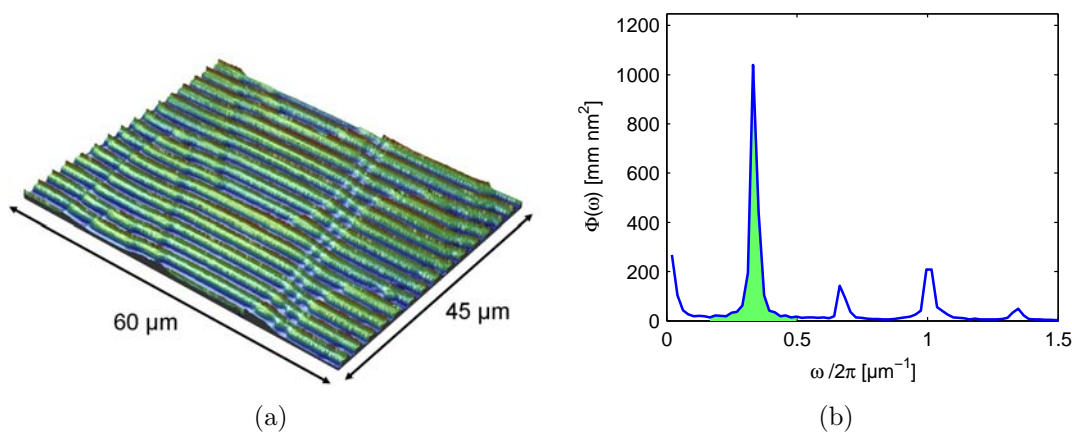


Figure 4.1: (a) The topography of a Tomra DOE molded in polycarbonate as measured with WLI. (b) The power spectrum density of the same part. The area colored green is used for defining the degree of replication.

For the work in Paper F a newer WLI instrument was used (WYKO NT-9800 from Veeco Instruments). The most notable difference is a new mode of operation termed high definition vertical scanning interferometry (HDVSI) which combines the two methods PSI and VSI in one measurement. The coarse vertical location of a point is estimated using VSI and the phase information from PSI is used to locate the point more accurately. A comparison of the VSI and the HDVSI signal for the same optical grating is shown in figure 4.2. First of all, HDVSI has a much lower noise level than VSI. It was also observed that some optical artifacts that were introduced when measuring sharp

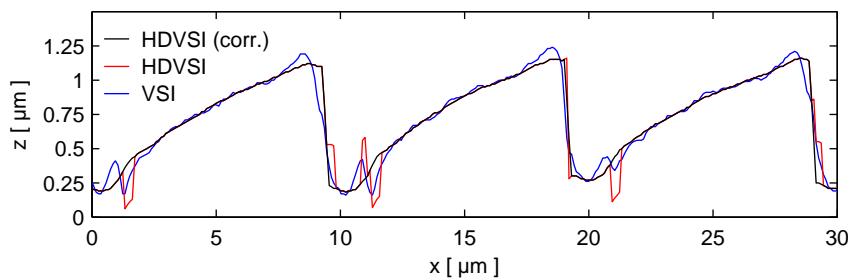


Figure 4.2: Comparing the same optical grating measured using different modes of the white light interferometer. Optical artifacts in the VSI signal (blue line) propagate to the HDVSI signal (red line). The artificial jumps in the signal of half the wavelength of the light source (303.4 nm) were manually removed when analyzing parts for paper F. The grating profiles presented in the paper correspond to the black line.

steps using VSI, could be avoided using HDVSI.

It is known from the literature [32] that optical artifacts might occur when measuring step heights using VSI. This is also seen in the VSI signal in figure 4.2, both close to the peak and in the valley. Since the VSI signal is used to reconstruct the surface in the HDVSI mode this will also lead to artifacts in the HDVSI signal as can be seen in the red curve of figure 4.2. These artifacts were manually removed from the HDVSI signal to construct the final measurement shown in black. In Paper F this procedure was used to provide measurements of molded gratings with a very low noise level and seemingly without the artifact prone to a VSI measurement.

## 4.2 Scanning electron microscopy

The wavelengths of the electromagnetic spectrum visible to the human eye are about 380 – 750 nm. This poses a limit in the resolution of conventional microscopes. A scanning electron microscope (SEM) is in some aspects similar to an optical microscope but uses electrons instead of photons to create an image of a subject. According to quantum mechanics all matter has a wave-like behavior. The wavelength  $\lambda$  of a given particle relates to its momentum  $p$  by the de Broglie relation

$$\lambda = \frac{h}{p}, \quad (4.2)$$

where  $h = 6.63 \cdot 10^{-34}$  Js is the Planck constant. The de Broglie wavelength for an electron accelerated by a typical voltage in a SEM of 20 kV is 0.009 nm, well below the radius of the smallest atom, hydrogen, and the wavelength of the electrons is in general not a limiting factor for SEM resolution.

The SEM instrument used in this work (Quanta 600 FEG-SEM from FEI Company) first accelerates a beam of electrons in an field emission gun using an acceleration voltage of typically 1 – 40 kV. The beam is focused on the substrate using condenser lenses and the surface is scanned line by line. The interaction between the electron beam and the sample results in three main types of emissions; 1.) reflection of high-energy electrons by elastic scattering, 2.) emission of secondary electrons by inelastic scattering and 3.) emission of electromagnetic radiation. These three types of radiation can be detected

by different detectors. In this work only the secondary electrons have been used for imaging. These electrons are emitted from the atoms in the top few nm of the sample surface.

All parts investigated were sputtered with a 50 nm thick gold layer before investigation to make the surface conductive. In figure 4.3 two SEM images of the Tomra DOE are shown.

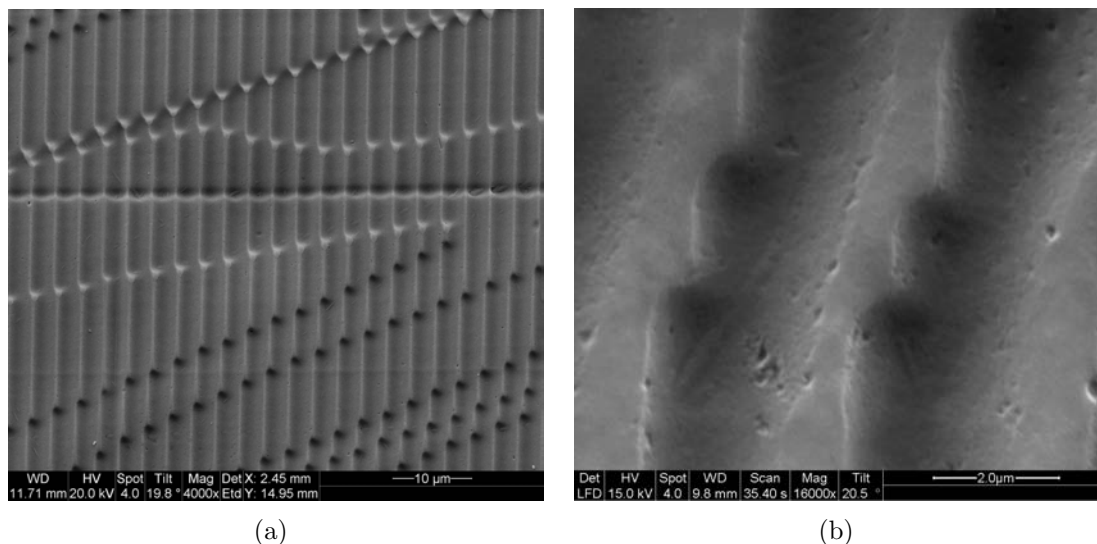


Figure 4.3: (a) SEM image of the surface of the Tomra DOE molded in COC. (b) Same part with higher magnification. It can be seen that the surface has a smoother character where it is solidified without contact with the mold surface.

### 4.3 Atomic force microscopy

Atomic force microscopy (AFM) belongs to the family of scanning probe microscopes in which solid surfaces are scanned by extremely sharp mechanical probes. In what is called tapping mode, the cantilever with the probe tip is driven to oscillate near or at its resonance frequency. As the tip comes in close proximity to the sample surface there will be forces acting on the probe tip. These forces will disturb the oscillations of the cantilever, giving information about the sample surface. One big advantage with the AFM for the optical structures investigated in this work is that there was no need for sample preparation. The sample could be loaded directly into the instrument for characterization. Another advantage is the excellent resolution possible. The AFM was first described by Binnig, Quate and Gerber in 1986 [33] and reported then to give a lateral resolution of 30 Å and a vertical resolution of 1 Å, smaller than the diameter of a carbon atom. Recently, individual atoms of molecules adsorbed on a surface were resolved using AFM [34].

In the studies of optical gratings, the smallest structures of interest had critical dimensions in the range 200 nm – 5 μm, i.e. well above the theoretical resolution of the AFM. The difficulty came from the fact that some of the structures were relatively deep with an aspect ratio up to 2. In order to capture the topography of these structures accurately, it was necessary to use very sharp and small angle probes. The probes

(AR5T-NCHR from Nanosensors) were used in this case having a tip radius of less than 15 nm. The AFM used was a Dimension 3100 with a NanoScope IIIa from Digital Instruments. The main reason why AFM was not exclusively used for measuring sample topography is that it is a much slower method than WLI. It also involves bringing a probe in contact with the sample. This will in some cases damage the sample or the probe may pick up dust on the sample surface interfering with the measurement.



# 5 FILLING SIMULATIONS

The goal of the injection molding simulations in this work is partly to understand how and under which conditions microfeatures form during injection molding and thereafter; to be able to predict how well replicated a microfeature will be, given the polymer, processing equipment and processing settings.

This is not a trivial task and in my opinion, the main challenges compared to conventional injection molding simulation are:

- The relevant polymer rheology is more complex. The viscosity changes by a factor of  $10^6$  as the microfeatures are formed. As is shown in Paper F, elastic effects, which can normally be neglected in injection molding simulations, have a significant influence on the replication of the microfeatures.
- There is a high cooling rate (up to 10.000 K/s) close to the mold/polymer interface. Exactly how high, will mainly be determined by the wall heat transfer condition. This condition is to a large extent unknown but has major implication on the replication of microfeatures.
- Flow phenomena on the microscale are coupled to flow phenomena on the macroscale. The size ratio of the features (sub  $\mu\text{m}$ ) to the whole part (several cm) is similar to that of an ant (few mm) to the Burj Dubai (818 m). These two size ranges can not effectively be modeled in the same simulation and thus have to be solved individually.

In Paper C, we have simulated the injection molding process of a microfeatured part. It was decided to neglect the elastic response of the polymer and treat it as a generalized Newtonian fluid, as is common in conventional injection molding simulations. The focus in the study was the coupling between the micro and macroscale and to get a realistic description of the polymer viscosity through the whole processing cycle. The effect of mold heating was also included in the simulations. Even though a viscous description of the polymer melt has some shortcomings, it was possible to describe well how changes in the processing settings change the replication of the microfeatures.

## 5.1 Model description

### 5.1.1 Governing equations

The governing equations in the computational fluid dynamics simulations performed in this work represent the conservation of mass, linear momentum and energy. They are

written on a differential form as:

$$\frac{\partial}{\partial t}(\rho) + \nabla \cdot (\rho \mathbf{U}) = 0 \quad (5.1)$$

$$\frac{\partial}{\partial t}(\rho \mathbf{U}) + \nabla \cdot (\rho \mathbf{U} \otimes \mathbf{U}) = -\nabla p + \nabla \cdot \mathbb{T} + \mathbf{f} \quad (5.2)$$

$$\frac{\partial}{\partial t}(\rho e) + \nabla \cdot (\rho \mathbf{U} e) = \nabla \cdot \mathbf{q} + \mathbb{T} : \nabla \mathbf{U}, \quad (5.3)$$

where  $t$  is the time,  $\rho$  is the density,  $\nabla = \left( \frac{\partial}{\partial x}, \frac{\partial}{\partial y}, \frac{\partial}{\partial z} \right)$ ,  $\mathbf{U}$  is the velocity vector,  $p$  is the pressure (one third of the trace of the stress tensor),  $\mathbb{T}$  is the deviatoric stress tensor,  $\mathbf{f}$  represents non-contact forces per unit volume,  $e$  is the internal energy per unit volume and  $\mathbf{q}$  is the heat flow vector. The operator  $\cdot$  is the inner product between two vectors,  $\otimes$  is the outer product between two vectors and  $:$  is the inner product of two second rank tensors. In addition, in order to conserve angular momentum it is required that  $\mathbb{T}$  is symmetric.

Equation 5.1 - 5.3 are derived in most textbooks in continuum mechanics and no derivation will be given here. However, the assumptions behind the equations and their physical significance will be discussed briefly.

First, it is assumed that matter is continuous. In fact, a polymer melt consists of individual molecules, but the assumption of a continuum is good as long as the length scale of the system is much larger than the molecular length scale. Since in the present case, features with characteristic length down to a few hundred nanometers are considered, a test of the continuum approximation is necessary. Consider a monodisperse polymer with molecular weight 10.000 g/mol and density 1.000 kg/m<sup>3</sup>. In every cubic micrometer there will then be 60.000 polymer chains. This is probably a large enough number for the continuum approximation to be valid. However, if the length scale is reduced further, the assumption of a continuum will eventually break down. Reducing the system length scale to 10 nm, it approaches the gyration radius of the individual polymer molecules. Such length scales are found for example in nanoimprint lithography (NIL) and the polymer rheology when confined to volumes with dimensions on this scale has been shown to deviate considerably from the macroscopic behavior [35, 36]. At the length scales considered in this work, however, the material properties of the polymer will be treated as scale independent.

Equation 5.1 is obtained by assuming that when there is a zero net flux of mass into any control volume, the mass within remains constant. This holds for classical mechanics, but fails if relativistic effects are important. In the present study, all velocities are far below that of the speed of light and the energy exchange is insignificant compared to the classical mass of the matter involved.

Equation 5.2 is obtained by assuming that Newton's second law is valid for any control volume. That is, the time derivative of the momentum (left side of equation 5.2) equals the sum of contact forces ( $-\nabla p + \nabla \cdot \mathbb{T}$ ) and non-contact forces ( $\mathbf{f}$ ). The non-contact forces usually only include gravity, but may also include for example electromagnetic forces. In the cases discussed in this thesis, gravitation was found negligible compared to the viscosity and only contact forces were included.

Equation 5.3 is the first law of thermodynamics for an arbitrary control volume. The change in energy (left side of equation 5.3) equals the sum of heat added to the control

volume ( $\nabla \cdot \mathbf{q}$ ) and work performed on the control volume ( $\mathbb{T} : \nabla \mathbf{U}$ ).

### 5.1.2 Constitutive equations

Equations 5.1 - 5.3, merely describes the conservation of mass, linear momentum and energy. The equations are valid for both elastic solids and viscous liquids. The difference between the two types of materials is how deformations of the material relate to stresses in the material. This relationship is called the constitutive relation. For an isotropic, viscous fluid, the deviatoric stress tensor is given by

$$\mathbb{T} = 2\eta \left( \mathbb{E} - \frac{1}{3}(\nabla \cdot \mathbf{U})\mathbb{I} \right), \quad (5.4)$$

where  $\mathbb{E} = \frac{1}{2}(\nabla \mathbf{U}) + \frac{1}{2}(\nabla \mathbf{U})^T$  is the rate of strain tensor and  $\mathbb{I}$  is the second rank identity tensor. If the viscosity  $\eta$  is constant, the fluid is called Newtonian. This model describes what we can call an ideal fluid. The model is a good approximations for many fluids, among them liquid water at constant temperature. If, in addition, it is assumed that the density is constant and no non-contact forces are present, equation 5.1 and 5.2 are simplified to:

$$\nabla \cdot \mathbf{U} = 0 \quad (5.5)$$

$$\frac{\partial}{\partial t} (\rho \mathbf{U}) + \nabla \cdot (\rho \mathbf{U} \otimes \mathbf{U}) = -\nabla p + \eta \nabla^2 \mathbf{U} \quad (5.6)$$

In Paper B regarding the novel micromixer, this is the form used when simulating the isothermal flow of water.

When simulating the non-isothermal flow of a polymer melt, the assumption of a constant viscosity is no longer valid. The viscosity depends strongly on temperature and also on the rate of deformation. As a part of the simulation study in Paper C, the viscosity of the COC was measured. This was done using a rheometer at constant shear for measuring low shear rate deformations and using dynamic rheometry for the higher frequencies. The results are summarized in figure 5.1. Note that the entire temperature and shear rate range from the figure is relevant for the formation of polymer microfeatures in injection molding. During injection the shear rates may also exceed the measurement range from the figure.

When simulating injection molding it is common to use a viscosity which is dependent on the temperature  $T$  and the second invariant of the rate of strain tensor  $\dot{\gamma} = \sqrt{\frac{1}{2}\mathbb{E} : \mathbb{E}}$ . The specific model which was used in Paper A and C is the Cross-WLF model.

$$\eta(T, \dot{\gamma}) = \frac{\eta_0(T)}{1 + \left( \frac{\dot{\gamma} \eta_0(T)}{\tau^*} \right)^{1-n}} \quad (5.7)$$

$$\log_{10} \frac{\eta_0(T)}{\eta_0(T_{\text{ref}})} = \frac{-C_1(T - T_{\text{ref}})}{C_2 + T - T_{\text{ref}}} \quad (5.8)$$

The model parameters  $C_1$ ,  $C_2$ ,  $T_{\text{ref}}$ ,  $n$ , and  $\tau^*$  were fitted to match the measured viscosity.

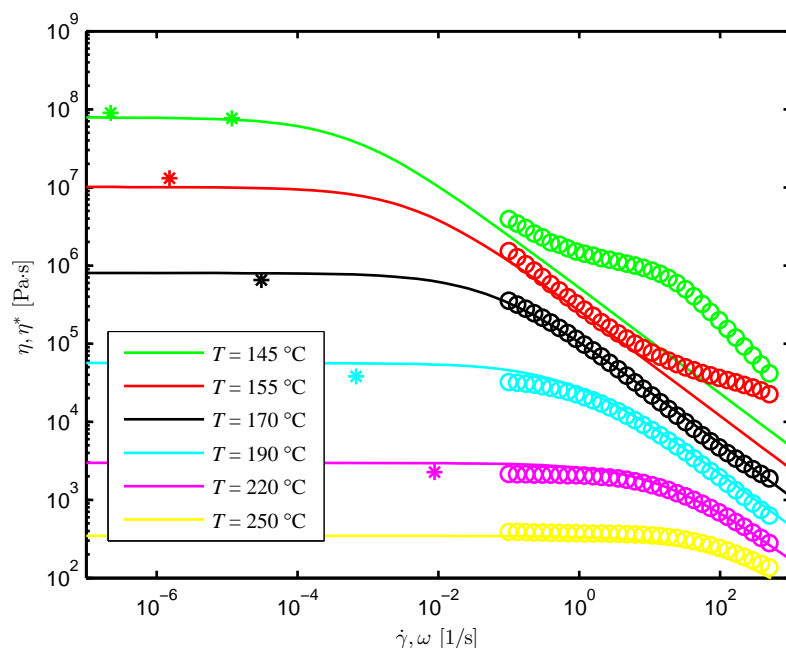


Figure 5.1: Shear viscosity as a function of shear rate and temperature for the COC 5013S-04. Circles: Measured complex viscosity. Asterisks: Measured zero-shear viscosity. Solid lines: Fitted Cross-WLF model.

Only two of the three first parameters are independent so that for example the reference temperature can be chosen freely. The viscosity is shear rate independent in the so-called plateau region where  $\dot{\gamma}\eta_0 \ll \tau^*$  and follows a power-law model ( $\eta = a\dot{\gamma}^{n-1}$ ) for  $\dot{\gamma}\eta_0 \gg \tau^*$ . Large databases exist where Cross-WLF parameters are tabulated for different polymers (provided for example by Moldflow Co.). The database parameters are obtained by testing the polymer in a capillary rheometer or modified injection molding machines at relevant processing conditions i.e. in the melt temperature interval recommended by the polymer manufacturers and relatively high shear rates.

Polymer microfeatures partly form at temperatures significantly below what is typically referred to as the processing temperature, even at temperatures close to the glass transition as is seen in Paper C. Because of this it was necessary to perform our own rheological measurements for the simulation study and not rely on extrapolation of data from other sources. When comparing our measured values with tabulated values it was seen that they agreed relatively well at high shear rates and high temperatures but deviated strongly at low temperatures (up to a factor 100 in viscosity).

It can be seen in figure 5.1 that for COC the viscosity is relatively well described by the Cross-WLF model for temperatures down to around 170 °C. Below this, there is a threshold frequency, above which the viscosity is higher than what would be expected from the model. This deviation happens as the polymer passes through the frequency dependent glass transition. This behavior was also seen for the other amorphous polymers tested in Paper E.

### 5.1.3 Flow front tracking

In the simulations performed in this work, an Eulerian description has been used to track the polymer flow front. This means that the domain is discretized with a mesh and, during the simulations, the mesh is kept stationary while the fluid passes through it. The alternative would be to use a Lagrangian description, where the mesh moves with the fluid flow. How a moving interface is captured in these two formulations is fundamentally different.

In the Lagrangian formulation, the interface is well defined and tracked in time. The main reason why such a formulation is not commonly used in injection molding simulations, is that it is difficult to handle large deformations. As the interface is deformed, as for example in a bifurcation or the fountain flow region, a Lagrangian mesh will be deformed with it. After some time, the mesh elements will be distorted and hence the discretization error will increase. To reduce this error, a computationally expensive remeshing has to be performed.

In an Eulerian formulation, the interface is not tracked explicitly in time. The location of each phase is tracked using a phase variable and its value is used to reconstruct the interface. The method that was used in Paper B and Paper C is similar to the Volume of Fluid method proposed by Hirt and Nichols [37]. Additional phase variables  $\phi_i$  are introduced and are convected through the domain.

$$\frac{\partial \phi_i}{\partial t} + \mathbf{U} \cdot (\nabla \phi_i) = 0 \quad (5.9)$$

Initially, the phase variable  $\phi_i$  takes the value 1 in phase  $i$  and the value 0 elsewhere. Even though there is initially a sharp step in the phase variable, numerical diffusion will always lead to some blurring of the interface. The physical properties of the fluid, such as the viscosity, are then taken as a linear interpolation over the phase variable.

$$\eta = \sum_i \phi_i \eta_i \quad (5.10)$$

When studying the performance of the micromixer, there was only a one-way coupling between the flow field and the phase variable, since both phases had the same physical properties (water). However, in the injection molding simulation study, the two phases are a molten polymer and air with very different physical properties. In that case, there is a two-way coupling between equation 5.9 and equations 5.1 – 5.3.

### 5.1.4 Multiscale modeling

For microfeatured parts, the ratio in size between the whole part and its features is too large to be handled in a single injection molding simulation. This is partly because of the large difference in length scale, but also due to the large difference in time scale. Modeling the system requires a multiscale approach as discussed in Paper C. First a filling simulation is performed on the macroscale and the pressure information from this macroscale simulation is used as a boundary condition on the microscale. We describe this as a one way coupling from macro to microscale. This is rationalized by the fact that the size of the microfeatures is much smaller than the thickness of the macroscopic part.

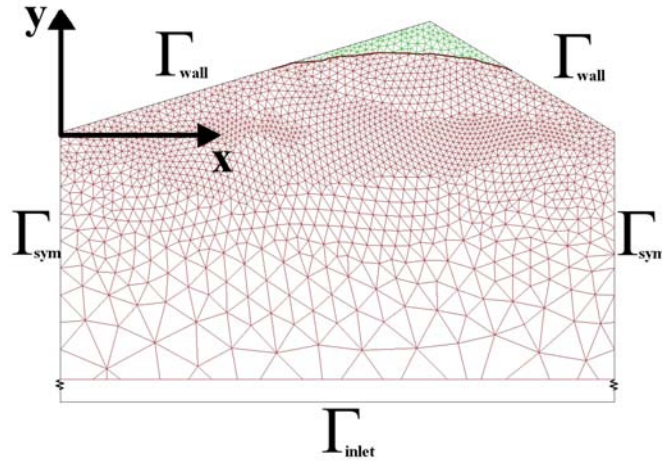


Figure 5.2: Domain and boundary conditions for the microscale part of the simulations in Paper C. The mesh is shown and colored red in regions where polymer is present, green in areas filled with air.

### 5.1.5 Microscale boundary conditions

In figure 5.2, the geometry and mesh of the microscale simulation are shown. The detailed description of the boundary conditions are given in Paper C. The time dependent pressure from the macroscale simulation is applied at the boundary  $\Gamma_{\text{inlet}}$ . In contrast to other studies in the field, where the pressure is applied at a location similar to  $y = 0$  [38, 39], this procedure takes account of the pressure drop occurring close to the inlet.

At the wall,  $\Gamma_{\text{wall}}$ , a no-slip condition is applied for the polymer and a constant heat transfer coefficient is used for the thermal boundary condition. The value of the coefficient was chosen so that simulated replications matched the experimental values using reverse engineering. This procedure was chosen due to lack of experimental data for the microscale heat transfer coefficient. As is discussed in Paper C, the value of the coefficient will be scale dependent.

In addition there were two symmetry boundary conditions  $\Gamma_{\text{sym}}$  which are modeled as frictionless, adiabatic walls.

### 5.1.6 Mold heating

As was discussed in the section on injection molding, temperature control is partly the key to good replication of microfeatures. However, in classical injection molding simulations, the mold temperature is approximated to be constant during the filling phase. Such an approximation is possible because of two characteristics of the injection molding process; 1.) the thermal conductivity, mass and heat capacity of the mold is much larger than that of the polymer and 2.) the cooling of the polymer melt is small and locally bounded to the area close to the wall and thus have only a limited influence on the flow field. Thus, there is 1.) only a small change in mold surface temperature and 2.) the flow field is relatively insensitive to a change in mold surface temperature. For the replication of microfeatures, it was seen in the experimental study in Paper A, that even small changes in the mold temperature can lead to significant changes in the microfeature replication. Because of this sensitivity, even though the temperature rise is still modest, also the heating of the mold wall was included in Paper

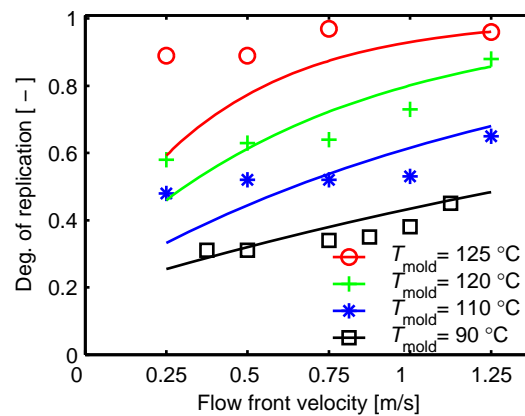


Figure 5.3: Comparing simulated (solid lines from Paper C) and experimental (symbols from Paper A) replication of the Tomra DOE. The part is molded in a COC material using different values for the mold temperature and injection velocity.

C. The temperature increase of the mold wall was predicted from the simulations to be relatively small (below 5 °C), but even this was enough to significantly change the replication of the microfeatures.

## 5.2 Simulation conclusions

Using the multiscale approach, a good agreement was found between the simulated replication of the microscale grating and the experimental measured replication as can be seen in figure 5.3. Going back to the three challenges stated at the beginning of this chapter, I will try to estimate how well the challenges are addressed within the present model.

- The viscosity of the polymer is much better described than what would have been the case if using tabulated values for the Cross-WLF model. Still, the rheology is not well described through the glass transition. Below the transition, the viscosity is higher than what is predicted from the model and the relaxation times of the polymer are close to the system time scale, making elastic effects important.
- The heat transfer condition is not rigorously founded. Reverse engineering is used to estimate its value. Even though this approach is used also in other studies in the field, the method is questionable.
- The coupling between the macroscale and microscale seems to capture the process relatively well compared to other studies in the field. By moving the microscale entrance away from  $y = 0$ , the pressure loss occurring close to the entrance is included.



## 6 CONCLUSIONS

This thesis has in detail investigated how injection molding processing conditions influence the replication of microfeatures. In Paper A, a new method for characterizing the replication of injection molded parts was introduced. This measure made it possible to investigate a large number of parts with a high accuracy. The mold temperature is an important factor influencing the replication, and the sensitivity increases when the mold temperature is close to the glass transition temperature of the polymer. The injection velocity also has a positive effect on the replication. Both these effects were described previously in the literature.

In Paper C, a new simulation method was developed, which captures well how processing settings influence the replication of microfeatures. The simulations show that much of the polymer deformation, leading to the replication of microfeatures, occurs close to the glass transition temperature of the polymer. In this temperature range, elastic effects start to become important. A more realistic description of the process would probably require a viscoelastic constitutive equation.

As indicated by the simulations in Paper C, it was seen in Paper F that the elastic effects really are important and the paper studies these effects in detail. It is shown that the holding pressure, which generally is assumed to have a positive effect on replication, can actually worsen the definition of the microfeatures. The reason for this is linked to the elastic recoil taking place after the holding pressure is released.

In Paper E, it is investigated how the zero shear rate viscosity depends on the temperature for different amorphous polymers. When simulating polymer processing as in Paper C, it would have been a great advantage if a recent proposal of a universality of the temperature dependence for polymer chain relaxation times was correct. Our rheological measurements do not support such a universality.

In Paper D, work has been done developing a new lab-on-a-chip platform, which can rapidly be mass produced using injection molding.

In Paper B, a new proposal is made for a microfluidic mixer that folds layers of different fluids together. The mixer is designed to have a simple and open layout which facilitates replication by for example injection molding and allows for easy implementation in lab-on-a-chip designs. The mixer is verified to work well by using a numerical model and by investigating the flow field directly in manufactured prototypes.



# BIBLIOGRAPHY

- [1] Feynman, R. *Engineering and Science* **23**, 22 – 36 (1960).
- [2] Gadegaard, N., Mosler, S., and Larsen, N. *Macromol. Mater. Eng.* **288**(1), 76 – 83 (2003).
- [3] Park, S., Lee, D., Xu, J., Kim, B., Hong, S., Jeong, U., Xu, T., and Russell, T. *Science* **323**(5917), 1030 – 1033 (2009).
- [4] Puukilainen, E., Rasilainen, T., Suvanto, M., and Pakkanen, T. *Langmuir* **23**(13), 7263 – 7268 (2007).
- [5] Ting, C.-J., Chen, C.-F., and Chou, C. *Opt. Commun.* **282**(3), 434 – 438 (2009).
- [6] Whitesides, G. *Nature* **442**(7101), 368 – 373 (2006).
- [7] Compton, J. *Nature* **350**(6313), 91 – 92 (1991).
- [8] Nguyen, N. and Wu, Z. *J. Micromech. Microeng.* **15**(2), R1 – R16 (2005).
- [9] Løvhaugen, O., Johansen, I.-R., Bakke, K., Fismen, B., and Nicolas, B. *J. Mod. Opt.* **51**(14), 2203 – 2222 (2004).
- [10] Sha, B., Dimov, S., Griffiths, C., and Packianather, M. *J. Mater. Process. Tech.* **183**, 284 – 296 (2007).
- [11] Mönkkönen, K., Hietala, J., Paakkonen, P., Paakkonen, E., Kaikuranta, T., Pakkanen, T., and Jaaskelainen, T. *Polym. Eng. Sci.* **42**(7), 1600 – 1608 (2002).
- [12] Han, X., Yokoi, H., and Takahashi, T. *Int. Polym. Proc.* **21**(5), 473 – 479 (2006).
- [13] Su, Y.-C., Shah, J., and Lin, L. *J. Micromech. Microeng.* **14**(3), 415 – 422 (2004).
- [14] Yokoi, H., Han, X., Takahashi, T., and Kim, W. *Polym. Eng. Sci.* **46**(9), 1140 – 1146 (2006).
- [15] Eriksson, T. and Rasmussen, H. *J. Non-Newtonian Fluid Mech.* **127**(2-3), 191 – 200 (2005).
- [16] Murakami, O., Kotaki, M., and Hamada, H. *Polym. Eng. Sci.* **48**(4), 697 – 704 (2008).
- [17] Kalima, V., Pietarinen, J., Siitonen, S., Immonen, J., Suvanto, M., Kuittinen, M., Mönkkönen, K., and Pakkanen, T. *Opt. Mater.* **30**(2), 285 – 291 (2007).

- [18] Xu, G., Yu, L., Lee, L., and Koelling, K. *Polym. Eng. Sci.* **45**(6), 866 – 875 (2005).
- [19] Han, X. and Yokoi, H. *Polym. Eng. Sci.* **46**(11), 1590 – 1597 (2006).
- [20] Pranov, H., Rasmussen, H., Larsen, N., and Gadegaard, N. *Polym. Eng. Sci.* **46**(2), 160 – 171 (2006).
- [21] Yao, D., Chen, S.-C., and Kim, B. *Adv. Polym. Technol.* **27**(4), 233 – 255 (2008).
- [22] Michaeli, W. and Gartner, R. *J. Polym. Eng.* **26**(2-4), 161 – 177 (2006).
- [23] Brunelle, D. In *Encyclopedia of Polymer Science and Technology, 3rd edition*, Mark, H. F., editor, volume 7. Wiley-Interscience (2003).
- [24] Tofteberg, T. and Andreassen, E. In *Annual Meeting of the Polymer Processing Society* (PPS, Salerno, 2008).
- [25] Ding, Y. and Sokolov, A. *Macromolecules* **39**(9), 3322 – 3326 (2006).
- [26] Liu, C., He, J., Keunings, R., and Bailly, C. *Macromolecules* **39**(25), 8867 – 8869 (2006).
- [27] Sokolov, A. and Schweizer, K. *Phys. Rev. Lett.* **102**(24), 248301 (2009).
- [28] Ngai, K., Plazek, D., and Roland, C. *Phys. Rev. Lett.* **103**(15), 159801 (2009).
- [29] Sokolov, A. and Schweizer, K. *Phys. Rev. Lett.* **103**(15), 159802 (2009).
- [30] Williams, M., Landel, R., and Ferry, J. *J. Am. Chem. Soc.* **77**(14), 3701 – 3707 (1955).
- [31] Ferry, J. *Viscoelastic properties of polymers*. John Wiley & Sons, Inc., New York, 3rd edition, (1980).
- [32] Ohlsson, R., Wihlborg, A., and Westberg, H. *Int. J. Mach. Tool. Manu.* **41**(13-14), 1899 – 1907 (2001).
- [33] Binnig, G., Quate, C., and Gerber, C. *Phys. Rev. Lett.* **56**(9), 930 – 933 (1986).
- [34] Gross, L., Mohn, F., Moll, N., Liljeroth, P., and Meyer, G. *Science* **325**(5944), 1110 – 1114 (2009).
- [35] Soles, C. and Ding, Y. *Science* **322**(5902), 689 – 690 (2008).
- [36] Rowland, H., King, W., Pethica, J., and Cross, G. *Science* **322**(5902), 720 – 724 (2008).
- [37] Hirt, C. and Nichols, B. *J. Comput. Phys.* **39**(1), 201 – 225 (1981).
- [38] Kim, D., Lee, H., Lee, B., Yang, S., Kwon, T., and Lee, S. *Polym. Eng. Sci.* **46**(4), 416 – 425 (2006).
- [39] Young, W. *Appl. Math. Model.* **31**(9), 1798 – 1806 (2007).

## PART II

### INCLUDED PAPERS



# PAPER A

Terje Tofteberg, Hélène Amédéo and Erik Andreassen

## **Injection molding of a diffractive optical element**

*Polymer Engineering & Science*, Volume 48, Issue 11, pages 2134 – 2142 (2008)



# Injection Molding of a Diffractive Optical Element

Terje Tofteberg, H el ene Am edro, Erik Andreassen  
SINTEF Materials and Chemistry, Oslo, Norway

**The injection molding of a microfeathered component, a diffractive optical element, was studied. The component has a wave-like pattern on the surface, with amplitude 0.5  $\mu\text{m}$  and wavelength 3  $\mu\text{m}$ . Two different polymers were used: a polymethylmethacrylate and an ethylene-norbornene copolymer (cyclic olefin copolymer). The topography was investigated using white light interferometry (WLI), atomic force microscopy (AFM), and scanning electron microscopy (SEM). A new WLI-based technique is proposed for rapid quantification of the replication of periodic surface patterns. This technique gives almost the same information regarding the degree of replication as AFM but can be performed much faster. Quantitative data on the degree of replication as function of processing conditions are presented. At optimal conditions, almost perfect replication is obtained using both materials. At suboptimal conditions, it is observed that the degree of replication increases with increasing injection velocity and increasing mold temperature, with similar characteristics for both materials. The difference in replication quality between the two materials seems to be related to the different temperature dependencies of the viscosities. POLYM. ENG. SCI., 48:2134–2142, 2008.   2008 Society of Plastics Engineers**

## INTRODUCTION

In his visionary talk “There’s plenty of room at the bottom” given in 1959 at Caltech, Richard Feynman suggested plastic materials as ideal candidates for rapid replication of parts with micro- and nanosized features [1]. Today, such parts are mass produced using different technologies, and the most common are injection molding and hot embossing.

Our research addresses challenges regarding the use of polymer materials in injection-molded, high-precision components. The focus is on components with the largest outer dimension in the centimeter range, but with features (channels, gratings, etc.) in the micrometer range. We refer to these as microfeathered components.

This study is based on molding trials with a diffractive optical element (DOE). The DOE design was described

by L ovhaugen et al. [2]. It is an essential part of a low-cost infrared spectrometer, which for example, can be used to identify different types of polymers. The molded DOE works in reflection and it is sputtered with a thin gold layer after molding to have the required reflectance.

Other products with micrometer and submicrometer sized features fabricated using injection molding include optical storage media such as the CD, the DVD, and the Blu-ray Disc, where the accurate replication of microfeatures using injection-compression molding is essential for the product quality. The physical properties of a surface can also be altered dramatically by shaping it on the microscale, for instance, to produce superhydrophobic surfaces [3].

No limit has yet been set, as to how small features that can be replicated using injection molding. Fibrillar structures with details down to 10 nm [4] were replicated by injection molding, as well as characteristic wave patterns from deep reactive ion etching with features down to 5 nm [5]. However, both these structures had very low aspect ratios ( $\ll 1$ ). For some submicrometer structures, it has been suggested that the adhesive energy between the polymer and the mold (insert) may be an important factor for the replication [6].

Several authors have reported that increasing mold temperature and injection velocity improves the replication of microfeatures [6–14]. However, only limited quantitative data exists on how the mold temperature and the injection velocity influence replication. On the other hand, too high mold temperatures can damage microfeatures [15], high mold temperatures will increase the cycle time [16], high injection velocity may lead to poor surface quality [17], and the injection velocity is limited by the injection molding machine. This makes it important to obtain quantitative data, linking process parameters with replication quality, in order to optimize the injection molding of parts with microfeatures.

Other process parameters do also affect the replication. It has been demonstrated that higher melt temperature [7, 17, 18] and higher holding pressure [7, 18] can have a positive effect. There is also a coupling between process and geometry including microfeatures. Some examples: the effect of holding pressure increases with increasing cavity thickness [7]. Grooves parallel to the flow direction are easier to replicate than those perpendicular to the flow

Correspondence to: Terje Tofteberg; e-mail: terje.tofteberg@sintef.no  
Contract grant sponsor: Research Council of Norway.  
DOI 10.1002/pen.21154  
Published online in Wiley InterScience (www.interscience.wiley.com).  
  2008 Society of Plastics Engineers

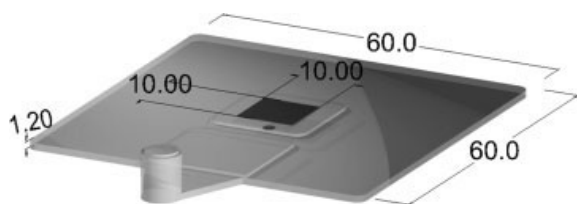


FIG. 1. A drawing of an injection-molded part with some dimensions indicated in millimeters. The microfeatures are in the central square area (10 mm  $\times$  10 mm). A combined pressure and temperature sensor is mounted in the mold half opposite the Ni shim, in the position marked with a dark gray circle (just in front of the square with microfeatures).

[7, 18, 19]. Features near the gate may [7, 20] or may not [17] be easier to replicate, e.g. depending on the aspect ratio of the microfeatures. Flow instabilities that reduce the replication quality of certain microfeatures occur at certain processing conditions [6, 21].

Special techniques and equipment can be used to improve the quality of injection molded microfeatured parts (microsized parts is not the topic of this study). Variotherm processing (variation of the mold temperature through the cycle), evacuation of the air inside the cavity prior to injection, and injection-compression molding are the most common techniques. Several groups have developed and studied variotherm processes. In these processes the cavity surface is heated, prior to injection to enhance the replication, and then cooled in order for the polymer to reach the ejection temperature. For amorphous polymers, the cavity surface is typically heated to temperatures above the glass transition temperature. The cavity surface can be heated from the interior of the mold (by circulating liquids or electrical heating) or from the surface. A smaller mass is heated with the latter techniques, giving shorter cycle times. Implementations of surface heating include induction heating [22], proximity effect heating [23], and infrared heating. Positive effects on product quality have also been reported with cavity evacuation [7, 9, 19] and injection-compression molding [24].

In the present study, conventional injection-molding equipment was used. The effect of mold temperature and injection velocity on the replication quality is studied.

## EXPERIMENTAL

### Part Geometry and Mold Insert

The geometry of the injection molded part can be seen in Fig. 1. The area with microfeatures was 10 mm  $\times$  10 mm. A microstructured mold insert was clamped in a modular base mold. The mold insert was a 0.3-mm-thick Ni shim made by electroplating a resist structured by electron beam lithography [2]. The surface topography of the shim was an irregular wave pattern with wave height  $\sim$ 500 nm and wavelength 3  $\mu$ m.

### Polymers

Two different amorphous materials were used in the injection molding trials. Both of them had a good ability to replicate microstructures, according to the manufacturers. The materials were a polymethylmethacrylate (PMMA; Plexiglas POQ62 from Evonik Röhm) and an ethylene-norbornene copolymer, often referred to as a cyclic olefin copolymer (COC; Topas 5013S-04 from Topas Advanced Polymers). The latter had about 50 mol% norbornene [25]. The glass transition temperatures are given in Table 1.

### Injection Molding

The injection molding was performed on a servoelectric Battenfeld EM 50/120 machine with maximum clamping force 500 kN and screw diameter 25 mm. The injection velocity and the mold temperature were varied. All other molding parameters were kept constant. An overview of the parameters used is shown in Table 1. Note that in this article, injection velocity is defined as the flow front velocity given as the volume flow divided by the cross sectional area where the microfeatures are located. It has been shown that, at high injection rates, the relationship between volume flow (cm<sup>3</sup>/s) and flow front velocity (mm/s) is not completely linear [9], probably because of compression effects. This possible effect is not included when specifying the flow front velocity. Also note that both polymers were molded with a melt

TABLE 1. Materials and processing parameters.

Grade	Polymer type	$T_g^a$ (°C)	Mold temp. <sup>b</sup> (°C)	Injection velocity <sup>c</sup> (mm/s)	Melt temp. <sup>d</sup> (°C)	Holding pressure (MPa)
Plexiglas POQ62	PMMA	99.6	40–80	130–1200	240	60
Topas 5013S-04	COC	130.0	60–125	130–1300	270	50

<sup>a</sup> Glass transition temperature measured using DSC at heating rate 10°C/min. Sample first heated to above  $T_g$ , cooled down, and then heated again.

<sup>b</sup> Recommended mold temperatures: 60–90°C (the PMMA) and 95–125°C (the COC).

<sup>c</sup> This is the melt front speed through the cross-section with microfeatures, i.e. volume flow divided by cross-sectional area.

<sup>d</sup> The temperature set for the last cylinder element and the nozzle, confirmed by measurements in the barrel end cap (using a Kistler 4083A sensor).

temperature 140 K above their respective glass transition temperatures.

The volume flow was kept constant during injection, and the switchover to holding pressure was set to occur when a specified volume had been injected. This nominal switchover volume was the same for all trials within one polymer series. It should be noted, however, that there is a certain retardation time involved for the injection velocity to reach zero. At the highest injection velocities, the extra volume filled during this retardation time is not insignificant. Hence, for high injection velocities, the real switchover volume is higher than the nominal value, and it increases with increasing injection velocity.

For each change of injection velocity, five shots were made before taking the sixth as characteristic for that setting. For one setting using PMMA, the degree of replication was measured for shots 6–15, and it was seen that the replication varied only slightly and no trend was observed. More details can be found in the Results section.

The mold temperature was controlled using circulating water at a constant temperature, and the mold temperatures reported later refer to the set water temperature. A combined temperature and pressure sensor (Kistler 6190BA) located in the mold surface opposite to the microfeatures confirmed that this was also close ( $\pm 2^\circ\text{C}$ ) to the surface temperature when the melt was injected. Some temperatures that were significantly outside the recommended settings were tested, in order to check how this influenced the replication of the microfeatures. When changing the water temperature, the mold temperature was allowed to stabilize, so that the maximum and minimum temperature of the mold within a cycle did not change from cycle to cycle.

#### Characterization of Molded Parts Using AFM, SEM, and WLI

The surface topographies of parts and of the Ni shim were characterized by atomic force microscopy (AFM), scanning electron microscopy (SEM), and white-light interferometry (WLI).

AFM was performed in tapping mode. The instrument was a Dimension 3100 from Digital Instruments. A tetrahedral tip (DP14/GP/AIBS from MicroMasch) was used. The same peak near the middle of the microfeatured area was investigated on molded parts and on the shim.

The SEM instrument was a Quanta 600 FEG from FEI Company. Before the parts were investigated by SEM, a 50-nm-thick gold layer was sputtered on the surface.

The WLI instrument was a WYKO NT-2000 from Veeco Instruments. To measure the replication quality,  $45\ \mu\text{m} \times 60\ \mu\text{m}$  images near the center of the microfeatured area were recorded. The parts were manually aligned, so that the pictures were taken from almost the same location ( $\pm 3\ \mu\text{m}$ ) for all parts. WLI is a coarser method than AFM, and the lateral resolution depends

on the microscope used. In our case, the resolution was  $0.5\ \mu\text{m}$  in the plane and 10 nm in the vertical direction. WLI can however, as will be shown, be used to estimate the degree of replication within the same accuracy as AFM. We do this by not only considering a single peak in the topography, but also doing a Fourier transform of the entire image. Details are given in the next section.

#### Degree of Replication From WLI Measurements

The topography of a DOE can be described by a function  $h = f(x,y)$  which gives the height  $h$  as a function of the spatial coordinates  $x$  and  $y$ . We first assume that the topography is periodic, where we have aligned the coordinate axes so that there exists a  $P$  for which  $f(x,y + P) = f(x,y)$  for all  $x$  and  $y$ . The power spectral density (PSD)  $\Phi(\omega,x)$  of such a continuous function taken in the  $y$ -direction is given along any line parallel to the  $y$ -axis as

$$\Phi(\omega,x) = \left| \frac{1}{\sqrt{2\pi}} \int_{-\infty}^{\infty} f(x,y) e^{-i\omega y} dy \right|^2 = \frac{F(\omega,x)F^*(\omega,x)}{2\pi}, \quad (1)$$

where  $F(\omega,x)$  is the Fourier transform of  $f(x,y)$  and  $F^*(\omega,x)$  is its complex conjugate. For an electromagnetic or acoustic wave,  $\Phi(\omega,x)$  is proportional to the amount of energy carried by given frequencies, therefore, the prefix power. For a 2D periodic pattern, the PSD gives information about the strength of the signal at the given frequency. Before discussing the difficulties coming from the fact that our signal is finite, discrete, and not perfectly periodic, we show how the degree of replication could be defined in the ideal case.

Figure 2 shows how the PSD transformation works on a periodic saw-tooth signal. The first observation to be made is that the largest peak is located at the inverse of the characteristic wavelength of the saw-tooth pattern. This is clearly seen when restoring the signal using the inverse Fourier transform of the truncated spectrum. The next peaks are located at integer multiples of this frequency and corresponds to the coefficients of the Fourier series of the saw-tooth signal. We define the degree of replication  $\alpha$  as

$$\alpha = \frac{\sqrt{I_{\text{DOE}}}}{\sqrt{I_{\text{shim}}}}, \quad (2)$$

where  $I$  is the integral of the largest peak in  $\Phi(\omega,x)$ . This integral is proportional to the square of the amplitude of the signal in Fig. 3.

In our case, the topography is measured by WLI as a discrete signal of finite extension. To be able to define the PSD from Eq. 1, the discrete version of the Fourier transform must be used. There is also a challenge in the fact that the topography is not completely periodic. An exam-

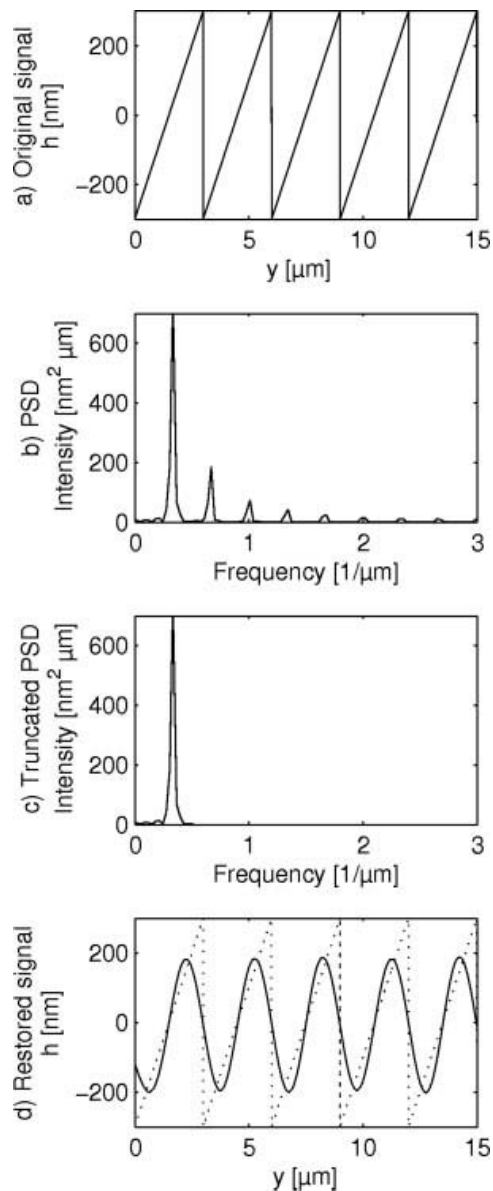


FIG. 2. An illustration of the PSD function. (a) Original saw-tooth signal, (b) PSD of the saw-tooth signal, (c) truncated spectrum used for calculating the degree of replication, (d) restored signal based on the truncated PSD.

ple of the topography as measured by WLI is shown in Fig. 3. Since not all lines parallel to the  $y$ -axis are equal, we found it most useful to define the PSD as an average over all  $x$ -values.

There are some advantages with this method compared to using AFM and comparing the structures on the molded part with the corresponding (but negative) structures on the Ni shim. The PSD from WLI includes statistical information representing an area, and all the information is used to define the degree of replication. Hence, this method gives a better statistical average for the degree of replication than AFM studies, where only a few peaks/profiles are analyzed. In addition, the WLI measure-

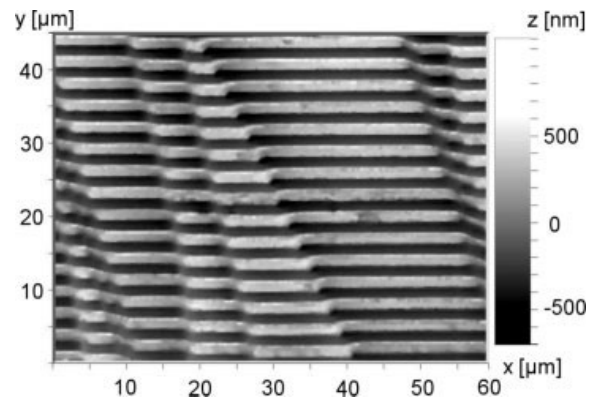


FIG. 3. Topography by WLI for a molded PMMA DOE.

ments are fast, typically on the order of a second, once the alignment and focusing is done, compared to the relatively slow AFM that needs to scan the surface pixel by pixel.

However, a scalar variable is not able to capture the full complexity of a surface, neither is the typical resolution of WLI good enough to capture as fine details as AFM. Still the WLI/PSD method allows for rapid and adequate analysis of a large number of parts.

## RESULTS

### *Degree of Replication Versus Processing Conditions*

A high degree of replication was obtained with the PMMA, with mold temperatures in the interval recommended by the manufacturer, i.e. 60–90°C. Figure 4 shows how the replication improves when increasing the injection velocity and the mold temperature. These results indicate that the processing window, giving good replication, is quite broad. Hence, there is some freedom to

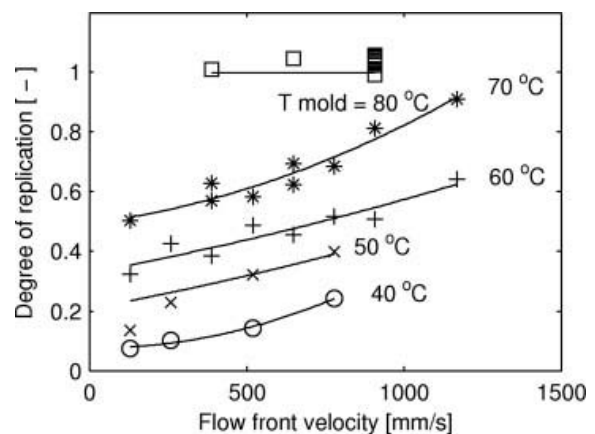


FIG. 4. The degree of replication as measured using WLI/PSD for PMMA DOEs as function of mold temperature and flow front velocity. The lines are guides for the eyes. With a mold temperature of 80°C and a flow front velocity of 900 mm/s, 10 consecutively molded samples were analyzed, see main text for details.

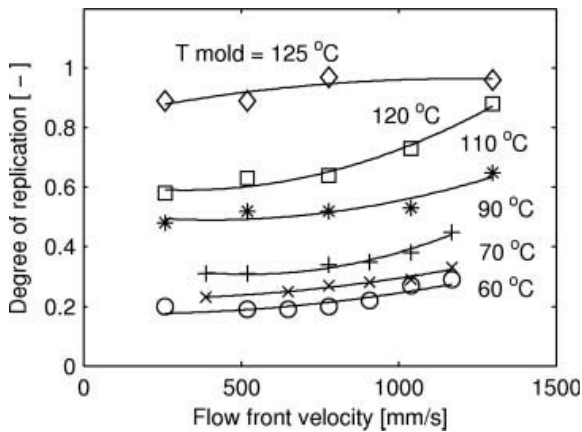


FIG. 5. The degree of replication for COC DOEs as a function of mold temperature and flow front velocity. The lines are guides for the eyes.

change processing conditions to meet other criteria. Also with the COC it was possible to achieve a high degree of replication, but as can be seen in Fig. 5, the mold temperature had to be set to the maximum of the recommended range.

When comparing the two polymers regarding the effect of mold temperature on replication there are two main observations. (1) For high mold temperatures (near  $T_g$ ), the PMMA gives better replication than the COC for a given difference between mold temperature and  $T_g$ . (2) The effect of mold temperature on replication is higher for the PMMA than for the COC. Note that both Fig. 4 and Fig. 5 contain data for the mold temperatures ( $T_g - 20$  K), ( $T_g - 40$  K), and ( $T_g - 60$  K).

When the surface of the polymer solidifies it can be in contact with the Ni shim or not, and the resulting surface textures are different, as shown in the SEM picture in Fig. 6.

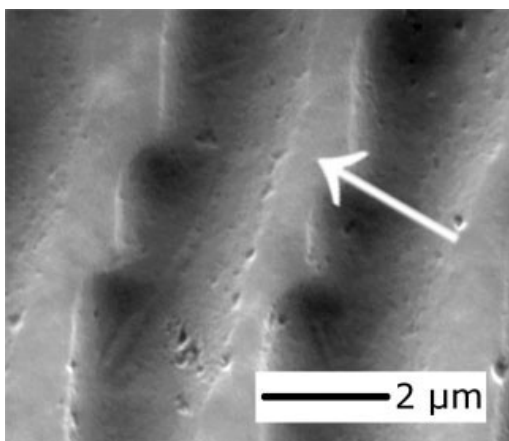


FIG. 6. SEM picture of a molded COC DOE. Three periods of the diffractive grating are seen. The degree of replication (from WLI) is 0.72. On the top of the ridges (white arrow), where the polymer was not in contact with the Ni shim when solidifying, the texture appears different.

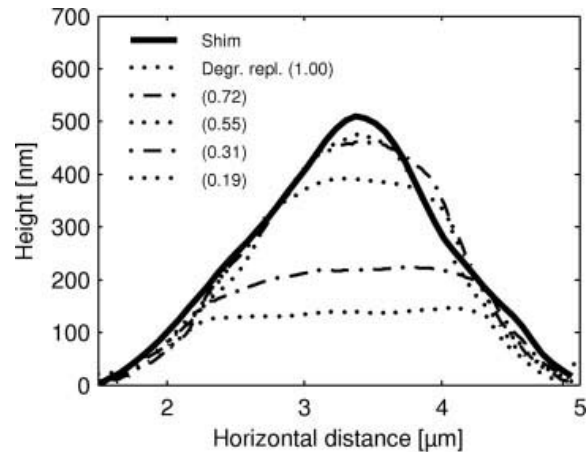


FIG. 7. AFM data for the same peak on different injection-molded PMMA parts, and on the Ni shim (inverted data). The numbers in the legend refer to the degree of replication determined by the WLI/PSD method.

#### Verification of the Degree of Replication Obtained With the WLI Method

The degree of replication obtained with the WLI/PSD method was compared with AFM data for one specific wave. As shown in Fig. 7, the degree of replication obtained with WLI/PSD correlates well with the peak height measured with AFM, justifying the use of the WLI/PSD method to quantify the degree of replication. The fact that the given degree of replication varies smoothly with the processing parameters, as shown in the previous section, also speaks for its validity.

Since the WLI measurements were based on manual alignment of the sample, all measurements were not taken at the exact same location on the DOE. To see how this influenced the results, one PMMA part was manually aligned and analyzed 10 times. These 10 values for the degree of replication had a standard deviation of 1.7%. For comparison, 10 consecutively molded PMMA parts (same molding parameters) were analyzed. The standard deviation of the degree of replication values from these 10 trials was 1.9%. Note that the difference between consecutively molded parts is not significantly larger than the uncertainty of the measurements.

## DISCUSSION

The degree of replication increases with increasing mold temperature and injection velocity for the two polymers in this study. The replication of the microfeatures can only take place as long as the polymer has sufficient fluidity.

#### How the Mold Temperature Influences the Replication

A high mold temperature will increase the degree of replication by keeping the polymer at a sufficiently low

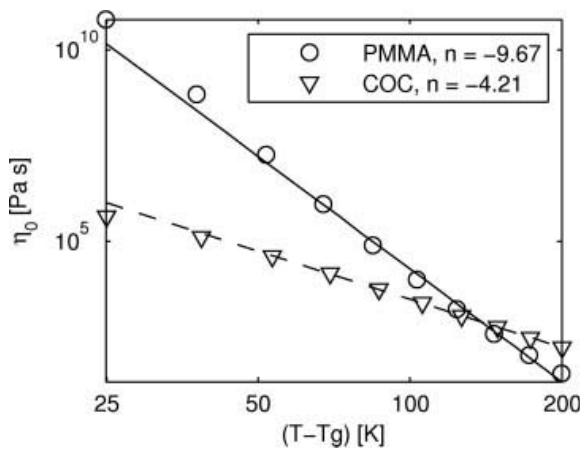


FIG. 8. Log-log plot of zero shear rate viscosity as function of temperature. Both polymers were injected with a melt temperature of  $(T_g + 140)^\circ\text{C}$  (Table 1) and thus had similar viscosities. The slope  $n$  is defined from  $\log \eta = n \log(T - T_g) + \log b$ .

viscosity for a longer time. The magnitude of this effect depends on how fast heat is transferred from the hot polymer to the mold wall. The most common way to describe this heat transfer is to use a heat-transfer coefficient, saying that the heat flow is proportional to the temperature difference between the polymer and the wall. In a numerical simulation, the degree of replication of microfeatures will generally depend significantly on the value chosen for the heat-transfer coefficient; see e.g. Ref. [12]. Still there is no consensus regarding which value to use, and experimental evidence suggests that the value changes during the injection-molding cycle [26].

How much the polymer properties change with temperature will also be important for how the mold temperature influences replication. Figure 8 shows viscosity at zero shear rate versus temperature for the two polymers, based on Cross-WLF data from the Moldflow database [27]. The temperature dependence of the viscosity is stronger for the PMMA than for the COC. The difference between the two materials depends on the shear rate and becomes small above  $\sim 100 \text{ s}^{-1}$ . However, the deformation rates can be low during the filling of the last remaining volume of the microfeatures, as the pressure builds up after the melt front has passed (discussed in the next section).

The observation that the PMMA gives better replication than the COC at high mold temperatures (relative to the respective glass transitions) could be due to its lower viscosity at high temperatures and low shear rates. The zero shear viscosity curves in Fig. 8 cross at  $(T - T_g) \sim 130 \text{ K}$ . The crossing point moves to higher temperatures with increasing shear rate. At a shear rate of  $10 \text{ s}^{-1}$ , the curves cross above  $(T - T_g) = 140 \text{ K}$ , which is the melt temperature in the molding trials. However, with high mold temperatures, the lower PMMA viscosity at low rates and high polymer temperatures could account for the higher degree of replication with this polymer com-

pared to the COC. Shear heating could also contribute to the temperature being above the crossing point. It should, however, be noted that capillary rheometry data at low shear rates, and the extrapolation to zero shear rates, are uncertain. Further work is planned to characterize the rheology of these polymers, including the behavior near the glass transition and the effective no-flow temperature.

The observation that the effect of mold temperature on replication is higher for the PMMA than for the COC could be explained by the viscosity curves in Fig. 8. Our hypothesis is that the change in replication when changing the mold temperature is related to the temperature dependence of the viscosity. The PMMA has a steeper curve in Fig. 8. Hence, a given reduction in mold temperature will result in a larger viscosity increase for this polymer than for the COC.

Other thermal properties of the polymers may also affect the replication. The basic thermal parameters are thermal conductivity, specific heat capacity, and density. The PMMA in this study has higher specific heat capacity and density than the COC, also if the values are compared at a certain temperature above the respective glass transitions. The values for the thermal conductivity are not so clear. The two polymers have roughly the same conductivities in the Moldflow database. Other published values vary substantially for given polymer types or grades, probably because of different measurement techniques and experimental uncertainty.

The thermal diffusivity, i.e., the ratio of thermal conductivity to the product of specific heat capacity and density, is important in the injection-molding process. The thickness of the solidified layer is often found to be proportional to the square root of the thermal diffusivity. In our study, the PMMA has lower thermal diffusivity than the COC. This could contribute to the good replication with the PMMA at high mold temperature, but cannot explain why the replication with PMMA is more sensitive to mold temperature, at least not without taking into account the variation of the thermal diffusivity with temperature. For the replication of microfeatures, the heat-transfer coefficient (or other entities describing local effects near the boundary) seems to be more important than the thermal diffusivity. Yoshii et al. [20] found no correlation between thermal diffusivity and degree of replication for four amorphous polymers.

The thermal effusivity, i.e., the square root of the product of thermal conductivity, specific heat capacity, and density, determines, in an idealized case, the contact temperature between the polymer and the mold (shim) [20]. The PMMA has somewhat higher thermal effusivity than the COC, but the Ni shim has a thermal effusivity that is about 30 times larger than the effusivities of the polymers. This leads to a contact temperature that for both polymers is less than 10 K above the mold temperature and that is about 0.8 K higher for the PMMA than for the COC. Again, this cannot explain why the replication with the PMMA is more sensitive to mold temperature, at least

not without taking into account the variation of the thermal effusivity with temperature.

#### How the Injection Velocity Influences the Replication

The injection velocity may influence the replication via several different effects. (a) Faster injection means less cooling of the polymer before reaching the mold wall. (b) Faster injection will give more shear heating. (c) Faster injection will cause a viscosity reduction due to shear thinning. (d) Faster injection will cause a higher pressure and faster pressure buildup at the wall, which will enhance the flow into the microfeatures. (e) The magnitude of the injection velocity may affect the heat transfer to the mold (the heat-transfer coefficient). (f) When switching from velocity control to pressure control, the effective switchover volume and associated pressure may increase with increasing injection velocity because of the retardation time of the injection unit. Some of these effects will be discussed below.

The pressure effect will be considered first. Faster injection will cause a higher pressure and faster pressure buildup at the wall. For a Newtonian fluid injected between two parallel plates, the pressure field behind the flow front has been solved analytically [28]. The pressure at the wall at a given distance behind the flow front is proportional to the injection velocity. The pressure also depends linearly on the distance from the flow front, except for the fountain flow region at the flow front. The net effect of this is that the pressure as a function of time is proportional to the square of the injection velocity for a Newtonian fluid. However, a polymer melt is highly shear thinning and thus not Newtonian. Shear thinning and shear heating will cause the polymer to flow more easily when injected at a high velocity, and thus partly cancel the effect the velocity has on the pressure building up at the wall.

The filling of the part in Fig. 1 without microfeatures was simulated with Moldflow [27] in the Hele-Shaw framework (planar flow). The heat-transfer coefficient at the wall was set to 5000 W/(m<sup>2</sup> K), but changing it did not influence the results presented here. Simulated pressure vs. time at the wall near the microfeatures agrees well with measurements, as shown in Fig. 9, although the pressure is overpredicted for the PMMA. These results indicate that the effect the injection velocity has on the pressure can be described well using a generalized Newtonian model for the viscosity of the polymer.

A high injection velocity will cause shear thinning and shear heating. These effects will enhance the flow into the microfeatures. The maximum temperature during the injection molding cycle, as measured with the thermocouple flush with the mold wall, was around 3 K higher when injecting the melt at 1300 mm/s than when injecting at 200 mm/s. The details of the rheology on this size scale are not completely understood, and it is suggested that viscoelastic effects can be important for the flow into microfeatures [6].

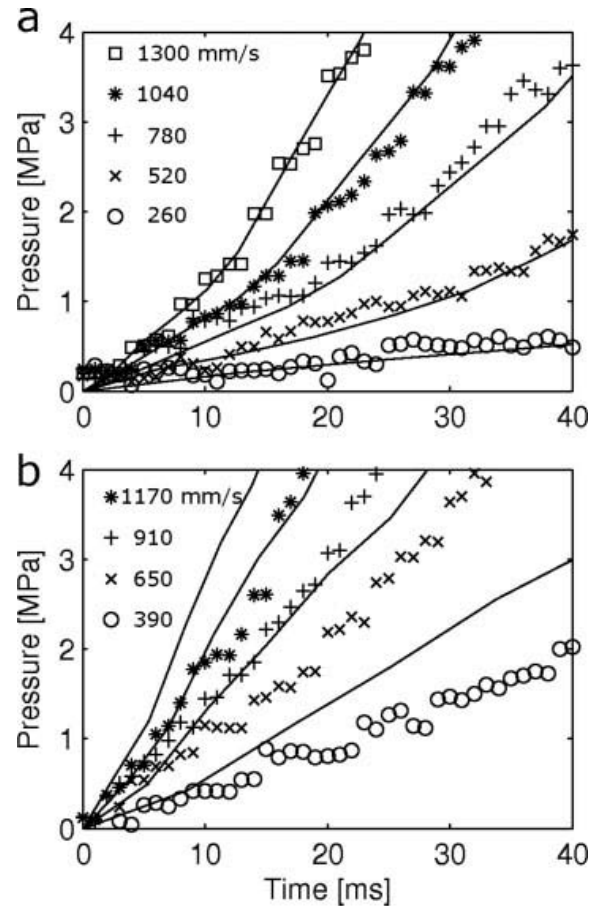


FIG. 9. Measured (symbols) and simulated (lines) cavity pressure vs. time. The location of the pressure sensor is indicated in Fig. 1. The diagrams show results for COC with mold temperature 110°C (a) and PMMA with mold temperature 70°C (b).

The injection velocity may also influence the heat-transfer coefficient. Xu et al. [12] claimed good agreement between simulated and experimental replication of microfeatures when using a heat-transfer coefficient varying via the local Nusselt number.

It could also be argued that at high velocities the polymer carries more momentum as it approaches the wall and thus has a higher capability for filling the microfeatures. However, since the Reynolds number for the polymer melt is so low (typically <1 in regular injection molding and much lower when using a characteristic length of around 1 μm), this effect will not be of any importance.

#### Empirical Relationship Between Process Parameters and Degree of Replication

As shown in Fig. 10, a good correlation exists between the degree of replication and the following expression:

$$\frac{v_{inj}^2}{\left(\frac{T_g - T_{mold}}{\Delta T}\right)^n} \quad (3)$$

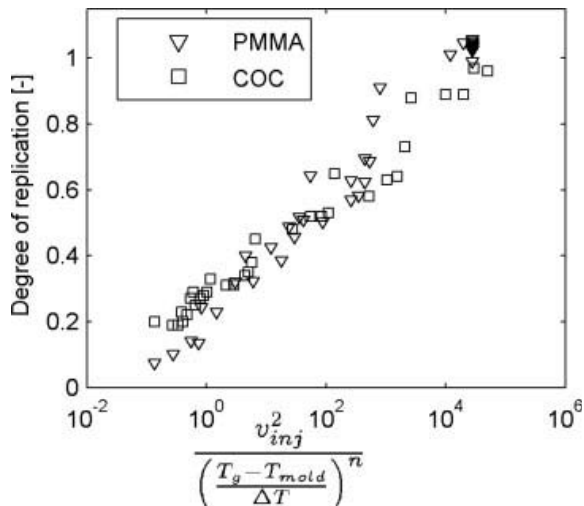


FIG. 10. The degree of replication for both materials and different molding conditions plotted as function of the empirical expression from Eq. 3. See main text for details.

Here  $v_{inj}$  (m/s) is the velocity of the flow front during injection,  $T_g$  (K) is the glass transition temperature of the polymer,  $T_{mold}$  (K) is the mold temperature,  $n$  (-) is the absolute value of the slope in Fig. 8, and  $\Delta T$  is a scaling factor which was chosen to be 60 K to make the data for the two materials overlap. Note that this is only an empirical parameter.

Eq. 3 represents the ratio between the driving force that forces the polymer into the microfeatures and the resistance to flow.

The driving force is the pressure building up in the cavity after the flow front has passed the microfeatures. It will depend on the viscosity of the melt, the geometry of the cavity, and the injection velocity. In this case, the geometry is kept fixed, and as shown in Fig. 8, the zero shear rate viscosities of the two polymers are similar at the injection temperature, meaning that even though these effects will clearly influence the replication, they will enter the expression mentioned earlier as a constant term. It was also observed in both experiments and the Mold-flow simulations that the mold temperature only had a marginal influence on the cavity pressure. The only parameter that is varied and which influences the cavity pressure is the flow front velocity. It will influence the viscosity through the shear rate and, given a constant viscosity, will cause the pressure to increase proportional to  $v_{inj}$  squared.

The resistance to flow into the microfeatures depends on the geometry of the microfeatures and the viscosity of the polymer in the microfeatures. Once again, the geometry is kept fixed and will enter as a constant term. For simplicity we have chosen to assume that the shear thinning effect in the microfeatures (easier flow) will cancel out the effect of the shear thinning in the main geometry (lower pressure).

The characteristic temperature in the microfeatures will decrease rapidly from the melt temperature down to the

mold temperature. The temperature decrease will depend on the heat-transfer coefficient, the thermal diffusivity, and the contact temperature (thermal effusivity). If we neglect the differences between the polymers regarding thermal diffusivity and effusivity, and assume that the heat-transfer coefficients will be similar for the two polymers, we can express the characteristic temperature in the microfeatures as the difference between the mold temperature and the glass transition temperature to the power of  $n$ , similar to how the zero shear rate viscosity varies with temperature as

$$\eta_0 = b(T - T_g)^n, \quad (4)$$

as seen in Fig. 8.

Even though a simple scalar expression never will be able to concentrate all information from the physically complex injection molding process, the expression given in Eq. 3 can provide useful information when predicting and optimizing the injection-molding process.

## CONCLUSION

We have described a fast and accurate method for determining the degree of replication of parts with periodic microfeatures. This method made it possible to study a large number of injection-molded parts and, from the data acquired, to present an empirical expression relating the degree of replication to the variation in injection velocity and mold temperature.

## ACKNOWLEDGMENTS

We thank Odd Løvhaugen at SINTEF ICT for providing the Ni shim.

## REFERENCES

1. R.P. Feynman, *Eng. Sci.*, **23**, 22 (1960).
2. O. Løvhaugen, I.-R. Johansen, K.A.H. Bakke, B.G. Fismen, and B.G. Nicolas, *J. Mod. Opt.*, **51**, 2203 (2004).
3. E. Puukilainen, T. Rasilainen, M. Suvanto, and T.A. Pakkanen, *Langmuir*, **23**, 7263 (2007).
4. N. Gadegaard, S. Mosler, and N.B. Larsen, *Macromol. Mater. Eng.*, **288**, 76 (2003).
5. A.K. Angelov and J.P. Coulter, in *Proceedings of SPE ANTEC*, Cincinnati, OH, 2987 (2007).
6. H. Pranov, H.K. Rasmussen, N.B. Larsen, and N. Gadegaard, *Polym. Eng. Sci.*, **46**, 160 (2006).
7. X. Han, H. Yokoi, and T. Takahashi, *Int. Polym. Process.*, **21**, 473 (2006).
8. X. Han and H. Yokoi, *Polym. Eng. Sci.*, **46**, 1590 (2006).
9. H. Yokoi, X. Han, T. Takahashi, and W.K. Kim, *Polym. Eng. Sci.*, **46**, 1140 (2006).
10. N.S. Ong, H.L. Zhang, and W.H. Woo, *Mater. Manuf. Process.*, **21**, 824 (2006).
11. Y.-C. Su, J. Shah, and L. Lin, *J. Micromech. Microeng.*, **14**, 415 (2004).

12. G. Xu, L. Yu, L.J. Lee, and K.W. Koelling, *Polym. Eng. Sci.*, **45**, 866 (2005).
13. J. Zhao, R.H. Mayes, G. Chen, P.S. Chan, and Z.J. Xiong, *Plast. Rubber Compos.*, **32**, 240 (2003).
14. R. Wimberger-Friedl, *J. Inj. Mold. Technol.*, **4**, 78 (2000).
15. M.J. Madou, *Fundamentals of Microfabrication: The Science of Miniaturization*, CRC Press, Boca Raton, FL, USA (2002).
16. M. Hecke and W.K. Schomburg, *J. Micromech. Microeng.*, **14**, 1 (2004).
17. B. Sha, S. Dimov, C. Griffiths, and M.S. Packianather, *J. Mater. Process. Technol.*, **183**, 284 (2007).
18. K. Mönkkönen, J. Hietala, P. Paakkonen, E.J. Paakkonen, T. Kaikuranta, T.T. Pakkanen, and T. Jaaskelainen, *Polym. Eng. Sci.*, **42**, 1600 (2002).
19. J. Pirskanen, J. Immonen, V. Kalima, J. Pietarinen, S. Siitonen, M. Kuitinen, K. Monkkonen, T. Pakkanen, M. Suvanto, and E.J. Paakonen, *Plast. Rubber Compos.*, **34**, 222 (2005).
20. M. Yoshii, H. Kuramoto, and Y. Ochiai, *Polym. Eng. Sci.*, **38**, 1587 (1998).
21. M. Yoshii, H. Kuramoto, T. Kawana, and K. Kato, *Polym. Eng. Sci.*, **36**, 819 (1996).
22. S. Kim, C.-S. Shiau, B.H. Kim, and D. Yao, *Polym. Plast. Technol. Eng.*, **46**, 1031 (2007).
23. D. Yao, T.E. Kimerling, and B. Kim, *Polym. Eng. Sci.*, **46**, 938 (2006).
24. C.-H. Wu and W.-S. Chen, *Sens. Actuators A*, **125**, 367 (2006).
25. M. Blochowiak, T. Pakula, H.-J. Butt, M. Bruch, and G. Floudas, *J. Chem. Phys.*, **124**, art no. 134903 (2006).
26. D. Delaunay, P. Le Bot, R. Fulchiron, J.F. Luye, and G. Regnier, *Polym. Eng. Sci.*, **40**, 1682 (2000).
27. Moldflow Plastics Insight (MPI) 6.1, *Moldflow Corporation*, Framingham, MA, USA (2007).
28. H.J. Gramberg, J.C.W. van Vroonhoven, and A.A.F. van de Ven, *Eur. J. Mech. B Fluid.*, **23**, 571 (2004).



# PAPER B

Terje Tofteberg, Maciej Skolimowski, Erik Andreassen and Oliver Geschke

## **A novel passive micromixer: lamination in a planar channel system**

*Microfluidics and Nanofluidics*, Volume 8, Issue 2, pages 209 – 215 (2010)

---

# A novel passive micromixer: lamination in a planar channel system

Terje Tofteberg · Maciej Skolimowski ·  
Erik Andreassen · Oliver Geschke

Received: 10 February 2009 / Accepted: 29 April 2009  
© Springer-Verlag 2009

**Abstract** A novel passive micromixer concept is presented. The working principle is to make a controlled 90° rotation of a flow cross-section followed by a split into several channels; the flow in each of these channels is rotated a further 90° before a recombination doubles the interfacial area between the two fluids. This process is repeated until achieving the desired degree of mixing. The rotation of the flow field is obtained by patterning the channel bed with grooves. The effect of the mixers has been studied using computational fluid mechanics and prototypes have been micromilled in poly(methyl methacrylate). Confocal microscopy has been used to study the mixing. Several micromixers working on the principle of lamination have been reported in recent years. However, they require three-dimensional channel designs which can be complicated to manufacture. The main advantage with the present design is that it is relatively easy to produce using standard microfabrication techniques while at the same time obtaining good lamination between two fluids.

**Keywords** Passive mixer · Micromixer · Split-and-recombine mixer · Confocal microscopy · Micromilling · Simulations

---

T. Tofteberg (✉) · E. Andreassen  
SINTEF Materials and Chemistry,  
PO Box 124, Blindern, 0314 Oslo, Norway  
e-mail: terje.tofteberg@sintef.no

M. Skolimowski · O. Geschke  
Institute for Micro- and Nanotechnology,  
Technical University of Denmark,  
Building 423, 2800 Kgs Lyngby, Denmark

## 1 Introduction

At high Reynolds numbers (typically >2400) two fluids can readily be mixed by turbulence. In microchannels with cross-sections less than one millimeter, this becomes difficult to achieve. For water at room temperature, turbulence in such a channel would require a velocity of several meters per second, which, in most cases, is unfeasible. Mixing of two fluids can still be easily done if the Peclet number is small enough. The Peclet number is defined as the ratio between advection time and diffusion time as  $Pe = uL/D$ , where  $u$  is the characteristic velocity,  $L$  the characteristic length and  $D$  the characteristic diffusion coefficient. When  $Pe$  is small, diffusion is fast compared to advection, meaning that mixing can usually be left to diffusion alone, e.g. as in a *T*-type mixer (Wong et al. 2004). This will be the case if the channels are either very small or the diffusion coefficient is very large. In the domain where the Reynolds number is small and the Peclet number is large, mixing becomes difficult. In microchannels this typically occurs if the channel dimensions are between 1 and 1,000  $\mu\text{m}$  for species with low diffusivity.

There are several principles already available to achieve mixing in microchannels. Nguyen and Wu (2005) presented an overview of some of the mixers available. The coarsest classification of mixers in their article is between active and passive mixers. Active mixers can, for example, utilize pressure field disturbances (Rife et al. 2000; Niu and Lee 2003) or ultrasonic devices (Yang et al. 2001) to mix fluids. If the fluids are electrolytes, time-dependent electric or magnetic fields (Bau et al. 2001; Glasgow et al. 2004) can be used. It is also demonstrated that moving magnetic beads in a changing magnetic field can efficiently mix fluids (Suzuki and Ho 2002).

In contrast to active mixers, passive mixers are stationary and do not require any external energy input apart from the pressure drop required to drive the flow. In general, this makes passive mixers simpler to fabricate and fewer external connections are needed. In the review by Nguyen and Wu, the passive mixers for microchannels are subdivided into five categories:

- (1) Chaotic advection micromixers: the channel shape is used to split, stretch, fold and break the flow. One way of achieving this is to introduce obstructions to the fluid flow in the channel (Bhagat et al. 2007; Lin et al. 2007; Hsieh and Huang 2008). Another is to introduce patterns on the channel walls that rotate the flow field, as in the staggered herringbone mixer (Stroock et al. 2002).
- (2) Droplet micromixers: droplets of the fluids are generated and as droplets move an internal flow field is generated within the droplet causing a mixing of fluids. The first such mixer was demonstrated by Hosokawa et al. (1999).
- (3) Injection micromixers: a solute flow is splitted into several streams and injected into a solvent flow (Voldman et al. 2000).
- (4) Parallel lamination micromixers: the inlet streams of both fluids are splitted into a total of  $n$  substreams before combination. For  $n = 2$ , this is the classic  $T$ -type mixer. By increasing  $n$ , the diffusion length can be decreased (Bessoth et al. 1999).
- (5) Serial lamination micromixers: the fluids are repeatedly splitted and recombined in horizontal and vertical planes to exponentially increase their interfacial area. One well-known example is the Caterpillar mixer (Schönfeld et al. 2004) but other similar designs have also been proposed (Cha et al. 2006; Xia et al. 2006).

In this report we present a lamination mixer that is similar to the serial lamination mixers. However, whereas both the parallel and the serial lamination mixers described in the literature need out of plane channels to split and rejoin the streams, our mixer has all channels in one plane. This means that the mixer can be fabricated by just bonding a planar lid on the top of a structured channel. On the other hand, a three-dimensional channel will need at least two structured parts which have to be aligned precisely in the fabrication process. Thus, the main advantage of the present mixer when compared with active mixers and other lamination mixers is the ease of fabrication. The structures can easily be mass produced using polymer replication techniques such as injection molding or hot embossing.

To the authors knowledge this is the first time a mixer working on the principle of splitting and recombining in such a simple design is presented. In order to achieve the

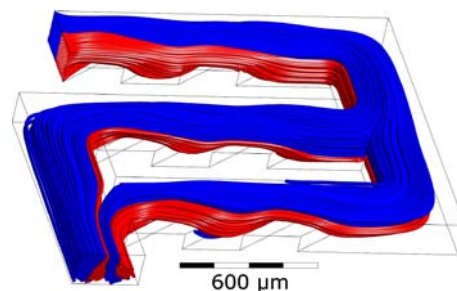


**Fig. 1** Simulated flow field in one mixing module showing lamination in the Stokes flow regime ( $Re < 5$ ). The two fluids enter in the *upper left* corner. The interfacial area between the two has approximately tripled at the exit in the *lower left* corner

folding, the flows are rotated  $90^\circ$  between each splitting and rejoining. This helical flow pattern is achieved by patterning the channel bed. An illustration of a mixing module of this kind is shown in Fig. 1. In this figure, the simulated streamlines are colored according to their origin.

The present mixer has been realized using several microfabrication techniques.

- Direct laser ablation of channels and grooves in poly(methyl methacrylate) (PMMA).
- Direct micromilling in polycarbonate (PC) and PMMA.
- Milling of the negative structure in aluminum and replication with injection molding in polystyrene (PS).
- Milling of the negative structure in PMMA and replication in polydimethylsiloxane (PDMS).

The results presented in this article relate to mixers milled directly in PMMA. We want to emphasize that the design, because of its open structure and lack of intricate details, can easily be realized using a range of microfabrication techniques.

## 2 Procedure

### 2.1 Microfabrication

As a main fabrication method micromilling (Mini-Mill/3PRO, Minitech Machinery Corp., USA) in PMMA (Röhm GmbH & Co. KG, Germany) was used. First, channels with depth of  $50\ \mu\text{m}$  and width of  $300\ \mu\text{m}$  (equal to the diameter of the tool) were milled. In the bed of the channels  $200\ \mu\text{m}$  wide grooves were fabricated using a  $\varnothing 100\ \mu\text{m}$  milling tool. This tool diameter was chosen to minimize the fillet radius on the corners of the grooves. Cut feed speed was  $70\ \text{mm/min}$  and spindle rotation was  $4,000\ \text{RPM}$ .

As an alternative fabrication method, laser ablation (48-5S Duo Lase carbon dioxide laser, SYNRAD Inc., USA) was used. The channels were obtained using a  $10\ \text{W}$  laser beam (wavelength  $10.6\ \mu\text{m}$ ) and a focusing lens with

200 mm focal length (beam diameter 290 μm). The ablation velocity was adjusted to 300 mm/min. For ablation of 200 μm grooves, an 80 mm focal length lens was used (beam diameter 90 μm) and the power was reduced to 4 W. Ablated structures had a Gaussian-like cross-section as reported earlier (Klank et al. 2002).

The microdevice was sealed with a lid using a silicone adhesive thin film (ARcare® 91005, Adhesive Research Ireland Ltd.). Thermal bonding and laser bonding methods also gave good results.

### 2.2 Confocal laser scanning microscopy measurements

To investigate the performance of the designed micromixer two dyes were used: Rhodamine B and Fluorescein. The dyes were dissolved in phosphate buffered saline (pH 7.4) with 0.2% sodium dodecyl sulfate (SDS) (all from Sigma-Aldrich, Denmark A/S). Confocal laser scanning microscopy (Zeiss LSM 510 Meta, Brock og Michelsen A/S, Denmark) was done using a 40× Fluar oil immersion objective. A 488 nm Argon laser was used for exciting Fluorescein and a 543 nm HeNe laser for Rhodamine B. The pinhole was adjusted for approximately 5 μm z axis slice thicknesses. The solutions were pumped through the microdevice by a syringe pump (model 540060, TSE Systems GmbH, Germany) with flow-rate according to the desired Reynolds number.

### 2.3 Simulations

The mixing efficiency was investigated using 3D finite volume simulations in ANSYS CFX 11.0. The procedure adopted is similar to the one described by Mendels et al. (2008) where the fluids are treated as isothermal and incompressible Newtonian fluids following the Navier–Stokes equations.

$$\nabla \cdot \mathbf{u} = 0 \tag{1}$$

$$\rho \left[ \frac{\partial \mathbf{u}}{\partial t} + \mathbf{u} \cdot \nabla \mathbf{u} \right] = -\nabla p + \eta \nabla^2 \mathbf{u} \tag{2}$$

Here  $\mathbf{u}$  is the velocity vector,  $\rho$  the density,  $\eta$  the viscosity and  $t$  the time. To track the location of the interface between the two fluids an additional concentration variable  $c$  is transported through the domain by convection and diffusion.

$$\frac{\partial c}{\partial t} + \mathbf{u} \cdot \nabla c = D \nabla^2 c \tag{3}$$

Since the mixer works by lamination, the efficiency of the mixer was best evaluated in the absence of diffusion, therefore the diffusion coefficient,  $D$ , was set to 0 in the simulations.

At the inlet, a sharp step in  $c$  is prescribed, representing two completely separated fluids. Because of numerical diffusion, it is necessary to have a fine mesh at the interface between the two phases. This interface is not initially known and in order to define a fine mesh here, an adaptive meshing procedure was used. Equations 1–3 were first solved on a relatively coarse mesh. When convergence was obtained, the mesh was refined where the variation in  $c$  over an element edge exceeded a given value. This procedure was repeated six times with an increasingly finer mesh, until convergence in mesh size. The fluid properties in the simulations are the same as water at 20°C with  $\eta = 1.002$  mPa s and  $\rho = 998$  kg/m<sup>3</sup>.

### 2.4 Validation

To validate the simulations, a channel was made using laser ablation. The channel has a cross-section of 300 μm × 50 μm, and 50 μm deep, 200 μm wide grooves inclined 55° relative to the channel axis. The shape of the grooves was measured using confocal microscopy and the measured geometry was used as a basis for simulations. The resulting rotation can be seen in Fig. 2. It can be seen that there is a good qualitative agreement between the simulated and measured rotations. Using this geometry, the closest thing to a 90° rotation occurs after three grooves. It can also be seen that after six grooves, a full 180° rotation is observed in the simulations. The experimental data indicates that this rotation is taking place already after five grooves. Note also the almost perfect match between the cross-section after the first and seventh grooves in the simulations, which is also seen after the first and sixth grooves in the experiments.

### 2.5 Design optimization

As can be seen in Fig. 2, the rotation after three grooves is not exactly a straight angle. There is also some deformation of the interface between the two tracers; it is no longer a straight line as was the case at the inlet. Three design parameters were varied in a full factorial design to see how a 90° rotation could best be achieved:

- the groove angle (45°–55°–65°),
- the depth of the grooves (50–100–200 μm),
- the depth of the channel (50–100–200 μm).

The channel width was fixed to 300 μm. The design optimization was performed using simulations in CFX of straight channels to find the configuration that gave a rotation of the flow as close to 90° as possible. The best results were obtained with a groove angle of 55°, a channel depth of 50 μm and a groove depth of 50 μm which are the parameters used in the following experiments. This optimal

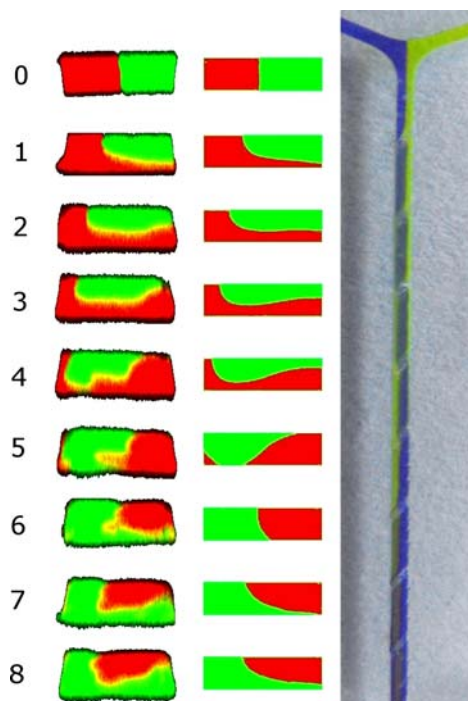


**Fig. 2** Helical rotation of the flow field in a straight channel with grooves on the channel bed in the Stokes flow regime ( $Re \sim 1$ ). *Left* confocal fluorescence microscopy measurements of the distribution of rhodamine (red, left at the inlet) and Fluorescein (green, right at the inlet). *Center* simulated flow field. *Right* photograph showing a top view of channel. The numbers indicate the cross-section after a given number of grooves, which can be seen in the *right* image

design is shown with dimensions in Fig. 3. Note that this is not a global optimum but only the optimum within the limited space sampled. Other authors have studied the optimization of helical flow patterns by patterning the channel (Yang et al. 2005, 2008) and it is likely that further optimization of the structure is possible.

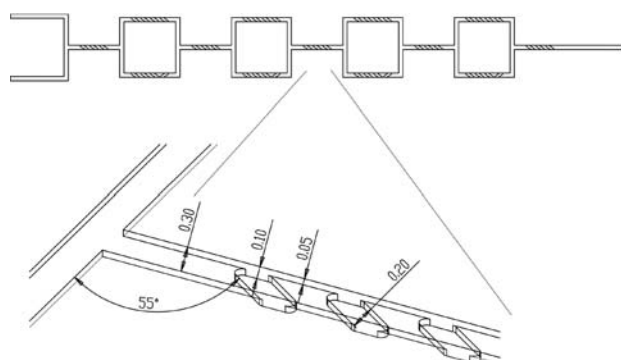


**Fig. 3** Design showing four mixing modules (*above*). Detailed view of the grooves with dimensions indicated (in mm) (*below*). The main channel is  $50 \mu\text{m} \times 300 \mu\text{m}$  with  $50 \mu\text{m}$  deep,  $200 \mu\text{m}$  wide grooves, inclined  $55^\circ$  relative to the channel axis

### 3 Results and discussion

The lamination observed experimentally and in simulations, for one module, is shown in Fig. 4. There is a good agreement between the simulated and measured rotations of the flow field. It is also demonstrated that the mixer is able to laminate the flow field as desired.

The lamination, as measured with confocal microscopy, after one to four modules is shown in Fig. 5a. Note that after three modules the two fluids are mixed well. The different laminae can still be seen, demonstrating that it is the stretching and folding effect of the device that is mixing the fluids. The mixing efficiency will in general be dependent on the Peclet number, showing better mixing at lower Peclet numbers. The diffusion coefficients for Rhodamine B and Fluorescein alone in water are  $3.6 \times 10^{-10}$  and  $4.9 \times 10^{-10} \text{ m}^2/\text{s}$ , respectively (Rani et al. 2005). Note that Rhodamine B is hydrophobic and is likely to form micelles with sodium dodecyl sulfate, increasing the diffusion coefficient. This increased diffusion coefficient was not measured. The Peclet number for Fluorescein in the setup shown in Fig. 5 is 9700. The effective Peclet number for Rhodamine B is probably larger than for Fluorescein because of the micelles. This is indicated by the fact that the evaluated degree of mixing for Rhodamine B rises slower than for Fluorescein as can be seen in Fig. 5c.

In the original staggered herringbone article by Stroock et al. (2002), the efficiency is evaluated by measuring the standard deviation  $\sigma$  in fluorescence at different locations. The distance required to achieve a reduction in standard

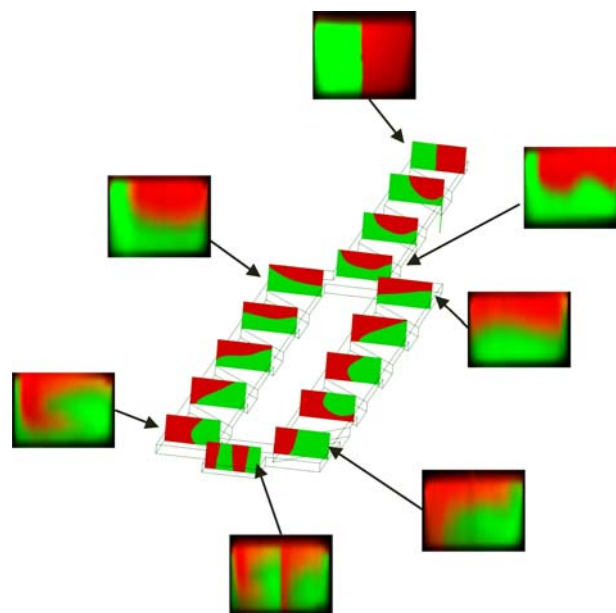
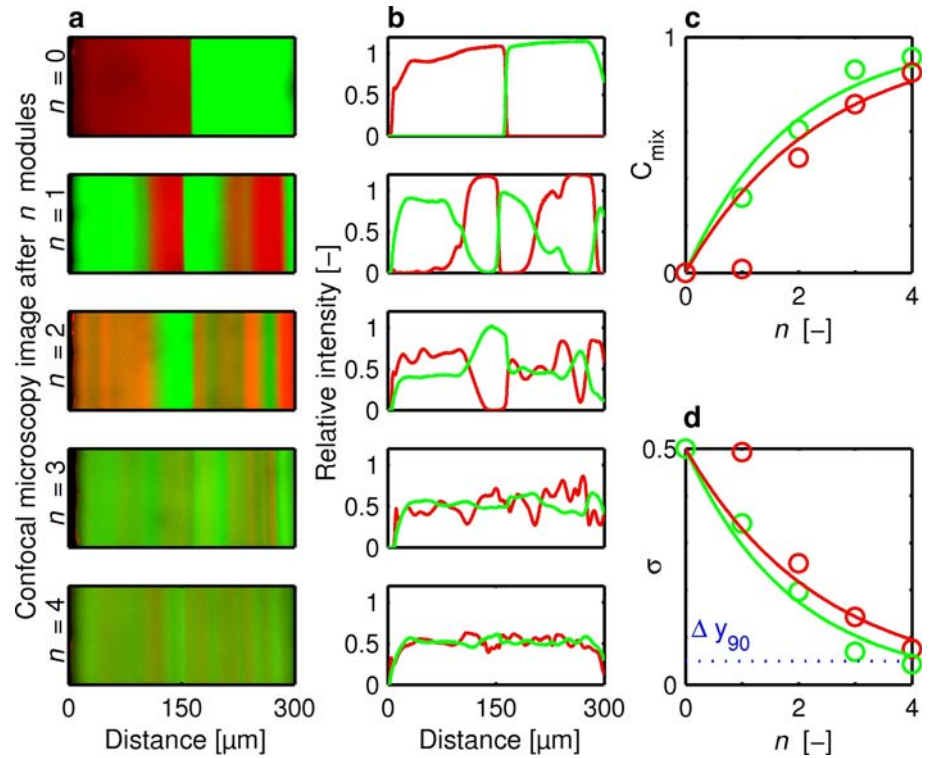


**Fig. 4** Concentration distributions within one mixing module. The images on the geometry show the simulated distribution and the outer ones are confocal microscopy measurements

**Fig. 5** **a** Confocal microscopy images showing planes at  $z = h/2$ , where  $h$  is the channel depth. The images show from the top the intensity at the entrance and after one to four full modules ( $Re = 5$ ). The modules can be seen in Fig. 3. **b** Normalized intensity of the two fluorophores measured across the cross-sections in **a**. **c** The index of mixing evaluated using the variance in the data from **b**. **d** The standard deviation of the intensities from **b** including a line showing the criteria used for mixing



deviation by 90% relative to the inlet,  $\Delta y_{90}$ , is taken as an indication of the length of mixer required. This standard deviation for the present mixer is seen in Fig. 3d after one to four full modules and it can be seen that this criterion has been met for the fluorophore with the highest diffusivity, Fluorescein, after four modules. The larger, and slower diffusing rhodamine B is close to achieving this criterion. In Stroock et al. this criterion is met after between 3.5 ( $Pe = 2000$ ) and 8.5 ( $Pe = 2 \times 10^5$ ) rotation cycles. Note that the standard deviation measure for mixing will be dependent on the resolution of the confocal microscopy used and therefore these values for mixing efficiency are not directly comparable from study to study. They are still included here for an indication of the mixing efficiency.

To quantitatively evaluate the mixing efficiency, we define the index of mixing as in (Liu et al. 2004) as

$$C_{\text{mix}} = \frac{\sigma_{\text{inlet}} - \sigma}{\sigma_{\text{inlet}}} \quad (4)$$

where  $\sigma$  is the standard deviation of the fluorescence intensity. They use simulation to evaluate the mixers and sigma is the standard deviation in the concentration of a phase variable. They find that the index of mixing for the herringbone mixer when mixing solutions of glycerol and water is approximately 0.5 ( $Pe = 1000$ ) after two full mixing cycles. The mixing index for the present mixer is shown in Fig. 5c.

### 3.1 Reynolds number dependence

The simulated lamination for two different Reynolds numbers is shown in Fig. 6. Up to a Reynolds number of 5 (flow rate 50  $\mu\text{l}/\text{min}$ ), changing the flow rate does not change the lamination process. The characteristic length, is in this case, taken as the hydraulic diameter of the channel (85  $\mu\text{m}$ ) and the characteristic velocity is the volume flow divided by the channel cross-section (300  $\mu\text{m} \times 50 \mu\text{m}$ ) where no grooves are present. It can be seen that in the Stokes flow regime, almost perfect lamination is observed. As the momentum effects become more important,

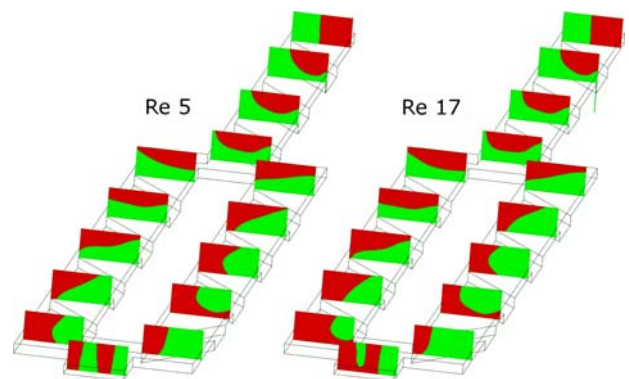


**Fig. 6** Simulated lamination as a function of the Reynolds number. For  $Re < 5$ , the profiles are independent of  $Re$  to the accuracy of this graphical representation

however, the helical rotation of the flow field changes. The structure still works as a mixer, but since the helical rotation outside the Stokes flow regime is Reynolds number dependent, it is not given that the two substreams join each other after the designed 90° rotation for Reynolds number above five. For the staggered herringbone mixers, which also rely on grooves on the channel bed to rotate the flow field, it has been reported that at high Reynolds numbers (>10) vortices form in the grooves which significantly reduce the rotation (Williams et al. 2008). Similar effects are also seen for three-dimensional mixers working on the split and recombine principle, for example, good lamination is only observed with the caterpillar mixers for low Reynolds numbers (<30, Schönfeld et al. 2004).

### 3.2 Stacking of design

In this report, the focus has not been on making the design as compact as possible. This can, however, be done when considering the layout in Fig. 1. By changing the direction of flow after each rotation of the flow field the overall shape of one mixer module is rectangular. The module shown measures  $1.5 \times 1.7$  mm and the rectangular overall shape makes it easy to pack it densely on a chip device.

## 4 Conclusions

A new concept for a passive micromixer has been developed. It is shown that the combination of patterning the channel bed and splitting and recombining the streams can be used to make controlled lamination in a 2D channel system. This is shown using both numerical simulations and experiments with prototypes. The design can easily be realized using a range of microfabrication techniques and mass produced using, for example, injection molding.

In the design optimization used in this work only a small subset of the design parameter space was investigated. A further optimization of the design with respect to mixing efficiency on an area as small as possible should be carried out in the future. It is also possible to change the mixer to divide the flow into more than two substreams. Preliminary studies indicate that splitting into three or four substreams can be used to obtain better mixing on a smaller area. Further examination of this question should be made in the future.

**Acknowledgments** The idea for the mixer presented in this work originated at the Summer School *Micro mechanical system design and manufacturing* held at the Technical University of Denmark the summer of 2008. We would like to thank the organizers, especially Arnaud De Grave and all students participating for two instructive, hectic and utmost enjoyable weeks in Lyngby. We would also like to

thank the Research Council of Norway and the Technical University of Denmark for funding.

## References

- Bau HH, Zhong J, Yi M (2001) A minute magneto hydro dynamic (MHD) mixer. *Sens Actuat B Chem* 79:207–215
- Bessoth FG, de Mello AJ, Manz A (1999) Microstructure for efficient continuous flow mixing. *Anal Commun* 36:213–215
- Bhagat AAS, Peterson ETK, Papautsky I (2007) A passive planar micromixer with obstructions for mixing at low Reynolds numbers. *J Micromech Microeng* 17:1017–1024
- Cha J, Kim J, Ryu SK, Park J, Jeong Y, Park S, Park S, Kim HC, Chun K (2006) A highly efficient 3D micromixer using soft PDMS bonding. *J Micromech Microeng* 16:1778–1782
- Glasgow I, Batton J, Aubry N (2004) Electroosmotic mixing in microchannels. *Lab Chip* 4:558–562
- Hosokawa K, Fujii T, Endo I (1999) Droplet-based nano/picoliter mixer using hydrophobic microcapillary vent. In: 12th IEEE international conference on micro electro mechanical systems (MEMS 99), pp 388–393
- Hsieh S-S, Huang Y-C (2008) Passive mixing in micro-channels with geometric variations through  $\mu$ PIV and  $\mu$ LIF measurements. *J Micromech Microeng* 18:065017
- Klank H, Kutter JP, Geschke O (2002) CO<sub>2</sub>-laser micromachining and back-end processing for rapid production of PMMA-based microfluidic systems. *Lab Chip* 2:242–246
- Lin Y-C, Chung Y-C, Wu C-Y (2007) Mixing enhancement of the passive microfluidic mixer with J-shaped baffles in the tee channel. *Biomed Microdevices* 9:215–221
- Liu YZ, Kim BJ, Sung HJ (2004) Two-fluid mixing in a microchannel. *Int J Heat Fluid Flow* 25:986–995
- Mendels DA, Graham EM, Magennis SW, Jones AC, Mendels F (2008) Quantitative comparison of thermal and solutal transport in a T-mixer by FLIM and CFD. *Microfluid Nanofluid* 5:603–617
- Nguyen NT, Wu ZG (2005) Micromixers—a review. *J Micromech Microeng* 15:R1–R16
- Niu X, Lee YK (2003) Efficient spatial-temporal chaotic mixing in microchannels. *J Micromech Microeng* 13:454–462
- Rani SA, Pitts B, Stewart PS (2005) Rapid diffusion of fluorescent tracers into *Staphylococcus epidermidis* biofilms visualized by time lapse microscopy. *Antimicrob Agents Chemother* 49:728–732
- Rife JC, Bell MI, Horwitz JS, Kabler MN, Auyeung RCY, Kim WJ (2000) Miniature valveless ultrasonic pumps and mixers. *Sens Actuat A Phys* 86:135–140
- Schönfeld F, Hessel V, Hofmann C (2004) An optimised split-and-recombine micro-mixer with uniform ‘chaotic’ mixing. *Lab Chip* 4:65–69
- Stroock AD, Dertinger SKW, Ajdari A, Mezic I, Stone HA, Whitesides GM (2002) Chaotic mixer for microchannels. *Science* 295:647–651
- Suzuki H, Ho CM (2002) A magnetic force driven chaotic micromixer. In: 15th IEEE international conference on micro electro mechanical systems (MEMS 2002), pp 40–43
- Voldman J, Gray ML, Schmidt MA (2000) An integrated liquid mixer/valve. *J Microelectromech Syst* 9:295–302
- Williams MS, Longmuir KJ, Yager P (2008) A practical guide to the staggered herringbone mixer. *Lab Chip* 8:1121–1129
- Wong SH, Ward MCL, Wharton CW (2004) Micro T-mixer as a rapid mixing micromixer. *Sens Actuat B Chem* 100:359–379
- Xia HM, Shu C, Wan SYM, Chew YT (2006) Influence of the Reynolds number on chaotic mixing in a spatially periodic

- micromixer and its characterization using dynamical system techniques. *J Micromech Microeng* 16:53–61
- Yang Z, Matsumoto S, Goto H, Matsumoto M, Maeda R (2001) Ultrasonic micromixer for microfluidic systems. *Sens Actuat A Phys* 93:266–272
- Yang JT, Huang KJ, Lin YC (2005) Geometric effects on fluid mixing in passive grooved micromixers. *Lab Chip* 5:1140–1147
- Yang JT, Fang WF, Tung KY (2008) Fluids mixing in devices with connected-groove channels. *Chem Eng Sci* 63:1871–1881

---

# PAPER C

Terje R. Tofteberg and Erik Andreassen

## **Multiscale Simulation of Injection Molding of Parts with Low Aspect Ratio Microfeatures**

*International Polymer Processing*, Volume 25, Issue 1, pages 63 – 74 (2010)

---

T. R. Tofteberg<sup>1</sup>, E. Andreassen<sup>1</sup>

<sup>1</sup>SINTEF Materials and Chemistry, Oslo, Norway

# Multiscale Simulation of Injection Molding of Parts with Low Aspect Ratio Microfeatures

*This article presents a simulation study of the injection molding of a macroscopic part with microfeatures; an optical grating with amplitude 0.6  $\mu\text{m}$  and period 3  $\mu\text{m}$ . The aim of the simulations is to develop a procedure capable of predicting the replication of optical gratings based on the injection molding processing parameters. Three coupled simulations are performed. 1.) A macroscopic simulation of the flow in the part without microfeatures. 2.) A microscale flow simulation in a domain around a single microfeature using the pressure from the macroscopic simulation as input. 3.) A thermal simulation of the mold wall coupled to the microscale simulation.*

*In the simulations the polymer melt is treated as a generalized Newtonian fluid. Shear viscosity and thermal properties were characterized as part of the study. Other physical effects such as wall adhesion and elasticity are discussed, but not included in the present model.*

*The simulation results agree well with the experimental replication data, and correctly describe how small changes in the mold temperature can lead to large changes in the replication.*

## 1. Introduction

Well-known examples of commercial polymer components with microfeatures include optical storage media and lightguide plates for LCD displays.. Microfeatured polymer components are also key elements in many emerging technologies, such as lab-on-a-chip devices and optical sensors. Surfaces patterned with a combination of micro and nano features have also been demonstrated, altering optical characteristics (Saarikoski et al., 2009) and wetting properties (Puukilainen et al., 2007).

Producing microfeatured parts requires sharp definition of e.g. channels for microfluidics and gratings for diffractive optics. The aim of the present simulation study is to capture the observations in a previous experimental study in which a part with a micrometer scaled grating was injection molded. (Tofteberg et al., 2008). The part is illustrated in Fig. 1. The essential feature of this part is an optical grating with wavelength 3  $\mu\text{m}$  and peak to valley distance 0.6  $\mu\text{m}$ . It has been

molded with different amorphous polymers. In the present work only parts molded with a cyclic olefin copolymer (COC) is considered. COC has, because of its biocompatibility and good water barrier properties (Shin et al., 2005) become popular for producing lab-on-a-chip devices and has optical properties that make it attractive in for example waveguides (Khanarian and Celanese, 2001). In the experimental study (Tofteberg et al., 2008), the injection velocity and the mold temperature were varied, while keeping all other settings constant. After production, the degree of replication of the grating was characterised and it varied greatly with processing settings. Even small changes in the mold temperature gave large changes in the replication quality.

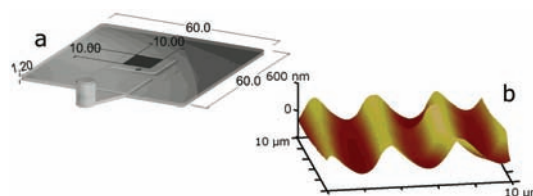


**Fig. 1 a) Drawing of the injection molded part with dimensions [mm]. The optical grating is located in the central dark square. b) Topography of the microfeatures (peak to valley distance 0.6  $\mu\text{m}$ , period 3  $\mu\text{m}$ ) measured on an injection molded part using atomic force microscopy.**

Microfeatures with low aspect ratio can be replicated well using conventional polymer processing techniques, such as injection molding and hot embossing. Consider for example the large scale production of CDs, DVDs and Blu-ray Discs which all have features in the submicrometer range. Replication of features down to 10 nm has also been reported (Gadegaard et al., 2003). However, the detailed understanding on how such features form is limited. Their formation occurs under rapid cooling as the hot polymer melt makes contact with the mold wall. The temperature difference between the two is typically more than 100  $^{\circ}\text{C}$ , and the cooling rate of the polymer in the microfeatures can exceed 10.000 K/s as will be shown.

### 1.1 Relevant physics on the microscale

When the features are small there are several effects that might influence the filling, some of which are not necessarily important on the macroscale. These effects include wall adhesion, surface tension, wall slip and size dependent viscosity. The main reason for their increased importance on the microscale is that the surface to volume ratio is larger, making surface effects relatively more important than bulk properties. Yao and Kim (Yao and Kim, 2004) described several of these effects, their relevance to injection molding and how they scale with the size of the system.

One problem with surface effects is that they are more difficult to characterize than bulk properties. Equilibrium bulk properties will in general be given if the material and the thermodynamic state are known. Surface properties on the other hand depend on at least two materials, the thermodynamic state and in some cases also the size scale at which we observe the interface. One relevant example will be given to illustrate the last point. Consider two pieces of metal at different temperatures in contact. Heat will flow from the hotter piece to the colder. At the interface between the two there will be heat flow  $q$  depending on the temperature difference  $\Delta T$  between two materials and the apparent contact area  $A_{\text{macro}}$ . The heat transfer coefficient can be defined as

$$h_{\text{macro}} = \frac{q}{\Delta T \cdot A_{\text{macro}}} \quad 1$$

If the two materials are studied under a microscope, it will become clear that the metal surfaces are rough. The contact area at this resolution  $A_{\text{micro}}$  is apparently smaller than the contact area on the macroscale. The heat flow and the temperature difference are still the same, which means that the microscopic heat transfer coefficient must be larger than the macroscopic one.

Specific microscale effects are so far not included in the simulations. The present focus is on coupling macroscale with microscale, and including the heating of the mold wall by the polymer. Nevertheless, it might be necessary to include microscale effects in future studies and their importance are estimated in the discussion section of this paper.

The high cooling rates close to the wall may influence both the rheology and the thermal properties of the melt. This is not directly a microscale phenomenon, but occurs because the microfeatures form in a very thin layer of the polymer in immediate contact with the cold mold wall. With a high cooling rate the glass transition temperature ( $T_g$ ) is shifted to higher temperatures than in measurements performed at low cooling rates, such as differential scanning calorimetry (DSC).

### 1.2 Previous simulation studies

For the part illustrated in Fig. 1 the ratio of part volume (a few  $\text{cm}^3$ ) to microfeature volume ( $\sim \mu\text{m}^3$ ) is on the order of  $10^{12}$ . To perform a filling simulation using a uniform mesh will clearly be unsuitable as the number of elements will be too large to handle. Using a mesh which is finer in the vicinity of the microfeature will also lead to problems, as the time steps needed to describe the filling of the grating must be much shorter than the ones needed to describe the filling of the main geometry.

Several authors have proposed using a coupled simulation to solve this problem. A conventional injection molding filling simulation is performed to predict the filling of the main geometry without the microfeatures. Then a subset of the data from the macroscale simulation is used as input to a local simulation on the microscale. (Eriksson and Rasmussen, 2005, Kim and Turng, 2006, Yu et al., 2004) It is assumed that the microfeatures are so small that they exert only minor influence on the flow and the temperature field in the main geometry, and there is only a one way coupling from macroscale to microscale.

Eriksson and Rasmussen performed viscoelastic, isothermal simulations of the filling of micro ribs (width  $22 \mu\text{m}$ ) using a dual domain procedure (Eriksson and Rasmussen, 2005). The whole deformation history in the macroscopic simulation was used as an initial condition and the full stress tensor was employed as a boundary condition in the microscale simulation. An experimental setup was designed to provide an isothermal flow, terminated instantly by abrupt freezing of the polymer at a controlled time. These simulations gave insight to the filling process at isothermal conditions and showed quantitative agreement with the experimental filling lengths. The simulations indicated that the state of planar stretch as the polymer makes contact with the mold wall influences the filling of microfeatures. Isothermal simulations do, however, not describe the injection molding process, in which the rapid cooling of the polymer near the wall is an essential process determining the replication of microfeatures.

Kim and Turng (Kim and Turng, 2006) performed three-dimensional finite element filling simulations of an injection molded microfeature (rectangular plate with thickness  $200 \mu\text{m}$  and length  $800 \mu\text{m}$ ) on a flat plate using a viscous model for the melt viscosity. At the inlet to the microfeature they prescribed the pressure and the temperature from a separate filling simulation of the base plate. Their findings indicated that with a high injection velocity the heat transfer coefficient in the simulations had to be increased to explain the experimental data.

Young gave an analytical approximation to the filling of microscale cylinders on a base geometry (Young, 2007). By neglecting the fountain flow effect in the filling of the main geometry and assuming a generalized Newtonian model for the rheology of the melt, an analytical expression for the cavity pressure behind the flow front was derived. This pressure and the initial melt temperature were used as boundary conditions for the microscale problem.

As described in a recent review on rapid thermal cycling of injection molds (Yao et al., 2008), controlling the mold surface temperature is the key to the replication of microfeatures. The surface temperature will not be constant during filling but increase as heat flows from the hot polymer to the mold. However, because the mold material has a much higher thermal conductivity than the polymer, the interface temperature will be closer to the initial mold temperature than the initial polymer temperature. This temperature rise is usually neglected when simulating the filling phase in conventional injection molding. The increase in mold temperature was estimated by Kim et al. (Kim et al., 2004) in a thermal simulation of an insulated mold coupled with an a simulation of the mold filling. Their simulations showed that the mold surface temperature could be kept higher for a longer time by insulating the cavity and it was argued that this would enhance the replication of microfeatures. The improved replication was also verified experimentally.

In the present article the coupled simulations on the macro and micro scales are combined with a thermal simulation of the mold temperature.

## 2. Experimental determination of material parameters

The polymer used in this study was a low viscosity cyclic olefin copolymer (COC), a copolymer of norbornene and ethylene (Topas 5013S-04 from Topas Advanced Polymers). It has a glass transition temperature  $T_g$  of 130 °C measured using differential scanning calorimetry at a cooling rate of 10 °C/s. According to the datasheet, the temperature of the injected melt is recommended to be in the range 240-300 °C, and mold temperatures up to  $T_g - 10$  °C are recommended for products requiring high surface quality (even higher mold temperatures have been used during filling in variotherm processes).

### 2.1 Rheology

Since it is important to have a good description of the temperature dependence of the viscosity from the initial melt temperature down to the glass transition, it was seen necessary to perform rheological measurements as part of the study, and not only rely on available data, which was capillary rheometry data obtained at typical melt temperatures (240-300 °C) and high shear rates.

The complex viscosity  $\eta^*$  was measured using dynamic rheometry. All measurements were performed with a Physica MCR 300 rheometer using a 25 mm diameter parallel plate fixture. Frequency sweeps were performed with angular frequency  $\omega$  in the interval 0.1 to 500  $s^{-1}$  at temperatures in the range 145-250 °C. In addition, the zero-shear viscosity  $\eta_0$  was measured at different temperatures in creep tests using the same rheometer.

The Cox-Merz rule has been shown to be valid experimentally for many rheologically simple materials

$$\eta(\dot{\gamma}) = \left| \eta^*(\omega) \right|_{\omega=\dot{\gamma}} \quad 2$$

The present COC grade is thermorheologically simple (Blochowiak et al., 2006) and we assume that the Cox-Merz relation is valid.

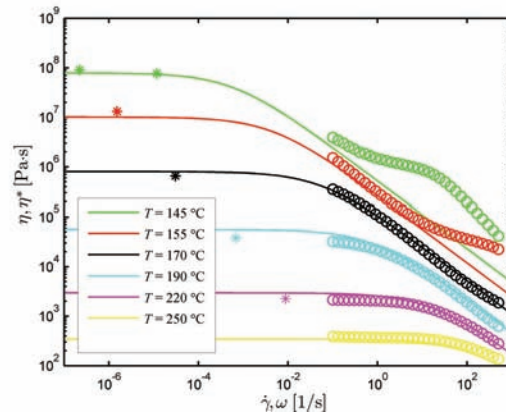


**Fig. 2 Shear viscosity as a function of shear rate and temperature. Circles: Measured complex viscosity. Asterisks: Measured zero-shear viscosity. Solid lines: Fitted Cross-WLF model.**

The Cross-WLF model was chosen to describe the rheology of the polymer melt

$$\eta(T, \dot{\gamma}) = \frac{\eta_0(T)}{1 + \left( \frac{\eta_0(T)\dot{\gamma}}{\tau} \right)^{1-n}} \quad 3$$

$$\log_{10} \frac{\eta_0(T)}{\eta_0(T_{\text{ref}})} = \frac{-C_1(T - T_{\text{ref}})}{C_2 + (T - T_{\text{ref}})}$$

The Cross-WLF parameters were fitted to the experimental data as can be seen in Fig. 2. With  $T_{\text{ref}} = 145$  °C, the coefficients are  $\eta_0(T_{\text{ref}}) = 7.96 \cdot 10^7$  Pa·s,  $C_1 = 11.3$ ,  $C_2 = 117.4$  K,  $n = 0.32$  and  $\tau = 47.6$  kPa.

The measured viscosity, spanning six decades, is well described by this model. However, it can be seen that for frequencies above  $\sim 10$   $s^{-1}$  at 155 °C, the viscosity is higher than what is expected from the Cross-WLF model. The same is the case at other temperatures; the

threshold frequency decreases with decreasing temperature. This increase in the viscosity is the glass transition and the frequency shift is an example of the time-temperature superposition principle. Finally, it can be mentioned that our viscosity measurements at high temperatures agree with data by others at typical processing temperatures (240-300 °C) for this material.

In the simulations it is clear that the Cross-WLF model does not give a good description at low temperatures. Hence, a no-flow temperature close to  $T_g$  was designated. When the flow front reaches this temperature, the flow front position is recorded and used to calculate the final degree of replication.

For many amorphous polymers, the apparent  $T_g$  will increase by approximately 3 °C per decade that the timescale of the system is changed (Ferry, 1980). In the present work, the cooling rate as the polymer passes through  $T_g$  is between 100 and 10.000 °C/s depending on the processing parameters. This is equivalent to between three and five decades faster than the DSC measurements. Hence, the expected shift in apparent  $T_g$  is in the range 9-15 °C. It will be shown in the simulations that the choice of no-flow temperature is of minor importance at the highest cooling rates. Therefore, in this study we chose a no-flow temperature of 140 °C, 10 °C above the  $T_g$  obtained by DSC.

The reason for using a generalized Newtonian model to describe the melt, despite its limitations, is because it greatly simplifies the numerical simulations compared to using a viscoelastic model. Generalized Newtonian models are available in most CFD codes and commercial software dedicated to injection molding presently only use viscous models in the filling stage. It is therefore interesting to see how far it is possible to come with such an approximation.

## 2.2 Thermal properties

The thermal diffusivity of the polymer was measured using a laser flash diffusivity apparatus (LFA 457 *MicroFlash* from NETZSCH). The specific heat was measured using a differential scanning calorimeter (DSC 204 *F1 Phoenix* from NETZSCH). When calculating the thermal conductivity a constant melt density  $\rho_{\text{COC}} = 1003 \text{ kg/m}^3$  was used. This approximation was also made in the simulations. The measured thermal properties are summarized in Fig. 3. Linear interpolation of these data was employed in the simulations. Any pressure or cooling rate dependence of the variables was neglected.

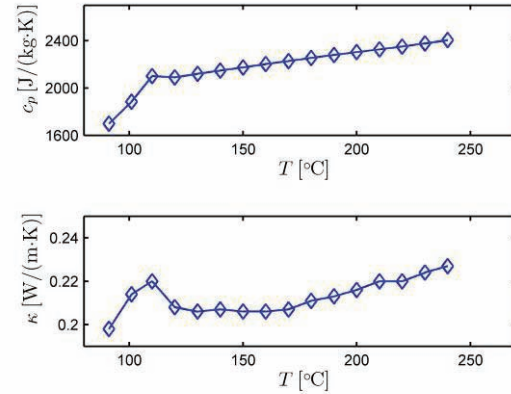


**Fig. 3 Heat capacity ( $c_p$ ) and thermal conductivity ( $\kappa$ ) for the COC polymer (symbols). In the simulations, linear interpolation of the data was used (solid lines).**

Air is trapped inside the microfeatures as the polymer enters, see Fig. 4. The air is treated explicitly in the simulations, with the following properties: Thermal conductivity  $\kappa_{\text{Air}} = 0.0261 \text{ W/mK}$ , heat capacity  $c_{p,\text{Air}} = 1004 \text{ J/kgK}$  and viscosity  $\eta_{\text{Air}} = 2 \cdot 10^{-5} \text{ Pa}\cdot\text{s}$ . Effects of pressure and temperature on these parameters are neglected. The air density  $\rho_{\text{Air}}$  is given from an ideal gas expression

$$\rho_{\text{Air}} = \frac{pM_w}{RT} \quad 4$$

where  $p$  is the pressure,  $T$  the temperature,  $R = 8.31 \text{ J/molK}$  the universal gas constant and  $M_w = 29 \text{ g/mol}$  the molecular weight. Dissolution of air in the polymer is neglected.

The thermal properties of the mold materials are given in Table 1. Temperature dependence is neglected.

**Table 1 Properties of mold and mold insert materials used in thermal simulations.**

Material	$\rho$ [kg/m <sup>3</sup> ]	$\kappa$ [W/mK]	$c_p$ [J/kgK]	Thickness [mm]
Nickel	8800	91	440	0.3
BeCu	8770	245	430	10
Steel	7800	27.5	460	23

## 3. Simulation procedure

Three coupled simulations are performed. First, the filling of the macroscopic geometry is simulated. The pressure from this simulation is then used as a boundary condition in the microscale flow simulation. The third simulation is a one-dimensional simulation of the temperature evolution in the mould wall, coupled with the microscale flow simulation.

### 3.1 Macroscale flow simulation

The macroscale simulation is performed in a commercial injection molding simulation software

(Moldflow Plastics Insight (MPI) 6.1, 2007). Since the geometry is essentially flat as seen in Fig. 1a; a 2.5D representation was used in the macroscale simulation. The injection velocity and the melt temperature are specified as input and only the filling phase of the injection molding cycle is considered. The purpose of the macroscale simulation is to obtain the cavity pressure for the microscale simulation and this is the only information passed from the macroscale to the microscale. This pressure was also measured using a pressure sensor mounted in the mould half opposite the microfeatures, and the measurements showed good agreement with the simulated pressure as was shown earlier (Tofteberg et al., 2008).

### 3.2 Microscale flow simulation

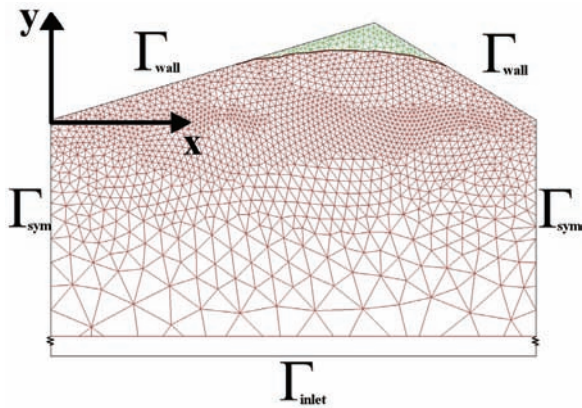


**Fig. 4** Illustration of the flow front during a microscale flow simulation. The mesh is colored red in the region where the polymer is present and green in the air region. The boundary conditions are given in the main text.

An illustration of the situation when the polymer melt hits the microstructured nickel shim (mold insert) is illustrated in Fig. 5. Behind the shim are two more metal mold components. There is no change in the microfeature geometry in the out of plane direction. Hence, 2D flow was assumed in the microscale simulation.

It can be shown analytically that when a Newtonian fluid fills the gap between two parallel plates, the flow front will take a shape very close to a semi-circle (Gramberg et al., 2004). Since the period of the optical grating ( $3 \mu\text{m}$ ) is very small compared to the thickness of the base geometry ( $1.2 \text{ mm}$ ), the flow front will be essentially flat as it makes contact with the wall. Such a flat flow front (at  $y = 0$  in Fig. 4) is used as the initial condition in the microscale simulation. The filling of the microfeatures is treated essentially as a compression molding problem, but instead of prescribing the movement of a mold/master, the cavity pressure from the macroscale simulation is used to force the polymer into the microfeatures.

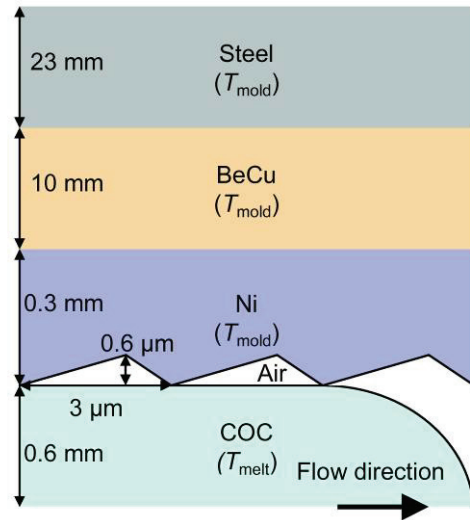


**Fig. 5** Sketch of the polymer melt hitting the microfeatures at the wall. Note that the sketch is not to scale. The temperatures indicated in parentheses are the initial temperatures in the simulations.

A general fluid dynamics (CFD) solver was used (ANSYS CFX-11.0, 2007) to solve the microscale problem. The code is based on the finite volume method and has previously been used for 3D mold filling simulations (Vahlund, 2003).

#### 3.2.1 Governing equations

The two-phase (polymer-air) flow problem is solved using what in the software is called a homogenous model. This means that the two phases share common velocity, pressure and temperature fields and the physical properties of the fluid depend on a phase variable. The equation of conservation of momentum reads

$$\frac{\partial}{\partial t}(\rho \mathbf{U}) + \nabla \cdot (\rho \mathbf{U} \otimes \mathbf{U}) = -\nabla p + \nabla \cdot (\eta [\nabla \mathbf{U} + (\nabla \mathbf{U})^T]) \quad 5$$

where  $\mathbf{U}$  is the velocity vector,  $\cdot$  is the inner product of two vectors,  $\otimes$  is the outer product and  $p$  is the pressure. The density  $\rho$  and the viscosity  $\eta$  are linear interpolations over a composition variable  $r$ .

$$\rho = r_{\text{Air}} \rho_{\text{Air}} + r_{\text{COC}} \rho_{\text{COC}} \quad 6$$

$$\eta = r_{\text{Air}} \eta_{\text{Air}} + r_{\text{COC}} \eta_{\text{COC}} \quad 7$$

The volume fractions take values between zero and one and sum to unity.

$$r_{\text{Air}} + r_{\text{COC}} = 1 \quad 8$$

Initially there is a sharp step in the volume fraction variable. During the simulation the interface region diffuses out to a width of approximately two mesh elements. This description is not meant to capture the

physics of the interface. It is a construction to treat a multiphase problem with a moving interface on a fixed grid. The equation of continuity for each phase reads

$$\frac{\partial}{\partial t}(r_\alpha \rho_\alpha) + \nabla \cdot (r_\alpha \rho_\alpha \mathbf{U}) = 0 \quad 9$$

where  $\alpha$  designates the phase, either Air or COC. The equation for conservation of energy includes heat conduction, convection and viscous dissipation;

$$\frac{\partial}{\partial t}(\rho e) + \nabla \cdot (\rho \mathbf{U} e) = \nabla \cdot (\kappa \nabla T) + \boldsymbol{\tau} : \nabla \mathbf{U} \quad 10$$

where  $e$  is the internal energy per unit mass,  $T$  is the temperature,  $\kappa$  is the thermal conductivity and  $\boldsymbol{\tau}$  is the stress tensor. Both the internal energy and the thermal conductivity are taken as linear interpolations over  $r_\alpha$ . The compression work of the gas phase is neglected in the energy equation. This work is not large and can not be implemented in the present release of the software.

### 3.2.2 Boundary conditions

At the mold wall, a no-slip condition is used for the velocity and a heat transfer coefficient  $h$  is used for the thermal boundary condition where the polymer is in contact with the wall.

$$\begin{aligned} \mathbf{U} &= 0 \\ (\kappa \nabla T) \cdot \mathbf{n}_{\text{wall}} &= -h r_{\text{COC}} (T - T_{\text{wall}}(t)) \quad \forall (x, y) \in \Gamma_{\text{wall}} \end{aligned} \quad 11$$

where  $\mathbf{n}_{\text{wall}}$  is the outward pointing wall normal vector and  $T_{\text{wall}}$  is the temperature of the mold wall. This wall temperature is coupled with a mold wall temperature simulation as described in the next section. The heat transfer coefficient was given by the expression below (discussed later)

$$h = 30.000 \text{ W/m}^2\text{K} \quad 12$$

On the microscale, only one period of the repeating grating is included in the simulation as shown in Fig. 4. To simulate the effect of a repeating grating, symmetry conditions were applied on the two boundaries labelled  $\Gamma_{\text{sym}}$  in Fig. 4. This implies zero velocity across the boundary, no shear stress tangential to the surface and zero heat flux.

$$\begin{aligned} \mathbf{U} \cdot \mathbf{n}_{\text{sym}} &= 0 \\ \boldsymbol{\tau}_{\text{sym}} &= 0 \quad \forall (x, y) \in \Gamma_{\text{sym}} \\ (\kappa \nabla T) \cdot \mathbf{n}_{\text{sym}} &= 0 \end{aligned} \quad 13$$

where  $\mathbf{n}_{\text{sym}}$  is the outward pointing normal vector and  $\boldsymbol{\tau}_{\text{sym}}$  is the shear stress at the boundary. An attempt was made to use periodic boundary conditions. The results were almost identical, as both the flow and the heat conduction through the boundary were very small, but the numerical stability was not good.

At the inlet labeled  $\Gamma_{\text{inlet}}$  in Fig. 4, the pressure  $p(t)$  is taken from the macroscopic simulation. In other models for flow into microfeatures (Kim and Turng, 2006, Young, 2007) a pressure boundary condition is applied directly at the inlet to the microfeature ( $y = 0$  in Fig. 4). This is similar to our approach, but we apply the pressure condition further away from the inlet. By doing this, the pressure loss occurring close to the entrance to the microfeature is included.

The inlet location is chosen far from the mold wall, so that the temperature here can be assumed to remain constant at  $T_{\text{melt}}$  during the simulation. The location was chosen to be 0.6 mm from the wall, i.e. at the center of the macroscale geometry.

$$\begin{aligned} p &= p(t) \\ T &= T_{\text{melt}} \quad \forall (x, y) \in \Gamma_{\text{inlet}} \end{aligned} \quad 14$$

After simulating the flow, it was verified that only a thin layer close to the wall was cooled significantly. Only regions closer to the wall than 100  $\mu\text{m}$  were cooled by more than 1  $^\circ\text{C}$  and the assumption of a constant temperature at the inlet was found acceptable.

When the macroscopic geometry is completely filled, a constant holding pressure (50 MPa) is prescribed. However, at the time the holding pressure was applied, the polymer had reached its no-flow temperature (in all the cases investigated). Hence, the holding pressure did not influence the simulated replication of the microfeatures.

### 3.2.3 Initial conditions

The microscale simulation starts when the polymer melt makes contact with the wall at the location of the microfeature. Initially there is a sharp step in  $r_{\text{COC}}$  (Eq. 15, see Fig. 4 for the coordinate system), and the entire domain has a uniform temperature equal to the initial melt temperature and zero velocity.

$$\begin{aligned} r_{\text{COC}}(t=0) &= \begin{cases} 1 & \text{for } y < 0 \\ 0 & \text{for } y > 0 \end{cases} \\ T(t=0) &= T_{\text{melt}} \\ \mathbf{U}(t=0) &= 0 \end{aligned} \quad 15$$

The reasoning for choosing  $T_{\text{melt}}$  as the initial temperature is partly that we observed that the flow front temperature in the macroscale simulation changed by less than 1 °C during filling with these processing conditions. Also, the polymer making contact with the wall has been transported outwards from the middle of the macroscopic fountain flow, and it has not been in proximity with the cold wall before making contact with the microfeature.

### 3.3 Mold wall thermal simulation

A one-dimensional heat conduction problem was solved through the mold wall:

$$\rho c_p \frac{\partial T}{\partial t} = \frac{\partial}{\partial y} \left( \kappa \frac{\partial T}{\partial y} \right) \quad 16$$

The boundary condition at  $y = 0$  is the heat flux from the microscale simulation.

$$\kappa \frac{\partial T}{\partial y} \Big|_{y=0} = \Phi(t) \quad 17$$

where the heat flux is calculated at each time step as the integral of the heat flow over the mold wall divided by the area of the microfeature projected into the plane of the wall  $L_\mu = 3 \mu\text{m}$ .

$$\Phi(t) = \frac{-1}{L_\mu} \int_{\Gamma_{\text{wall}}} h r_{\text{COC}} (T - T_{\text{wall}}) d\Gamma_{\text{wall}} \quad 18$$

The temperature at the location of the water cooling channels is assumed constant

$$T(y = 33.3 \text{ mm}) = T_{\text{mold}} \quad 19$$

and initially the temperature of the entire domain is assumed to be uniform. The time variable is the same in the microscale and the mold wall thermal simulation.

$$T(t = 0) = T_{\text{mold}} \quad 20$$

This partial differential equation was solved using the function `pdepe` in Matlab (Matlab R2007a, 2007).

### 3.4 Coupling microscale flow and thermal simulations

The microscale simulation and the mold wall thermal simulation were solved using an iterative procedure; 1.) An initial time dependent guess was made for the mold wall temperature  $T_{\text{wall}}(t)$  in Eq. 11. 2.) A full microscale simulation was carried out and the heat flux through the wall was calculated at each time step. 3.) This heat flux was integrated over the wall, projected onto the plane of the wall and used in Eq. 17 for a thermal simulation through the mould wall 4.) The temperature in the thermal simulation at  $y = 0$  was used as a new estimate for  $T_{\text{wall}}$ . Then step 2-4 was repeated until convergence. After two iterations the mold wall temperature had converged.

## 4. Results and discussion

### 4.1 Definitions

Macroscopic injection velocity ( $v_{\text{macro}}$ ): The volumetric flow rate divided by the cross-sectional area of the part.

Microscale flow front position: The contour line with volume fraction  $r_{\text{COC}} = 0.5$ .

Microscale flow front temperature ( $T_{\text{flow front}}$ ): The area-average temperature over the flow front. The temperature at the flow front is relatively uniform; the difference between the maximum and minimum is less than 1 °C.

Degree of replication (DOR): The DOR is defined as in the experimental paper, and is based on the Fourier transform of the replicated grating (Tofteberg et al., 2008). It is found by first transforming the shape of the periodic grating into the frequency domain. The DOR is then the strength of the strongest frequency (the inverse of the period) relative to the strength of that frequency measured on the shim. The mathematical definition is given in the Appendix. This expression is used for the final DOR, as well as the DOR during filling of the microfeatures. The values obtained by this method correlate well with the peak to valley distance of the molded gratings. The reason for choosing this parameter in the frequency domain is that experimentally it is faster and more robust to measure this parameter than the individual peak heights of the microfeatures.

### 4.2 Flow front advancement

Fig. 6 shows the filling of the microfeature as a function of time for different mold temperatures and injection velocities. As the melt hits the wall, it has the initial temperature of 270 °C. This means that the temperature difference in the wall temperature boundary condition (Eq. 11) is relatively insensitive to small differences in mold temperature. Hence, at a given injection velocity, the microfeature is initially filled at a rate independent of the mold temperature. After a few milliseconds the flow front has cooled enough for the flow to be sensitive to differences in mold wall temperature, and the filling curves for different mold temperatures diverge.

When comparing the results for different injection velocities in Fig. 6, the filling curves are shifted to lower  $t$  values when increasing the injection velocity. The initial advancement of the flow front is faster, the diverging behavior for different mold temperatures occur earlier and the no-flow temperatures are reached at an earlier time. These three phenomena are naturally linked to the faster buildup of pressure and the resulting reduction in thermal contact resistance.

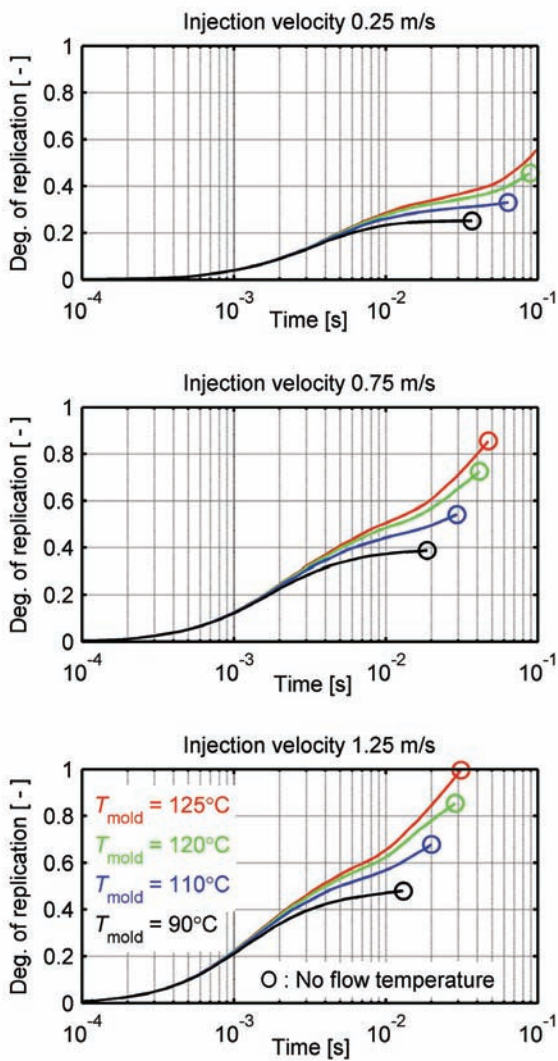


**Fig. 6** Simulated degree of replication as function of time after first polymer/mold wall contact for different mold temperatures  $T_{\text{mold}}$  and injection velocities. The circles indicate when the polymer has reached its no-flow temperature of  $140^\circ\text{C}$ . See 4.1 for definitions.

This temperature effect is clearer when plotting the degree of replication as a function of the flow front temperature as seen in Fig. 7. In this figure time runs from left to right. The flow front temperature starts at  $270^\circ\text{C}$  and as the polymer cools down it protrudes further into the microfeature until the no-flow temperature is reached. Consider the curves for a mold temperature of  $90^\circ\text{C}$ . At least for low to medium injection velocities, these curves reach a plateau before the no-flow temperature is reached. Because of the high cooling rate, an effective no-flow temperature is reached at around  $150^\circ\text{C}$ .

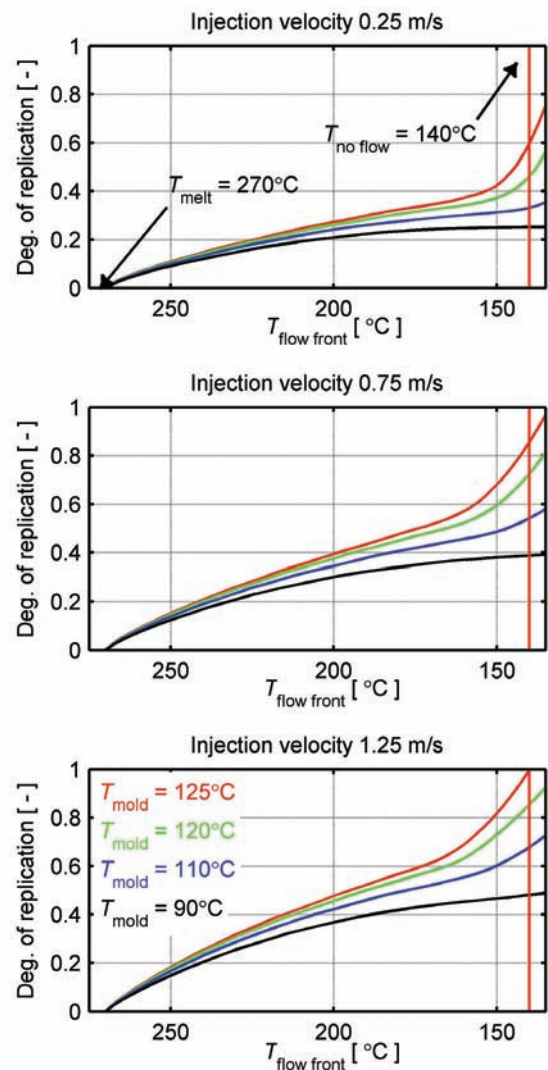


**Fig. 7** Simulated degree of replication as function of flow front temperature for different mold temperatures  $T_{\text{mold}}$  and injection velocities  $v_{\text{macro}}$ . See 4.1 for definitions. Time is increasing from left to right.

This behavior is not seen for higher mold temperatures. Most of the difference in replication between using a mold temperature of  $125^\circ\text{C}$  and  $120^\circ\text{C}$  is due to flow at temperatures between  $140^\circ\text{C}$  and  $150^\circ\text{C}$ . As shown in Fig. 2, the rheology of the melt is not well modeled at these temperatures and caution should be made when interpreting the results.

Finally, the microscale flow front temperature as a function of time is shown in Fig. 8. It can be seen that the polymer is above the no-flow temperature 50% longer when using a mold temperature of  $120^\circ\text{C}$  instead of  $110^\circ\text{C}$ , with an injection velocity of  $0.75\text{ m/s}$ . And as can be seen in Fig. 7 this leads to a significant improvement in replication.

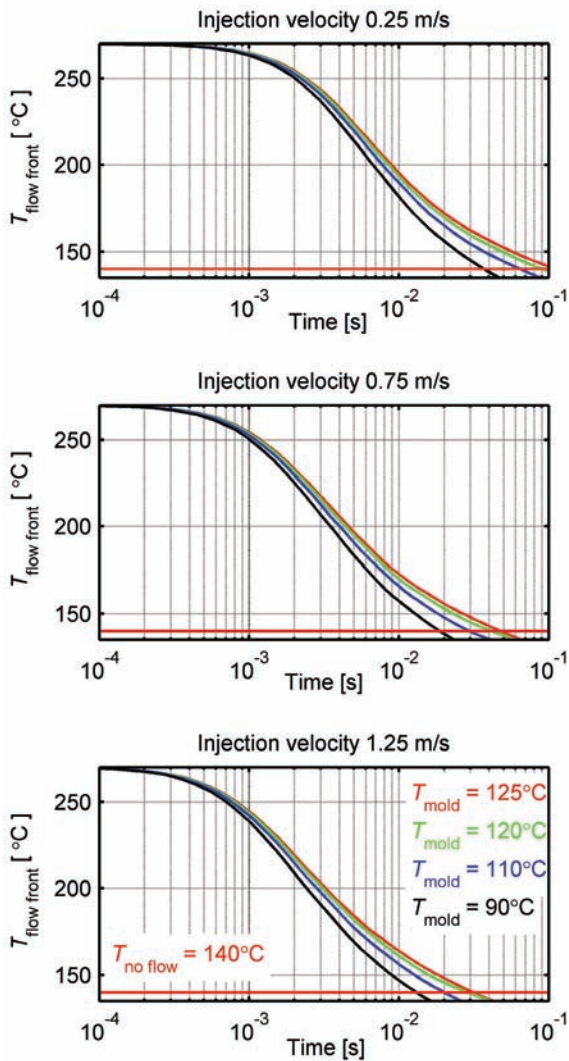


**Fig. 8** The flow front temperature as a function of time after first polymer/mold wall contact at different mold temperatures  $T_{\text{mold}}$  and injection velocities. See 4.1 for definitions.

#### 4.3 Comparison with experiments

In the experimental study, parts with microfeatures were molded using different values for the mold temperature and injection velocity while keeping the holding pressure and all other processing settings constant. The replication was assessed using white light interferometer. The experimental replication is compared to the final degree of replication from simulations in Fig. 9. The overall agreement is good. It is seen, for example that the difference in replication when reducing the mold temperature from 125 °C to 120 °C, 120 °C to 110 °C and 110 °C to 90 °C is approximately the same, even though the temperature drop is 5, 10 and 20 °C respectively. This increased sensitivity in replication with respect to mold

temperature when approaching the glass transition temperature is correctly described by the simulations.

The sensitivity to injection velocity is somewhat overpredicted in the simulations. The most noticeable disagreement is seen with the highest mold temperature (125 °C) and low injection velocities. Almost complete replication is observed experimentally, but not in the simulations. The replication being nearly independent of injection velocity at this mold temperature, as observed experimentally, indicates that the microfeatures might be filled by the holding pressure applied after the end of the filling phase. As the temperature drops below  $T_g$ , the polymer can still be elastically deformed by the holding pressure. This deformation is then frozen in as the polymer cools further. Such an effect can not be captured with a viscous rheology model.

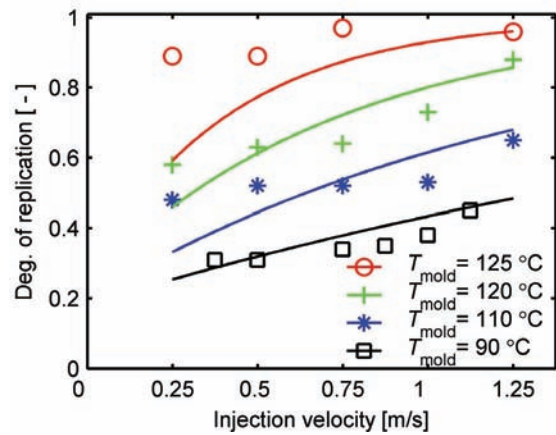


**Fig. 9** Final degree of replication from simulations (solid lines) and experiments (symbols). The experimental

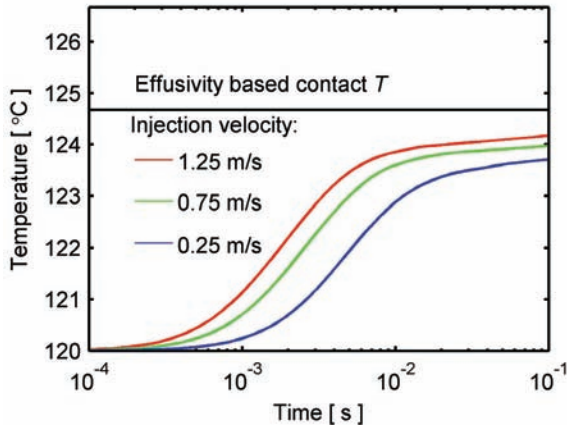
#### 4.4 Heating of the mold wall

Fig. 10 shows a typical simulation of mold surface (Nickel shim) temperature vs. time. In this example the initial mold temperature was 120 °C, but the observed temperature increase was very similar at other mold temperatures. After 0.01 s, the surface temperature has increased by almost 4 °C. This is compared to the ideal contact temperature between pure nickel and COC given by their relative effusivities  $b$ .

$$T_{\text{contact}} = \frac{b_1 T_1 + b_2 T_2}{b_1 + b_2}, \quad b_i = \sqrt{\rho_i c_{p,i} \kappa_i} \quad 21$$

This ideal contact temperature is calculated by considering two semi-infinite one-dimensional bodies initially at temperatures  $T_1$  and  $T_2$ . If the two bodies are brought into perfect thermal contact at  $t = 0$ , the contact temperature at the surface of the two bodies will be given by 21 for all positive times. (Baehr and Stephan, 2004) In the real world, no true semi-infinite bodies exist, but the simplification can be a good approximation for short times. As long as the timescale

is so short that all other thermal boundaries are not influenced by the contact boundary, a body can be considered semi-infinite. Relative effusivities have previously been used to estimate the wall surface temperature (Yoshii et al., 1998).



**Fig. 10 Simulated surface temperature of the nickel shim as a function of time for different injection velocities. The horizontal line is the ideal contact temperature between COC and nickel based on effusivity values.**

## 5. Discussion

### 5.1 The heat transfer coefficient

The simulation results are sensitive to the choice of heat transfer coefficient ( $h$ ) and the replication at all processing settings are reduced with an increasing value for  $h$ . The value in this study was chosen so that almost complete replication was achieved at a mold temperature of 125 °C and injection velocity 1.25 m/s as observed experimentally. Tuning the microscale heat transfer coefficient to match simulated data with experimental data is a procedure also used in other studies. (Kim and Turng, 2006, Yu et al., 2004). Changing the heat transfer coefficient will change the predicted replication, but the dependence on processing settings will still be similar.

When the heat transfer coefficient is chosen so that the experimental results and the simulated results agree, there is an apparent danger of camouflaging other relevant effects. If a relevant effect such as the wall adhesion is neglected, it can to a certain extent be compensated for by a change in the heat transfer coefficient

The value used in this work was relatively high compared to values used in conventional injection molding. Our rationale for this is that the apparent contact area on the microscale is smaller than on the macroscale. Another reason is that the heating of the mold was included in the present simulations. If not included, the temperature difference between mold and

polymer would have been larger in the simulation than the actual value. This could to some extent be compensated for by using a lower heat transfer coefficient.

In previous simulation studies (Kim and Turng, 2006, Yu et al., 2004), it was found that a higher heat transfer coefficient was needed to explain replication data at higher injection velocities. A velocity dependent heat transfer coefficient was not introduced in the present study as we do not have a quantitative model to describe such a relationship on the microscale. However, it should be noted that a heat transfer coefficient increasing with injection velocity (or cavity pressure) would improve the agreement between simulations and experiments, by reducing the simulated increase in replication with increasing injection velocity.

### 5.2 Wall adhesion

We have not measured the adhesion energy between the polymer (COC) and the mold wall. However, the adhesion energy between several high density polyethylenes (HDPE) and steel is on the order of  $\gamma = 0.03 \text{ J/m}^2$  (Anastasiadis and Hatzikiriakos, 1998). Chemically, COC and HDPE are similar polymers, consisting only of carbon atoms saturated with hydrogen. The adhesion energy between COC and nickel is therefore believed to be of the same order of magnitude.

The work  $W_{\text{pressure}}$  required to fill a microfeature at constant pressure  $p$  is

$$W_{\text{pressure}} = p \cdot V_{\text{micro}} \quad 22$$

where  $V_{\text{micro}}$  is the volume of the microfeature. The work required to fill the microfeature by wall adhesion alone is

$$W_{\text{adhesion}} = \gamma \cdot A_{\text{contact}} \quad 23$$

where  $A_{\text{contact}}$  is the contact area between the wall and the polymer. If Eq. 22 and 23 are assumed to be equal, a capillary pressure representing the same driving force as the wall adhesion can be calculated. Using  $\gamma = 0.03 \text{ J/m}^2$  and the present geometry, gives a capillary pressure of 0.1 MPa. This could be a significant contribution to the filling, the first milliseconds, especially for low injection velocities, when the cavity pressure increases slowly.

The effect of surface tension can also be evaluated by considering the dimensionless capillary number  $Ca$ . It is defined as the ratio between viscous forces and surface tension.

$$Ca = \frac{\hat{U} \hat{\eta}}{\hat{\sigma}} \quad 24$$

where  $\hat{U}$  is a characteristic velocity,  $\hat{\eta}$  a characteristic viscosity and  $\hat{\sigma}$  a characteristic surface tension. We

define the area average value over the flow front as the characteristic velocity and viscosity. The surface tension for different solid COC materials has been measured to be in the range 0.035-0.045 N/m (Shin et al., 2005). In the present simulations  $Ca < 1$  for  $t \leq 1$  millisecond. This indicates a flow where capillary action is important. The capillary number then increases rapidly and after around 10 milliseconds  $Ca > 100$  and surface tension can be neglected.

### 5.3 Viscous dissipation

The relative importance of viscous dissipation to wall heat transfer can be evaluated using the Brinkman number

$$Br = \frac{\hat{U}^2 \hat{\eta}}{\kappa \Delta T} \quad 25$$

where  $\Delta T$  is the temperature difference between the mold wall and the polymer. For all parameters the characteristic values used are the area average over the flow front. During the present microscale simulations, the Brinkman number is always below  $10^{-3}$  and viscous dissipation in the microfeature can be disregarded.

### 5.4 Conduction and convection

The relative importance of heat conduction and heat convection can be evaluated using the Peclet number

$$Pe = \frac{\hat{U} \hat{h} \rho c_p}{\kappa} \quad 26$$

The characteristic length  $\hat{h}$  is taken as the height of the microfeature (0.6  $\mu\text{m}$ ) and all other properties are evaluated at the flow front as area averages. As the velocities in the present simulations are small, the Fourier number is initially below  $10^{-2}$  and decreases with time. This means that heat transported with the polymer by convection is much smaller than the amount of heat conducted through the polymer.

### 5.5 Inertial forces

In conventional injection molding simulations it is common to assume Stokes flow conditions. This means that advective inertial forces are neglected because they are dominated by viscous forces. The ratio between inertial effects to viscous forces can be characterized by the Reynolds number

$$Re = \frac{\rho \hat{U} \hat{L}}{\hat{\eta}} \quad 27$$

On the microscale, both the characteristic length and characteristic velocity are smaller than on the macroscale. At the start of the simulations the Reynolds number is below  $10^{-6}$  and, as the viscosity rapidly increases, the Reynolds number is further reduced. Hence, the assumption of Stokes flow is still valid on the microscale.

### 5.6 Wall slip

For polyolefins it has been observed that the critical shear stress required for cohesive failure and onset of wall slip scales linearly with the adhesion energy. For the interface between HDPE and steel the critical value is 0.1 - 0.18 MPa. (Anastasiadis and Hatzikiriakos, 1998) The maximum shear stress in the present simulations exceeds this, with wall shear stresses up to 1 MPa during the filling phase. It is therefore likely that flow instabilities can occur. However, even if the polymer would slip at the wall, there will still be zero velocity at the sharp lower corners of the grating (where the mold wall tangents  $y = 0$  in Fig. 4) and it is unlikely that wall slip will have a large influence on the replication.

### 5.7 Elastic effects due to fountain flow

In injection molding there is a fountain flow region close to the flow front. In this region, melt will be transported from the midplane of the flow field and out towards the wall. In this fountain flow, the polymer will be stretched and sheared causing high molecular orientation and a state of tension close to the mold wall.

In the paper by Eriksson et al, it is argued that elastic effects in the flow front region influence the filling of microfeatures. They define a Deborah number  $De$  as the ratio of storage modulus  $G'$  to loss modulus  $G''$  at a frequency equal to the macroscopic flow front velocity  $v_{\text{macro}}$  divided by the half thickness of the geometry  $H$ .

$$De = \frac{G'(v_{\text{macro}} / H)}{G''(v_{\text{macro}} / H)} \quad 28$$

For Deborah numbers above 0.1, they observe improved replication at isothermal conditions. In the present simulations, the Deborah number as defined by Eq. 28 is between 0.5 and 1.2. The moduli are then evaluated at 270 °C using data from the dynamic rheology measurements. The  $De$  values indicate that elastic effects might influence the filling also in our case.

In order to reduce  $De$  to below 0.1, it would be necessary to either reduce the injection velocity to 0.01 m/s while keeping the melt temperature at 270 °C or keep the injection velocity at 0.25 m/s and increase the melt temperature to 410 °C.

### 5.8 Heating of the mold wall

As seen in Fig. 10, the temperature of the mold surface increases significantly as the polymer comes in contact with it. The effusivity based contact temperature is a reasonable estimate for the mold wall temperature at times when good thermal contact between the two materials has been established. The estimate is better for high injection velocities since a better thermal contact between the melt and the wall is established earlier.

However, within the timescale of the microfeature filling, the contact temperature is lower than that based

on an effusivity approach, due to the finite heat transfer coefficient. At longer times ( $> 0.5$  s) the BeCu block under the nickel shim is heated and its higher thermal diffusivity reduces the contact temperature from what would be expected from a effusivity based argument.

Nevertheless, an effusivity based contact temperature is in better agreement with the simulated results in this study than using a constant mold temperature. It can therefore be recommended as a first guess for the mold temperature increase.

The relatively small increase in the surface temperature of the mold is usually neglected in commercial injection molding simulation software. But, as can be seen in Fig. 9, a  $5^\circ\text{C}$  increase in the mold temperature has a significant effect on the replication, both in the simulations and experimentally, and this effect has to be included for a realistic melt temperature evolution.

### 5.9 Rheology close to the glass transition

As seen in Fig. 2, the rheology close to the glass transition is not well described by a Cross-WLF model. Also, as the temperature decreases the elastic contribution to the rheological response will increase. This effect is not included in our simulations, and it is common to neglect this effect in conventional injection molding simulations. We see, however, in Fig. 7 that a significant part of the deformation of the polymer into the microfeature occurs at temperatures close to the glass transition. A more realistic description of how microfeatures are replicated in injection molding may need a viscoelastic model. However, viscoelastic simulations require special computational codes and more detailed polymer characterization. Furthermore, many viscoelastic simulations have mainly been demonstrated for isothermal flow.

## 6. Conclusions

Simulations predicting how the replication of microfeatures changes with injection molding processing settings have been demonstrated.

The size of the microfeatures is in a transition region where several physical effects which normally are disregarded in injection molding start becoming important. One such effect is the wall adhesion, which can have a larger effect on the filling of microfeatures than the cavity pressure the first millisecond after polymer wall contact. It is also observed that the microfeatures partly fill at temperatures close to the glass transition. At such low temperatures, the assumption of viscous flow gradually becomes worse. Nevertheless, simplified viscous simulations are able to capture how changes in the processing settings influence the replication.

The high sensitivity of replication to changes in mold temperature is predicted by the simulations. To be able

to realistically capture this temperature sensitivity, it was necessary to include the heating of the mold wall explicitly in the simulations.

## Appendix

To reconstruct the degree of replication as defined in the experimental paper (Tofteberg et al., 2008), the following procedure was used;

1. Find the shape of a single period  $y(x)$  of the grating from  $0$  to  $x = L_\mu = 3 \mu\text{m}$ . This shape follows the mold wall where there is contact between polymer and wall and the contourline  $r_{\text{COC}} = 0.5$  elsewhere.

$$y(x) = h(x) \quad \forall x \in [0, L_\mu] \quad 29$$

2. Shift this period along the  $x$ -axis and repeat the shape 15 times. The value 15 was chosen to match the region investigated in the experimental study.

$$y(x) = y(x - L_\mu) \quad \forall x \in [L_\mu, 15L_\mu] \quad 30$$

3. Calculate the power spectrum density (PSD) of this grating. This was done numerically using the implementation of the fast fourier transform in Matlab (Matlab R2007a, 2007).

$$\Phi(\omega) = \left| \frac{1}{\sqrt{2\pi}} \int_0^{15L_\mu} y(x) e^{-i\omega x} dx \right|^2 \quad 31$$

4. Integrate the main peak of the PSD and divide by the integral of the PSD peak of the mold to obtain the degree of replication DOR. The half width of the integration  $\Delta\omega$  is chosen so that both the local minima on each side of the peak are included in the integration.

$$\text{DOR} = \frac{\int_{1/L_\mu - \Delta\omega}^{1/L_\mu + \Delta\omega} \Phi(\omega) d\omega}{\int_{1/L_\mu - \Delta\omega}^{1/L_\mu + \Delta\omega} \Phi_{\text{mold}}(\omega) d\omega} \quad 32$$

## References

- Anastasiadis, S. H. and Hatzikiriakos, S. G., "The work of adhesion of polymer/wall interfaces and its association with the onset of wall slip", *J. Rheol.*, **42**, 795-812 (1998)
- ANSYS CFX-11.0 from ANSYS Europe Ltd. (2007)
- Baehr, H. D. and Stephan, K.: *Wärme- und Stoffübertragung*, 4th ed., Springer, Heidelberg (2004)
- Blochowiak, M., et al., "Thermodynamics and rheology of cycloolefin copolymers", *J. Chem. Phys.*, **124**, art no 134903 (2006)
- Eriksson, T. and Rasmussen, H. K., "The effects of polymer melt rheology on the replication of surface microstructures in isothermal moulding", *J. Non-Newtonian Fluid Mech.*, **127**, 191-200 (2005)

- Ferry, J. D.: Viscoelastic properties of polymers, 3rd ed., John Wiley & Sons, Inc., New York (1980)
- Gadegaard, N., et al., "Biomimetic polymer nanostructures by injection molding", *Macromol. Mater. Eng.*, **288**, 76-83 (2003)
- Gramberg, H. J., et al., "Flow patterns behind the free flow front for a Newtonian fluid injected between two infinite parallel plates", *Eur. J. Mech. B-Fluid.*, **23**, 571-585 (2004)
- Khanarian, G. and Celanese, H., "Optical properties of cyclic olefin copolymers", *Opt. Eng.*, **40**, 1024-1029 (2001)
- Kim, S. W. and Turng, L. S., "Three-dimensional numerical simulation of injection molding filling of optical lens and multiscale geometry using finite element method", *Polym. Eng. Sci.*, **46**, 1263-1274 (2006)
- Kim, Y., et al., "Modelling of passive heating for replication of sub-micron patterns in optical disk substrates", *J. Phys. D: Appl. Phys.*, **37**, 1319-1326 (2004)
- Matlab R2007a from The MathWorks (2007)
- Moldflow Plastics Insight (MPI) 6.1 from Moldflow Corporation (2007)
- Puukilainen, E., et al., "Superhydrophobic polyolefin surfaces: Controlled micro- and nanostructures", *Langmuir*, **23**, 7263-7268 (2007)
- Shin, J. Y., et al., "Chemical structure and physical properties of cyclic olefin copolymers - (IUPAC technical report)", *Pure Appl. Chem.*, **77**, 801-814 (2005)
- Saarikoski, I., et al., "Modification of polycarbonate surface properties by nano-, micro-, and hierarchical micro-nanostructuring", *Appl. Surf. Sci.*, **255**, 9000-9005 (2009)
- Tofteberg, T., et al., "Injection molding of a diffractive optical element", *Polym. Eng. Sci.*, **48**, 2134-2142 (2008)
- Vahlund, C. F., "Using a finite volume approach to simulate the mould filling in compression moulding", *J. Reinf. Plast. Compos.*, **22**, 499-515 (2003)
- Yao, D., et al., "Rapid thermal cycling of injection molds: An overview on technical approaches and applications", *Adv. Polym. Technol.*, **27**, 233-255 (2008)
- Yao, D. G. and Kim, B., "Scaling issues in miniaturization of injection molded parts", *J. Manuf. Sci. E-T. ASME*, **126**, 733-739 (2004)
- Yoshii, M., et al., "Experimental study of the transcription of minute width grooves by injection molding (II)", *Polym. Eng. Sci.*, **38**, 1587-1593 (1998)
- Young, W. B., "Analysis of filling distance in cylindrical microfeatures for microinjection molding", *Appl. Math. Model.*, **31**, 1798-1806 (2007)
- Yu, L., et al., "Flow and heat transfer simulation of injection molding with microstructures", *Polym. Eng. Sci.*, **44**, 1866-1876 (2004)

---

# PAPER D

Michal M. Mielnik, Ib-Rune Johansen, Terje R. Tofteberg, Britta G. Fismen, Erik Andreassen, Dag Ausen, Lutz Riegger, Peter Koltay, Roland Zengerle, Anja Gulliksen, Lars A. Solli, Frank Karlsen, Petter Grønn, Rainer Gransee, Tobias Baier, Thomas Hansen-Hagge, Helen Keegan, Cara Martin, John O'Leary and Liv Furuberg

## **A microfluidic platform for fluorescence-based multi-target biochemical assays**

Submitted for possible journal publication 2009

---

# A microfluidic platform for fluorescence-based multi-target biochemical assays

Michal M. Mielnik,<sup>\*a</sup> Ib-Rune Johansen,<sup>a</sup> Terje R. Tofteberg,<sup>b</sup> Britta G. Fismen,<sup>a</sup> Erik Andreassen,<sup>b</sup> Dag Aussen,<sup>a</sup> Lutz Riegger,<sup>c,d</sup> Peter Koltay,<sup>c,d</sup> Roland Zengerle,<sup>c</sup> Anja Gulliksen,<sup>e</sup> Lars A. Solli,<sup>e</sup> Frank Karlsen,<sup>e</sup> Petter Grønn,<sup>e</sup> Rainer Gransee,<sup>f</sup> Tobias Baier,<sup>f,h</sup> Thomas Hansen-Hagge,<sup>f</sup> Helen Keegan,<sup>g</sup> Cara Martin,<sup>g</sup> John O'Leary<sup>g</sup> and Liv Furuberg<sup>a</sup>

A Lab-on-a-chip system capable of fully automated sample aliquoting and parallelisation, sequential fluidic control and highly sensitive real-time fluorescence detection is presented. The system, consisting of a disposable polymer microfluidic chip and a control instrument, is evaluated in terms of reliability and performance. The presented chip is designed to perform nucleic acid analysis using the isothermal method Nucleic Acid Sequence Based Amplification (NASBA) in eight parallel channels. However, the chip design may be readily adapted to other isothermal nucleic acid amplification technologies. A novel fluidic actuation method permits robust, simultaneous on-chip flow control of the parallel samples using a single chip-to-world interface. The method is easily scalable and increased parallelisation can be achieved without the need to modify the instrument hardware. The real-time fluorescence detection unit is based on an optical probe scanner with fiber optical coupling to stationary illumination and detection optics. The sensitivity of the unit is demonstrated during on-chip NASBA amplification of eight parallel 740nl samples. By integration of dried reagents on-board the chip, the automated system may be applied to perform a variety of multi-target, sequential biochemical assays.

## Introduction

As the field of microfluidics and Lab-on-a-chip (LOC) technology has rapidly progressed over the past years, a variety of biochemical assays such as protein detection, enzyme analysis, immunoanalysis and gene detection have been demonstrated successfully on the microscale.<sup>1</sup> Simultaneously, a variety of approaches to microfluidic handling and control have been developed and investigated. Capillarity driven systems, continuous flow/pressure driven systems, centrifugal microfluidics, droplet based (digital) systems and electrokinetics are now all fairly established microfluidic platforms, each featuring distinct strengths and weaknesses depending on the specific application.<sup>2</sup> Together, the microfluidic technology development and the microscale implementation of biochemical assays are expected to pave the way towards more integrated, automated, reliable and inexpensive (disposable) diagnostic systems. Ultimately, the sought-after target application of Lab-on-a-chip based devices in a point-of-care setting may be within reach.<sup>3</sup>

On-chip genetic analysis by means of nucleic acid amplification, in particular by means of polymerase chain reaction (PCR),<sup>4</sup> has achieved much attention in the microfluidic community. A vast amount of work has been reported in the literature, and several review articles are available on the subject.<sup>5,6,7</sup> As pointed out by Chen *et al.*,<sup>7</sup> full system integration remains a challenge, in particular the inclusion of sample preparation in an amplification and

detection device. Indeed, despite extensive efforts and considerable progress in demonstration of individual assay sub-functions on-chip, no truly integrated, automated sample in – answer out system exists thus far. Although recent attempts to provide user-friendly, autonomous analysis systems are highly promising, they still require substantial user intervention during operation, in addition to external supply of reagents.<sup>8,9,10</sup>

Development of an automated platform for chip-based pre-concentration, nucleic acid (mRNA) extraction, amplification, and fluorescent detection, without the need of any user intervention during the procedure, has been the major goal of the EU funded project MicroActive.<sup>11</sup> With such a platform, a procedure currently carried out in selected clinical laboratories by highly trained personnel, would require minimal training and could be readily accomplished in a doctor's office, or even at the patient's bed-side in a point-of-care setting. Two modular prototypes, one for sample preparation and one for amplification and detection have been developed and tested individually, with a common interface to facilitate later integration into one single setup. The automated sample preparation module is presented elsewhere.<sup>12</sup> Here, we focus on the technical aspects of the amplification and detection module, which comprises a novel general platform for biochemical assays. The biochemical performance of the system using dried enzymes stored on-chip has been demonstrated previously.<sup>13</sup> The biochemical

performance of the complete, integrated system with all reagents stored on-chip and sample in – answer out capability will be presented in a separate publication.

5 We present a microfluidic platform capable of automated sample aliquoting, parallelisation, sequential fluidic control and real-time detection. The system may be applied to perform automated, multi-target, sequential biochemical assays. The platform consists of a microfluidic chip and an  
10 external control- and detection instrument. A novel optical system design permits highly sensitive fluorescence detection, making the system particularly suited for detection assays based on molecular beacons<sup>14</sup> with nanoliter detection volumes. A simple sample loading, splitting and metering  
15 solution based on capillary forces, combined with a new, highly efficient pressure-pulse based microfluidic actuation method provide excellent control of discrete, parallel sample droplets using a single chip-to-world interface. The chip is based entirely on passive components, and can be realized in a  
20 single step by injection molding using commercially available processes. The presented system is specifically designed to comply with the necessary fluidic operations required for an on-chip nucleic acid sequence based amplification (NASBA).<sup>15</sup> Using the same fluidic principles and control  
25 instrument, however, the chip design can be readily adapted to other isothermal nucleic acid amplification technologies such as SMART, SDA, RCA, LAMP, HDA or SPIA, all of which exhibit capabilities which make them competitive with the popular non-isothermal PCR, and offer great potential for the  
30 development of hand-held nucleic acid diagnostic devices.<sup>16</sup>

## The NASBA protocol

Prior to the technical description of the fluidic control system, the optical detection system and the instrument, some insight into the NASBA protocol is desirable. Therefore, the NASBA  
35 technique will be briefly reviewed in the following.

NASBA is a transcription-based method which can amplify any RNA and single-stranded DNA sequence isothermally at 41°C, by the simultaneous use of the activities of the three  
40 enzymes; avian myeloblastosis virus reverse transcriptase (AMV-RT), ribonuclease H (RNase H) and T7 RNA polymerase.<sup>15</sup> When employing fluorescent molecular beacons in NASBA, rapid, specific and sensitive real-time RNA amplification is accomplished.<sup>17,18</sup> The NASBA technology  
45 was chosen for the current work because it is well documented for analysis of clinical specimens.<sup>19, 20, 21</sup>

NASBA contains two main reagent stock solutions; the nucleotide ion-adjusted master mixture (hereafter termed  
50 mastermix) and the enzymes. In order to achieve on-chip amplification, the following steps are required: First, the sample, consisting of purified nucleic acids, must be precisely metered. The accuracy of this metering is important as the concentrations are critical for the final reaction mixture.  
55 Second, the sample needs to be mixed with mastermix, primers, and probes, and heated to 65°C for 2 minutes, a

necessary initial heat denaturation step. Third, the sample is cooled to 41°C and mixed with the enzymes. At this stage, the amplification reaction commences and the sample mixture  
60 is kept at constant temperature of 41°C throughout the rest of the assay. Real-time fluorescence detection is initiated immediately after mixing with enzymes, and the shape of the recorded temporal development of the fluorescence signal determines whether the reaction is positive or not, i.e. whether  
65 the targeted nucleotide sequence identifying e.g. a specific virus is present in the sample. To perform an analysis targeting a different gene sequence, only the primers and probes need to be changed, whereas the rest of the reagents remain unaltered (although some concentration optimization  
70 may be required). Multiplex analysis is possible by simultaneously introducing several different primers into the assay, each identified by a different fluorescent probe. In such case, fluorescent detection over several wavelengths identifying the various primer types needs to be performed,  
75 however, this is not without some loss of sensitivity due to cross-talk between the fluorophores. Alternatively, the sample can be divided into several sub-samples, each of which can then be analyzed (singleplex) in parallel chambers for the presence of different targets without the risk of cross-  
80 contamination.

In terms of requirements for the microfluidics, the chip design, and the instrument for a NASBA assay, the protocol description given above yields the following implications.  
85 Implementing the assay on chip requires two chambers for storage of reagents. Also, precise temperature control is necessary, as well as a highly sensitive optical detection system. To permit simultaneous detection of several markers, sample splitting as well as accurate metering is also required.  
90 Finally, a method for fluidic control of several samples in parallel is needed, as well as scanning capability for the optical detection system.

In the present work, detection of the human papillomavirus  
95 (HPV), a cervical cancer marker, was chosen as a model case to demonstrate the capabilities of the optical detection system. All reagents required to perform the HPV detection employing NASBA were supplied by the PreTect HPV-Proofer kit (NorChip AS, Norway). The sample preparation protocol and  
100 the NASBA assay with pre-mixed reagents has been demonstrated on-chip previously and is described in detail in [22, 23].

## Microfluidic chip

105 A schematic illustration of the microfluidic chip is shown in Fig. 1. The chip consists of a sample inlet, a supply channel (cross-section of  $400 \times 200 \mu\text{m}^2$ ,  $W \times D$ ), eight parallel reaction channels, and a waste chamber containing a highly absorbing filter paper. Each of the parallel reaction channels consists of  
110 three parts; a metering channel ( $400 \mu\text{m} \times 120 \mu\text{m}$ , volume of 740nl) and two mixing/reaction chambers (volume approx.

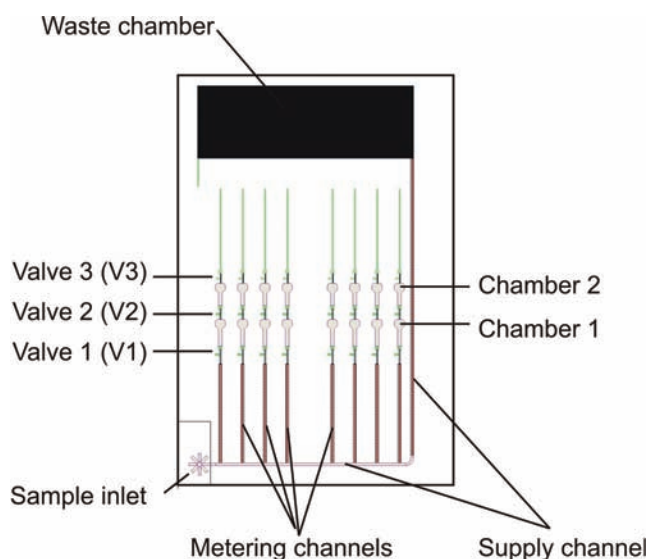


Fig. 1. Schematic illustration of the microfluidic chip. The chip consists of a sample inlet, a supply channel, a waste chamber, and eight parallel reaction channels, each consisting of a metering section and two reaction chambers separated by three capillary valves.

800nl). In the present context of NASBA being the targeted assay, the first chamber will contain dried master mix, primers and probes, while the second chamber will contain dried enzymes and additionally serve as the reaction/detection chamber. The two chambers and the metering channel are separated by hydrophobically coated capillary valves of increasing strength; the valve dimensions for the three valves V1, V2 and V3 are  $200 \times 80 \mu\text{m}^2$ ,  $125 \times 80 \mu\text{m}^2$ , and  $50 \times 50 \mu\text{m}^2$ , respectively. The overall chip size is  $75 \times 44 \times 1.5 \text{mm}^3$  (L×W×D).

### Fabrication

The microfluidic chips were manufactured by injection molding using a Battenfeld EM 50/120 machine with maximum clamping force of 500kN and screw diameter of 25mm. The material was a cyclic olefin copolymer (Topas 5013S-04 from Topas Advanced Polymers) chosen due to excellent optical properties, low water permeability, ability to replicate microfeatures,<sup>24</sup> and biochemical compatibility.

The mold insert (see Fig. 2A) was fabricated in brass by z-microsystems (Austria) using a combination of micromilling and electrical discharge machining (EDM). EDM was used in order to ensure proper definition of feature corners with a filet radius of less than  $50 \mu\text{m}$ , which was necessary in order to realize capillary valves of acceptable quality.

The mold temperature was  $115^\circ\text{C}$  (approximately  $15^\circ\text{C}$  below the glass transition temperature of the polymer material) and the nominal injection velocity was set to  $40 \text{cm}^3/\text{s}$ . The cycle time was 45s. A thick sprue in the inlet system required a long cooling time; with a mould and inlet system dedicated for industrial production the cycle time could be substantially reduced.

After manufacturing, the chip quality was assessed by white light interferometry (WYKO NT-2000, Veeco Instruments). The surface roughness of the microfluidic channels was measured to be below 100nm. The main contribution to the roughness was the milling pattern in the mold insert.

After molding, the chips were subjected to a cleaning and surface modification procedure (see next section). Finally, the chips were manually sealed with a polyolefin sealing foil containing microencapsulated glue on the contact side (HJ Bioanalytik GmbH). Prior to sealing, a piece of highly absorbant filter paper was cut and inserted into the waste chamber.

### Surface modification

Prior to surface modification, the chips were cleaned by sonification in a DI-water bath, treated with a 3% hydrogen peroxide solution to remove RNases with a subsequent rinsing step in RNase-free water and dried with pressurized nitrogen. The RNase removal step is important in order to avoid contamination of the chips which could inhibit the NASBA amplification reaction.

After cleaning, the microfluidic channel system was rendered hydrophilic by coating it with PEG (P2263, Sigma-Aldrich). This was done both to achieve the desired capillary flow properties, and to avoid unwanted adsorption of enzymes to the channel walls. PEG was chosen based on an initial evaluation of biocompatibility. First, the chip surface was activated by oxygen plasma treatment (2min, 200W). Then, the PEG was applied by dispensing  $30 \mu\text{L}$  of a  $4.8 \text{mg/mL}$  PEG-methanol solution into the channel inlet. The solution was spontaneously pulled into the channel system by capillary forces, thus priming all required surfaces. The chip was then left to dry in lab atmosphere for 2 minutes prior to further processing.

Selective hydrophobic patterning of the capillary valves was achieved by spotting a solution of 0.5 wt% Teflon (Teflon AF 1600, Du Pont) and 0.25 wt% carbon black (type 901, Degussa) solved in a perfluorinated solvent (Fluorinert FC-77, 3M) using a nL-dispenser (PipeJet<sup>TM</sup> P9, BioFluidiX), see Fig. 2Bi. Due to the small size of the valves, a standard pipette could not be used due to the high risk of overflow. The coating was applied by dispensing six to twelve 10 nl droplets, depending on the valve. A close-up of the hydrophobically patterned valves of a single reaction channel is shown in Fig. 2Bii. The teflon-carbon black solution forms a superhydrophobic surface, see Fig. 2Biii. The contact angle of DI-water on teflon-carbon black was found to be  $157.9^\circ \pm 2.1^\circ$ . Taking into account the contact angle and the dimensions of the capillary valves, the pressure required to break the valves (i.e. the burst pressure) can be estimated.<sup>25</sup> In the present case, the burst pressure of valve V1, V2 and V3 are approximately 23mbar, 27mbar and 53mbar, respectively, with DI water as working liquid. These values are expected to

be somewhat lower in the case of a sample mixed with NASBA reagents due to an anticipated reduction of the surface tension.<sup>26</sup>

5 An image of the finalized chip with filter paper, spotted hydrophobic valves and lamination foil is shown in Fig. 2C.

### The instrument

In order to facilitate automated operation of the microfluidic chip, an instrument providing the necessary means for fluid actuation, heating, and sensing has been developed, see Fig. 3A. The instrument comprises two major units; a system for fluidic actuation and control, and an optical detection unit. These are described in the following sections.

### Fluidic control system

15 All on-chip flow control is performed *via* a single chip-to-world pressure interface. After the chip is inserted into the instrument, a spring-loaded clamping system is actuated by turning a release knob, thus lowering a connector block onto the chip (see

20 Fig. 3B). The connector block contains a single groove which covers all the parallel channel outlets of the chip, and connects to a single pressure interface. The chip and fluidic control system are designed such that the sample liquid is at no time in contact with the instrument; all on-chip fluidic control is achieved by pressurized air *via* the fluidic interface. In this way, the risk of cross-contamination between samples is minimized.

Flow actuation is achieved by generation of negative-amplitude pressure pulses delivered to the downstream end of the reaction channels *via* the connector block. This novel actuation method will be further discussed in the next section.

35 The pressure pulse generation system consists of a 500ml pressure reservoir, three SMLD-5b valves from TechElan, a pressure sensor for system feedback and a custom made syringe pump integrated into the instrument for pressure level adjustment. The default state of the valves is in closed position. A schematic drawing of the pressure pulse system layout is shown in

40 Fig. 3C). During operation, the syringe pump and the feedback pressure sensor are used to set the desired pressure level in the reservoir. Once the correct pressure is reached, valve A is opened and a pressure pulse is issued into the chip. After a prescribed time  $\Delta t$ , valve B is opened venting the system to atmospheric conditions, thus terminating the pressure pulse. At the same time, valve A is closed. A third valve (valve C in Fig. 3C) is included in the system in order to allow resetting the reservoir pressure and/or syringe position during operation without communicating with the microfluidic chip. The valves are integrated into the connector block ( Fig. 3B).

55 Sample heating and temperature control is achieved by a Peltier element and a thermistor (feedback) located beneath the chip surface ( Fig. 3B). The accuracy of the heating system has been determined to be better than 0.1°C.

60

30

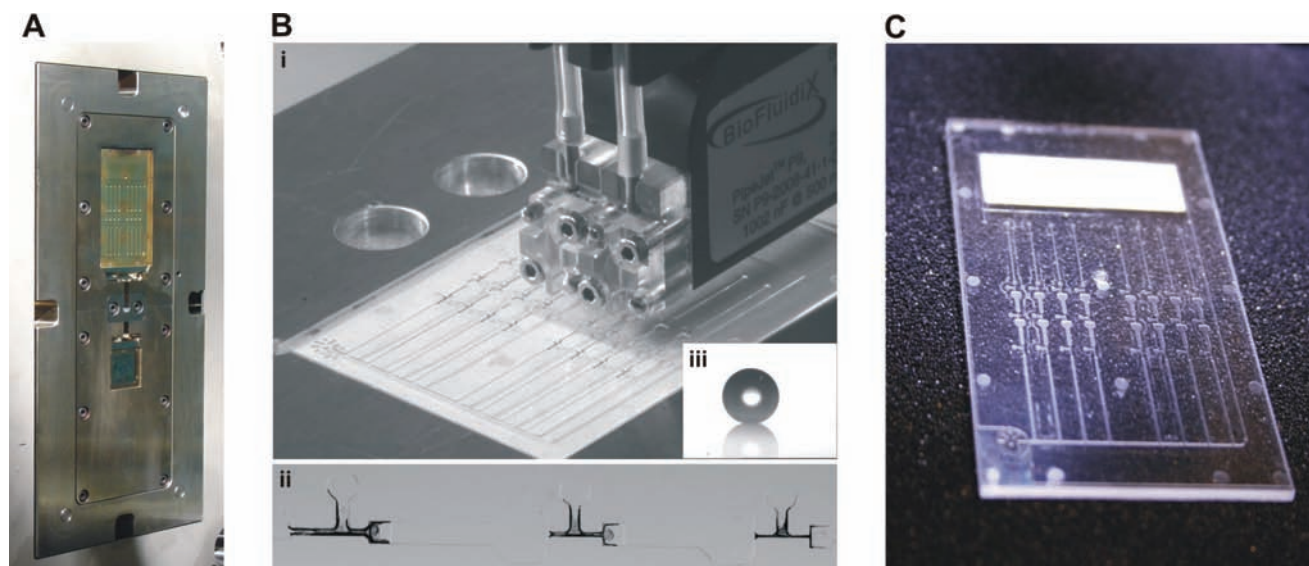


Fig. 2: A: Mold insert for chip fabrication; B: i) PipeJet™ P9 dispenser during spotting of hydrophobic valves of the chip. The chip is visible in the holder beneath the spotter. ii) Close-up of hydrophobically coated valves of a single reaction channel. iii) DI-water droplet on superhydrophobic Teflon – carbon black coated surface. The contact angle is 159°; C: Injection molded COC microfluidic chip containing surface modification, filter paper and sealing.

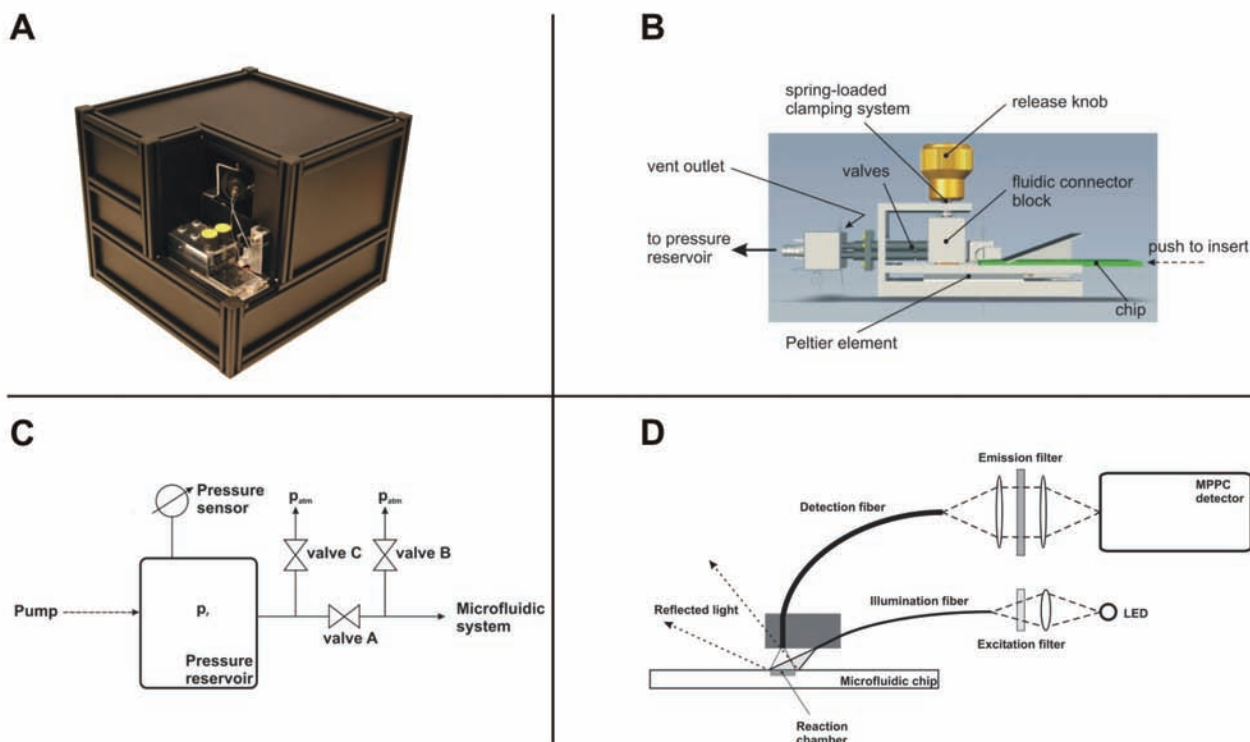


Fig. 3: **A:** Image of the control instrument; **B:** Chip loading system and fluidic chip-to-world interface. The chip is loaded into the instrument by sliding it onto an aluminum holder. Relieving a turn knob forces the spring-loaded fluidic connector block onto the chip, creating a tight seal. Valves for generation of flow actuation pressure pulses are integrated in the connector block. The Peltier element resides within the aluminium holder underneath the chip; **C:** Schematics of the pressure pulse generation system. A syringe pump is used to set the desired pressure level of the pressure reservoir with feedback provided by a pressure sensor. Two valves are used for pulse generation; one to initiate the pulse (valve A – opens pressure communication between reservoir and chip) and one to terminate the pulse (valve B – vents the system to atmospheric pressure). In addition, a third valve (valve C) is incorporated in the system to reset the pressure level of the reservoir without communication with the microfluidic chip if necessary; **D:** Schematic illustration of the optical detection system. A LED is used for illumination of the sample. The emitted light is guided via an excitation filter and lens into an optical fiber and projected onto the reaction chamber. The emitted fluorescent signal is collected via an optical fiber, filtered through an emission filter and detected by an MPPC detector. The illumination fiber is positioned at an angle with respect to the chip surface. The angle, numerical aperture and the fiber tip position of the illumination and detection fibers is optimized to suppress specular reflected light from the surface. The use of flexible fibers greatly simplifies scanning across the eight parallel chambers of the microfluidic chip.

### 15 Optical detection system

In order to detect the reactions in eight parallel chambers of the chip, the optical detection system consists of a fluorescence excitation/detection module and a scanner.

20 The scanning function is realized mechanically by introducing an optical probe connected *via* flexible fibers to the illumination and detection source of the optical system. The probe is attached to a linear actuator (NEMA 17 linear actuator stepper motor from Ultra Motion, spatial resolution  
25  $< 5\mu\text{m}$ ) and scanned across the chip, halting above each reaction chamber to perform the necessary fluorescence measurements. In this way, neither the chip nor the optical components have to be moved. This has several substantial advantages; First, avoiding chip translation eliminates the risk  
30 of unwanted fluid displacement on-chip due to vibrations during movement. Second, avoiding movement of the

typically fragile optical detector eliminates the risk of premature failure. Third, an optical probe and fiber setup greatly simplifies the mechanical system required for scanning, and thus reduces complexity, cost, and system size. A schematic illustration of the optical detection system is shown in Fig. 3D.

40 The illumination fiber is a  $600\mu\text{m}$  core diameter multimode fiber with numerical aperture (NA) of 0.22 (Thorlabs). The detection fiber is a  $1000\mu\text{m}$  core diameter multimode fiber with NA of 0.48 (Edmund Optics). The high NA of the detection fiber is chosen in order to achieve a high light  
45 gathering efficiency. The lower NA of the illumination fiber is chosen to match the distance between the fiber and the chip to illuminate only one chamber at a time, to avoid crosstalk from nearby chambers, and to reduce the background signal from

fluorescence and scattering.

In order to avoid background noise, the illumination fiber was tilted with respect to the chip surface, see

Fig. 3D. Compared to an epi-illumination setup, there are two distinct advantages with the current solution; first, there is no need for coupling optics on the illuminator/detector side, and second, reflection of excitation light into the detection pathway is avoided, thus greatly reducing the background noise level of the system. The former simplifies the necessary hardware and thus reduces system price. The latter is especially important in the case of highly sensitive detectors. The energy of a single photon at 500nm wavelength is:  $E = hf = hc/\lambda = 3.96 \times 10^{-19}$  J. Illuminating with 10 mW for 1 second thus corresponds to an energy of 10mJ or  $2.5 \times 10^{16}$  photons. The reflection from a plane surface of COC polymer is approx. 4%, which yields  $1 \times 10^{15}$  photons. The typical leakage between an excitation and emission filter is around  $10^{-7}$ . Counted in photons, the leakage would be around  $1 \times 10^8$  photons. As a good Photo Multiplier Tube (PMT) can detect single photons, avoiding reflections in low-level signal detection is consequently of great importance.

A 1W blue LED from Luxeon is used for excitation, and a band pass filter (Semrock filter FF01-472-30) is used to suppress unwanted wavelengths. During operation, the LED is modulated with a 310Hz square pulse train with 50 % duty cycle. The signal is demodulated by a digital lock-in amplifier, and integrated for 1 second. The lock-in amplifier removes the influence caused by external illumination, and makes the instrument more practical in use. The amount of light emitted from the fiber end is close to 10 mW. The use of a LED source is advantageous since modulation can easily be obtained, but also since it emits light in a limited spectral region. At the detector side, two lenses (Edmund Optics) were used to limit the angular cone through the emission filter (Semrock filter FF01-534-42), and thereby avoid the typical blue shift generated in interference filters by uncollimated light. A Multi-Pixel Photon Counter (MPPC C10507-11-050U from Hamamatsu) was chosen to serve as detector of the fluorescent signal after initial sensitivity tests.

In addition to the above described components, the instrument contains custom made electronics. The control of all instrument functions is performed via an in-house made software developed in LabVIEW (National Instruments).

## System functionality and performance

In order to perform a sample analysis, only three manual operations are required. Firstly, the microfluidic chip must be loaded into the instrument. This is done simply by sliding the chip into an aluminum holder and thereafter releasing a spring-loaded fluidic interface block onto the chip surface. The latter ensures air-tight connection between the chip and the instrument, thus permitting control of the on-chip fluidic operations *via* the instrument's pressure-based control system. Secondly, the sample (volume of approx. 20 $\mu$ l) has to be transferred onto the chip inlet. Thirdly, the assay has to be started by pressing an on-screen button on a computer. After

completing these simple procedures, the rest of the assay is completely automated, without the need of any further user intervention.

## Microfluidic performance

### Sample loading, splitting, and metering

Due to the star-shaped inlet of the microfluidic chip and the hydrophilic coating of the channel walls, a liquid sample pipetted onto the chip inlet is spontaneously drawn into the supply channel by capillary forces. While the sample liquid fills the supply channel towards the waste chamber, the parallel metering channels are sequentially filled up to the position of the first capillary valve, see Fig. 4A-B. When the sample reaches the waste chamber, it comes into contact with the filter paper which starts to absorb the liquid and hence acts as a capillary pump. Because the capillary forces exerted by the wicking action of the filter are considerably higher than those present in the comparatively large supply channel, the supply channel is effectively drained (Fig. 4C-D). As the rear meniscus of the sample liquid travels downstream the supply channel, it sequentially passes the metering channels and is pinched off, leaving a precisely metered liquid aliquot inside each of the metering channels. When the process is complete, isolated liquid plugs, or subsamples, reside in each reaction channel, while all surplus sample is contained inside the waste chamber (Fig. 4D).

The capillary sample loading, metering and waste discharge functions were tested on twelve chips. A sample containing purified mRNA was used as working liquid. Sample loading was evaluated in terms of the number of parallel channels per chip successfully filled with sample. Out of the total of 96 reaction channels (12 chips with 8 channels per chip), 95 were successfully filled, corresponding to a yield of 99%. Most likely, the unsuccessful filling of one reaction channel was due to clogging by e.g. dust particles during chip handling prior to lamination, possibly during hydrophobic spotting.

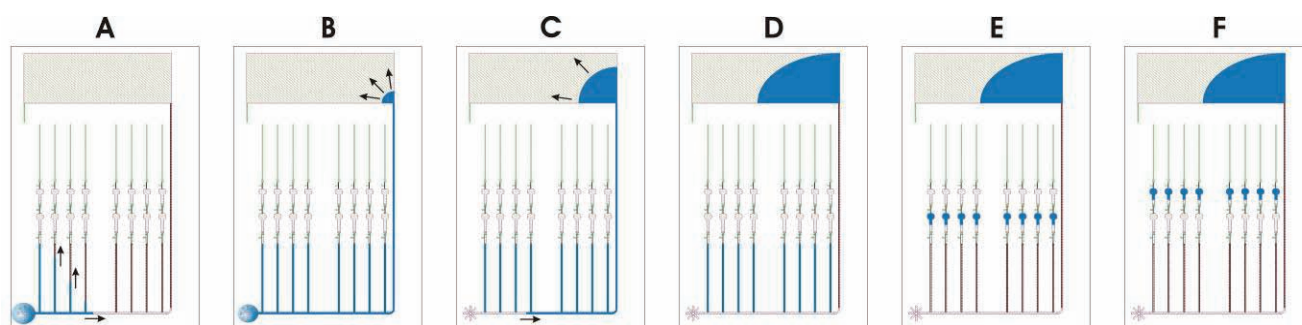
Visual observations of the metering channels during operation indicate that the variation in the filling degree of the channels is less than 5% of the metering volume. This number is based on assessment of the length of the liquid plug residing within the metering channel as compared to the metering channel's total length. Based on previous experiments on on-chip NASBA with dried reagent storage,<sup>13</sup> this metering accuracy should be sufficient for successful amplification.

In all cases, the discharge of surplus sample into the waste chamber functioned in a satisfactory manner.

### Pressure pulse actuation

Once the loading, metering and waste discharge steps are completed, the sample plugs have to be transferred to the first reaction chamber and heated to 65°C. After a prescribed time, they are moved to the second chamber, where they are incubated at 41°C for the remaining duration of the assay. Reliable and controlled sample actuation through the parallel

reaction channels (i.e. from the metering channel to the first



5 Fig. 4: Chip functionality. **A → B:** A sample pipetted onto the chip inlet is drawn into the system by capillary forces, sequentially filling all parallel reaction channels up to the first capillary valve (metering section). **C → D:** The filter paper inside the waste chamber functions as a capillary pump and drains the system. While the rear meniscus of the liquid is drawn through the supply channel, the liquid inside the metering sections is pinched off, leaving a precisely metered aliquot in each of the eight reaction channels. All surplus sample is collected in the waste chamber. **E:** The pressure pulse system is actuated, transferring the sample plugs in parallel to the first reaction chamber. **F:** The pressure pulse system is actuated again, transferring the sample  
10 plugs in parallel to the second reaction chamber.

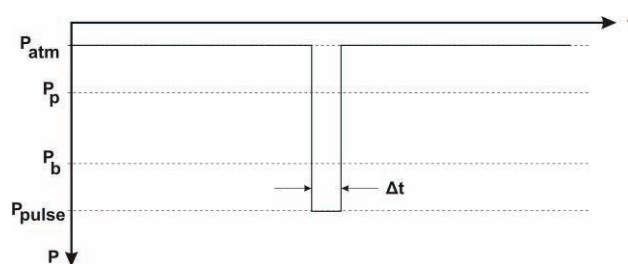
chamber, and from the first chamber to the second chamber) is consequently of great importance with respect to correct  
15 functionality of the chip, i.e. successful performance of the parallelized biochemical assay.

In our case, the sample is carried by a compressible medium (i.e. air). We have previously attempted to control the  
20 sample droplets by continuous pumping thus invoking sequential passing of the parallel capillary valves.<sup>26</sup> This method proved excessively sensitive to inherent geometrical variations (fabrication reproducibility) as well as variations in the hydrophobic spotting of the capillary valves, in addition to  
25 uncertainties with respect to the timing of the liquid plug movement. In order to avoid these issues, we introduce the novel concept of pressure pulse actuation.

Briefly, the pressure pulse actuation method is based on  
30 issuing short, high amplitude pressure pulses to control the individual sample plugs in all parallel channels simultaneously. The (absolute) amplitude of the applied pressure pulse is higher than the expected pinning pressure  $p_p$  of the microchannel walls as well as the burst pressure  $p_b$  of  
35 the capillary valve, see Fig. 5. The time duration of the pressure pulse  $\Delta t$  is sufficiently long to move the sample through the capillary valve, yet it is short enough so that the liquid stops prior to reaching the next valve. Once the capillary valve is opened with a high-amplitude pulse, the rest  
40 of the movement of the sample liquid (towards the inlet of the next capillary valve) can be achieved by a second pressure pulse of longer duration and amplitude well below the burst pressure of the next valve.

45 In contrast to a continuous pumping approach, where the system is subjected to a slowly changing pressure level which in turn makes the exact time of system response to the

imposed actuation unpredictable, the pressure pulse method



50 Fig. 5 The principle of pressure pulse actuation. A pressure pulse with an (absolute) amplitude higher than the pinning pressure of the channel system and the burst pressure of the capillary valve is used to actuate the liquid for a short period of time to overcome the required pressure  
55 barriers.

provides excellent timing control. The time delay  $t_d$  between the issuing of the actuation impulse and its impact on the liquid sample is proportional to the total fluidic channel  
60 length  $L$  and inversely proportional to the speed of sound  $c$ , i.e.  $t_d \sim L/c$ , which, in the practical situation, translates to immediate system response. This permits accurate and robust control of on-chip sample movement, and makes the method ideally suited as a universal platform for highly efficient  
65 parallel actuation without the need to alter the actuation hardware.

In addition to the purely fluidic aspects of pressure pulse actuation, the method requires only a simple external control  
70 system which is straight forward to implement, and it is therefore well suited for achieving compact instrumentation.

#### Parallel sample movement

The implemented sample actuation scheme during instrument

operation is shown schematically in Fig. 6. First, a pressure pulse of duration  $\Delta t_1=300\text{ms}$  and amplitude of  $-3000\text{Pa}$  ( $-30\text{mbar}$ ) was issued to pull the samples in parallel through the first capillary valve (V1). This pressure pulse was sufficiently long to pull the front meniscus of the samples through the first valve, but not long enough to completely fill the first reaction chamber (CH1). This is to make sure that the second valve will not break during the first actuation pulse. After the first pulse, the pressure reservoir of the instrument was pressurized to  $-15\text{mbar}$  during the time  $\Delta t_2$ , which is in the range of 5 – 10 seconds. When the correct pressure level was reached, a second pulse (with amplitude of  $-15\text{mbar}$ ) is issued with a duration of  $\Delta t_3 = 10\text{s}$ . This pulse, termed the pull-in pulse, pulls the samples completely into CH1, so that the front meniscus reaches the inlet of the second capillary valve (V2). Note that the amplitude of this pulse is well below the design strength of V2 which was approximately  $-25\text{mbar}$ .

When the samples have resided in CH1 for the required time, the pulse sequence is repeated and the samples are moved in parallel into the second mixing/reaction chamber (CH2). All pressure levels of the sample actuation scheme (actuation pulse and pull-in pulse strength), as well as pulse duration times ( $\Delta t_1$  and  $\Delta t_3$ ) are adjustable via the instrument's control software. The time delay between the actuation and the pull-in pulses  $\Delta t_2$  is limited by the syringe pump speed in respect to reaching the desired pressure level. It can therefore not be limitlessly shortened, but it can, however, be made longer if necessary.

The performance of the sample actuation method was evaluated in terms of the number of samples per chip reaching the designated chamber during a cycle consisting of an actuation pulse followed by a pull-in pulse. Sample mixed with mastermix and enzymes was used as working liquid. Seven chips were evaluated with respect to sample transfer. For transfer between the metering channel and CH1, 52 of 56 channels were successfully moved during the pulsing, corresponding to a yield of 93%. During transfer between CH1 and CH2, 52 out of 56 channels were successfully actuated, i.e. a yield of 100%. The reason for the malfunction of the transfer between the metering channel and CH1 was observed to be premature breaking of the capillary valve V2 during the pull-in pulse, despite the fact that this pulse had an amplitude well below the design burst pressure of this valve. Consequently, the liquid sample was transferred into CH2 instead of being retained inside CH1. It is suspected that the premature breaking of V2 is due to issues associated with the hydrophobic spotting. For an in-depth discussion of the spotting procedure, see [27]. Nevertheless, this issue should be possible to resolve by alteration of the design of the second capillary valve and by alterations of the actuation pulse time sequence.

### Overall fluidic performance

The overall fluidic yield of the developed microchip is the combination of the individual yields for the sample metering, the transfer between the metering channel and CH1, and the

transfer between CH1 and CH2. Based on the numbers presented above, the overall yield is 92% at present. Although

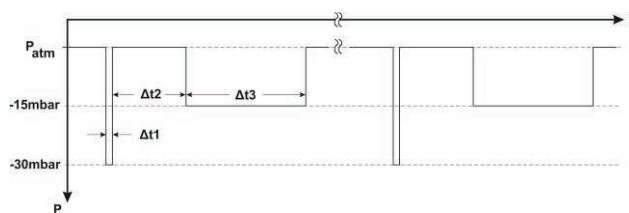


Fig. 6 Sample actuation scheme used for flow control on the microfluidic chip. First, a short pressure pulse of high amplitude was issued to break the capillary pressure barrier. This pulse was followed by a longer, low-amplitude pulse to move the liquid plug into the first reaction chamber, i.e. downstream toward the next capillary valve. The same procedure was repeated to overcome the second capillary valve and to position the liquid in the second reaction chamber.

this is not yet sufficient in a commercial perspective, it shows great potential for the developed prototype system. With minor design changes of the fluidic microchannel system and further optimization of manufacturing processes and surface modification methods, the microfluidic chip with its control instrument have the potential to achieve the level of reliability required for a commercial biomedical system.

### Optical performance

#### Signal to noise ratio

In order to determine the most suitable detection hardware for the fluorescent signal readout, three different types of detectors were tested, all from Hamamatsu; an avalanche photo diode (APD Module C5460-01), a Multi-Pixel Photon Counter (MPPC module C10507-11-050U) and a photo multiplier tube (PMT module H5784-02). The PMT control voltage was set to 0.722 V. Results obtained with the MPPC detector and a  $\sim 500\text{nL}$  fully amplified NASBA sample showed an SNR of 460. The corresponding SNR for the APD was 185 and for the PMT the SNR was 3750. Despite the superior performance of PMT, the MPPC detector was chosen as it fulfilled the sensitivity requirements for the NASBA detection at the lowest cost.

#### Fluorescence signal strength

The response of the optical system was tested by performing a NASBA amplification protocol on a sample containing positive control of the Human Papilloma Virus (HPV) subtype 16. All reagents including the purified sample solution were pre-mixed off-chip, whereafter the mixture was pipetted onto the sample inlet of the chip. The subsequent fluidic operations (sample loading, splitting, metering, waste discharge, heating and parallel actuation) and optical real-time detection was carried out automatically, as described in previous sections.

The real-time fluorescence emission curves for the eight parallel channels during on-chip NASBA amplification are shown in Fig. 7. Each of the sigmoid-shaped curves represents

a positive amplification. In addition, the fluorescence signal recorded during NASBA performed on a negative control sample is included for comparison.

5 For the positive control samples, the fluorescent signal detected in each channel was at the same level during the lag (amplification) phase. However, at the end of the assay, the curves display several intensity levels. This is typical behaviour and is also observed in macro scale experiments.  
10 The signal from the negative control remained constant throughout the assay as expected, due to the absence of amplification. The presented data clearly demonstrate the capability of the developed optical system to detect NASBA amplification in a parallel channel system containing ~500nl  
15 samples.

The signal strength from a fully amplified NASBA depends mostly on the fluorescent probe efficiency, and is therefore comparable to other isothermal amplification techniques as  
20 well as PCR if the same type of probes is applied. The detector system should thus yield similar SNR and signal levels for other amplification techniques.

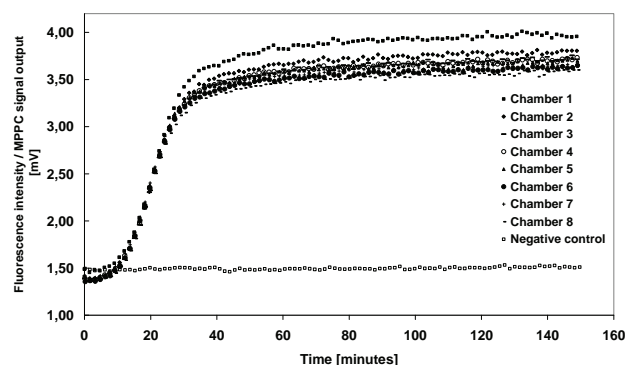
## Conclusions and outlook

25 We have developed a microfluidic platform capable of sample parallelization, sequential fluidic control and highly sensitive fluorescence detection. The system consists of a disposable microfluidic chip and an external control instrument. After insertion of chip into the instrument and  
30 infusion of sample onto the chip inlet, the entire assay procedure is completely automated, requiring no further user interaction.

The microfluidic chip functionality is based on passive  
35 components only, and it can be realized using commercially available mass production methods. Sample loading, metering and waste discharge is based exclusively on capillary flow. External actuation for on-chip flow control is required during sequential movement of subsamples through the parallel  
40 reaction channels. This is accomplished via a single fluidic interface between the chip and the instrument. Due to a novel flow control concept relying on pressure pulses, very good control of the fluidics is achieved using a simple external hardware setup. Although demonstrated on a chip containing  
45 eight parallel channels, the actuation method is easily scalable to larger parallel systems. The overall fluidic yield of the current system was found to be 92%, revealing great potential in the developed prototype.

50 The fluorescence detection unit is based on an optical probe scanner with fiber optical coupling to stationary illumination and detection optics. An MPPC is used as detector for the fluorescent signal, with an SNR of 460. The sensitivity of the system was tested during on-chip NASBA amplification of  
55 ~500nl positive control samples. The recorded real-time fluorescence signal from the parallel reaction chambers exhibited excellent characteristics unambiguously showing

positive amplification.



60 Fig. 7 Fluorescence signal reading from eight parallel reaction channels during NASBA amplification of pre-mixed positive control. In addition, a signal curve recorded during NASBA amplification of a negative control is included for comparison. The negative control shows no amplification  
65 and thus results in a flat response curve, in contrast to the characteristic sigmoid-shaped response curves of the amplified positive controls.

The microfluidic system presented herein constitutes a  
70 general platform for fluorescence based, multi-target biochemical assays. With dried reagents in the reaction chambers of the chip, and in combination with the developed automated sample preparation module,<sup>12</sup> a completely autonomous, automated amplification and detection system  
75 with disposable analysis chips and sample in – answer out capability can be realized.

## Acknowledgements

This work was funded by the European Commission under contract no. IST-NMT-CT-2005-017319 and by the Research Council of Norway under grants no. 182229 and 165853.

## Notes

\* Corresponding author.

<sup>a</sup> SINTEF ICT, Dept. of Microsystems and Nanotechnology,

85 Gaustadalleen 23C, 0314 Oslo, Norway. Fax: +47 22067321; Tel: +47 22067300; E-mail: [Michal.Mielnik@sintef.no](mailto:Michal.Mielnik@sintef.no)

<sup>b</sup> SINTEF Materials and Chemistry, Forskningsveien 1, 0314 Oslo, Norway

<sup>c</sup> University of Freiburg, Department of Microsystems Engineering

90 (IMTEK), Georges-Köhler-Allee 106, 79110 Freiburg, Germany

<sup>d</sup> BioFluidix GmbH, Georges-Köhler-Allee 106, 79110 Freiburg, Germany

<sup>e</sup> NorChip AS, Industriveien 8, 3490 Klokke, Norway

<sup>f</sup> Institut für Mikrotechnik Mainz, Carl-Zeiss Straße 18-20, 55129 Mainz, Germany

95 <sup>g</sup> Department of Pathology, Coombe Women and Infants University Hospital, Dublin, Ireland

<sup>h</sup> present address: Technische Universität Darmstadt, Center of Smart Interfaces, Petersenstraße 32, 64287 Darmstadt

---

## References

- 1 U. Bilitewski, M. Genrich, S. Kadow and G. Mersal, *Anal Bioanal Chem*, 2003, **377**, 556-569.
- 2 S. Haeberle and R. Zengerle, *Lab Chip*, 2007, **7**, 1094-1110.
- 3 V. Linder, *Analyst*, 2007, **132**, 1186-1192.
- 4 R. K. Saiki, S. Scharf, F. Faloona, K. B. Mullis, G. T. Horn, H. A. Erlich and N. Arnheim, *Science*, 1985, **230**, 1350-1354.
- 5 Y. Zhang and P. Ozdemir, *Anal. Chim. Acta*, 2009, **638**, 115-125.
- 6 P.-A. Auroux, Y. Koc, A. deMello, A. Manz and P.J.R. Day, *Lab Chip*, 2004, **4**, 534-546.
- 7 L. Chen, A. Manz, P.J.R. Day, *Lab Chip*, 2007, **7**, 1413-1423.
- 8 C.J. Easley, J.M. Karlinsey, J.M. Bienvenue, L.A. Legendre, M.G. Roper, S.H. Feldman, M.A. Hughes, E.L. Hewlett, T.J. Merkel, J.P. Ferrance and J.P. Landers, *PNAS*, 2006, **103**, 19272-19277.
- 9 J.-G. Lee, K.H. Cheong, N. Huh, S. Kim, J.-W. Choi and C. Ko, *Lab Chip*, 2006, **6**, 886-895.
- 10 J.W. Hong, V. Studer, G. Hang, W.F. Anderson, S.R. Quake, *Nat Biotechnol*, 2004, **22**, 435-439.
- 11 Web address: <http://www.sintef.no/microactive>
- 12 T. Baier, T.E. Hansen-Hagge, R. Gransee, A. Crombé, S. Schmahl, C. Paulus, K.S. Drese, H. Keegan, C. Martin, J. O'Leary, L. Furuberg, L. Solli, P. Grønn, I.M. Falang, A. Karlgård, A. Gulliksen and F. Karlsen, *Lab Chip*, DOI:10.1039/B910421F.
- 13 A. Gulliksen, M.M. Mielnik, E. Hovig, F. Karlsen, L. Furuberg and R. Sirevåg, *Proc. 11<sup>th</sup> International Conference on Miniaturized Systems for Chemistry and Life Sciences (MicroTAS)*, 2007, **1**, 673-675.
- 14 K. Abravaya, J. Huff, R. Marshall, B. Merchant, C. Mullen, G. Schneider and J. Robinson, *Clin Chem Lab Med*, 2003, **41**, 468-474.
- 15 J. Compton, *Nature*, 1991, **350**, 6313, 91-92
- 16 P. Gill and A. Ghaemi, *Nucleosides, Nucleotides, and Nucleic Acids*, 2008, **27**, 224-243.
- 17 G. Leone, H. vanSchijndel, B. vanGemen, F. R. Kramer and C. D. Schoen, *Nucleic Acids Res*, 1998, **26**, 2150-2155.
- 18 S. Tyagi and F. R. Kramer, *Nat Biotechnol*, 1996, **14**, 303-308
- 19 C. C. Ginocchio, M. Kemper, K. A. Stellrecht and D. J. Witt, *J Clin Microbiol*. 2003, **41**, 1, 164-173.
- 20 T. Molden, I. Kraus, F. Karlsen, H. Skomedal, J. F. Nygård and B. Hagmar, *Cancer Epidemiol Biomarkers Prev*, 2005, **14**, 2, 367-372.
- 21 J. D. Fox, *J. Clin. Virol.*, 2007, **40**, Suppl. 1 S15-S23.
- 22 Gulliksen A, Solli L, Drese K S, Sørensen O, Karlsen F, Rogne H, Hovig E, and Sirevåg R, *Lab Chip*, 2005, **1**, 416-420
- 23 Gulliksen, A., Solli, L., Karlsen, F., Rogne, H., Hovig, E., Nordstrøm, T., Sirevåg R., *Anal. Chem.*, 2004, **76**, 9-14
- 24 T. Tofteberg, H. Amédro and E. Andreassen, *Polymer Engineering and Science*, 2008, **48**, 2134-2142.
- 25 H. Cho, H.Y. Kim, J.Y. Kang, T.S.Kim, *J. Colloid Interface Sci*, 2007, **306**, 379-385.
- 26 L. Furuberg, M. Mielnik, A. Gulliksen, L. Solli, I.-R. Johansen, J. Voitel, T. Baier, L. Riegger and F. Karlsen, *Microsystem Technologies*, 2008, **14**, 673-681.
- 27 L. Riegger, M.M. Mielnik, A. Gulliksen, D. Mark, J. Steigert, S. Lutz, M. Clad, R. Zengerle and P. Koltay, *J. Micromech. Microeng.*, submitted.

# PAPER E

Erik Andreassen, Terje R. Tofteberg and Mariusz Blochowiak

## **New data testing the universality of chain dynamics in polymers**

Submitted for possible journal publication 2009

---

# New data testing the universality of chain dynamics in polymers

Erik Andreassen\*, Terje R. Tofteberg and Mariusz Blochowiak

SINTEF Materials and Chemistry, PO Box 124 Blindern, 0314 Oslo, Norway

The existence of an almost universal  $T_g/T$  dependence ( $T$  is the temperature and  $T_g$  is the glass transition temperature) of chain relaxation times ( $\tau_c$ ) of different polymers was proposed by Ding and Sokolov<sup>1</sup> and confirmed by Liu et al.<sup>2</sup>, but repudiated by Ngai et al.<sup>3</sup>. This paper presents new experimental data in the Williams-Landel-Ferry (WLF) region ( $T_g/T \sim 0.75$ ) which do not support the proposed universality, at least not with a strict definition.

Ref 1 was based on  $\tau_c(T)$  data directly measured with dielectric and dynamic mechanical spectroscopy, as well as some data calculated from zero-shear viscosities  $\eta_0$  and steady-state compliances  $J_s$ :

$$\tau_c(T) = J_s(T) \eta_0(T) \quad (1)$$

Ref 2, on the other hand, considered time-temperature shift factors  $a_T(T)$  from superposition of dynamic (rheometry) moduli. Details of the superposition were not given, but our experience is that  $a_T(T)$  obtained from dynamic data covering temperatures from the glass transition temperature up to the terminal relaxation zone will have a temperature dependence near  $T_g$  that is more representative of the segmental relaxation than of the chain relaxation<sup>4</sup>.

This note is based on data from creep measurements of melts, probing long relaxation times representative of the chain relaxation. Our data fulfill the three requirements put forward by Ngai et al.<sup>3</sup> for assessing the universality of chain relaxation time vs.  $T_g/T$ . We also present some data on related temperature dependence issues: The fragility indices of relaxation times  $\tau(T)$  and viscosities:

$$m = d(\log \tau) / d(T_g/T) \Big|_{T=T_g} \quad (2)$$

and the different temperature dependencies of segmental and chain relaxation times, i.e. breakdown of the time-temperature superposition principle.

Melt rheology data for four different commercial amorphous polymers (Table 1), all with relatively low viscosity, are presented below. The temperature dependence of zero-shear viscosities  $\eta_0(T)$  and steady-state compliances  $J_s(T)$  were obtained by shear creep measurements. In addition, the temperature dependence of the segmental relaxation time was assessed by

dynamic rheometry. Only shift factors obtained by time-temperature superposition of dynamic data encompassing the segmental relaxation were used for this purpose. The same data were used to determine  $T_g$  ( $T_{g,dyn}$  in Table 1). Note that shift factors from creep measurements gave a good superposition of the dynamic data in the terminal flow zone, while at lower temperatures the temperature dependency of the dynamic data was clearly higher than that given by the shift factors from creep<sup>4</sup>. Temperature dependencies from both creep and dynamic measurements were well fitted by the WLF equation or the equivalent Vogel-Fulcher-Tamman (VFT) equation.

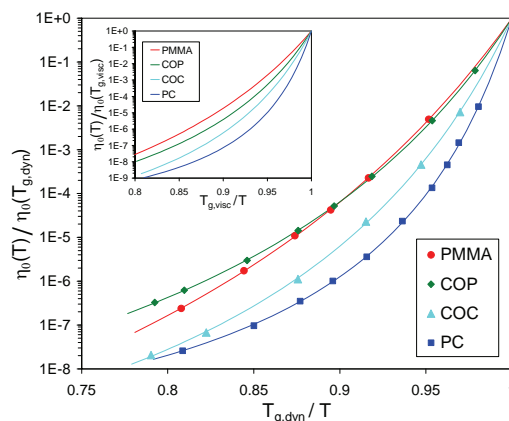


**Figure 1.**  $T_g$ -normalized temperature dependence of zero-shear viscosity from creep measurements. *Symbols:* Experimental data. *Lines:* VFT fits.  $T_{g,dyn}$  is defined in Table 1.  $\eta_0(T_{g,dyn})$  is calculated using VFT parameters. The insert diagram is based on an alternative definition of  $T_g$ :  $\eta_0(T_g = T_{g,visc}) = 10^{12}$  Pa-s, and  $T_{g,visc}$  is calculated using VFT parameters.

Data from creep measurements in Figure 1 shows that these polymers have quite different temperature dependencies near  $T_g$ . The PC has the strongest temperature dependence. This is reflected in the fragility indices; the  $m_v$  and  $m_c$  values in Table 1. (The fragility index is usually defined in terms of the segmental relaxation, but, following Ding and Sokolov<sup>1</sup>, we also calculate fragility indices for the chain relaxation time and the viscosity.) For these four polymers,  $m_c$  values are correlated with  $T_g$  values. The  $m_c$  values of the PMMA, the COC and the COP are in the ranges reported in ref 1 (6 polymers with  $m_c$  in the range 42-50) and ref 5 (12 polymers with  $m_c$  in the range 50-90). However, our PC has a higher  $m_c$  than reported in refs 1 and 5. In fact, ref 5 reported a

\* Corresponding author. E-mail: erik.andreassen@sintef.no

higher  $m_c$  value for a PMMA than for a PC. Ref 1 reported an  $m_c$  value close to 50 for a PC, based on published data obtained with a penetration viscometer<sup>6</sup> (temperature dependence of steady-state compliance neglected, i.e.  $m_c = m_v$ ). The  $T_g$  was not given in ref 6, but with the VFT parameters for the PC in ref 6 we obtain  $m_v$  values in the range 71-87 ( $T_g$  in the range 150-144 °C). This is still lower than the value in Table 1. However, note that Ngai et al.<sup>3</sup> criticized the quantitative reliability of the data in ref 6, as well as the high  $T_g$  (154 °C) used to calculate the  $m_c$  value in ref 1.

**Table 1.** Materials, glass transition temperatures and fragility indices.

Material	$T_{g,DSC}^e$ [°C]	$T_{g,dyn}^f$ [°C]	$m_v^g$	$m_c^h$	$m_s^i$
PC <sup>a</sup>	140.7	141.8	127	106	143
COC <sup>b</sup>	132.0	132.4	83	64	108
COP <sup>c</sup>	101.8	101.9	61	46	134
PMMA <sup>d</sup>	101.6	101.0	55	49	70

<sup>a</sup>Bisphenol A polycarbonate (Lexan OQ1026 from Sabic Innovative Plastics) with  $M_w$  18 kg/mol and  $M_w/M_n \sim 2.3$ . This PC is produced in a melt-transesterification process (known to induce some branching), and has on the average less than 0.1 branches per chain.

<sup>b</sup>Polymethylmetacrylate (Plexiglas POQ62 from Evonik Röhm) with  $M_w$  85 kg/mol,  $M_w/M_n \sim 2$ , syndiotactic content 52 % and isotactic content 6 %.

<sup>c</sup>Cyclic olefin copolymer (Topas 5013S-04 from Topas) with  $M_w$  92 kg/mol and  $M_w/M_n \sim 2$ . This is an ethylene-norbornene random copolymer with about 50 mol% norbornene, produced by chain copolymerization<sup>7,8</sup>.

<sup>d</sup>Cyclic olefin polymer (Zeonor 1060R from Zeon) produced by ring-opening metathesis polymerization of a norbornene derivative followed by complete hydrogenation of double bonds<sup>7</sup>.

<sup>e</sup> $T_{g,DSC}$  is the glass transition temperature obtained by differential scanning calorimetry; determined from the inflection point of the second heating at 10 K/min.

<sup>f</sup> $T_{g,dyn}$  is the glass transition temperature obtained from dynamic rheometry. In this study it is defined by  $\tau_s(T_g) = 30$  s, where  $\tau_s$  is the segmental relaxation time<sup>9</sup>.

<sup>g</sup> $m_v$  is the viscosity fragility index calculated analytically (in analogy with Eq 2) from the VFT temperature dependence of the zero-shear viscosity from creep measurements. The  $T_g$  used in the calculation of  $m_v$  is  $T_{g,dyn}$ .

<sup>h</sup> $m_c$  is the chain relaxation fragility index, calculated analytically (Eq 2) from the VFT temperature dependence of the relaxation time  $\tau_c(T)$  obtained by Eq 1, using data from the creep measurements. The steady-state compliance  $J_s$  is constant at high temperatures and decreases when the temperature approaches  $T_g$ . The  $T_g$  used in the calculation of  $m_c$  is  $T_{g,dyn}$ . Note that  $m_c$  has larger experimental error than  $m_v$ .

<sup>i</sup> $m_s$  is the segmental relaxation fragility index calculated analytically (Eq 2) from the WLF temperature dependence (superposition) of dynamic rheology data encompassing the segmental relaxation. The  $T_g$  used in the calculation of  $m_s$  is  $T_{g,dyn}$ . Note that  $m_s$  has larger experimental error than  $m_v$ .

Above  $T_g$ ,  $\eta_0(T_g/T)$  for the four polymers display different slopes and curvatures (Figure 1). From  $T_g/T = 0.9$  to  $T_g/T = 1$  the viscosity of the PC increases almost two decimal orders of magnitude more than that of the PMMA and the COP, while at  $T_g/T = 0.8$  the PC has lower temperature sensitivity than the PMMA. For the alleged universal curve in ref 1,  $\tau_c$  increases by a factor  $\sim 10^4$ - $10^5$  from  $T_g/T = 0.9$  to  $T_g/T = 1$ . This is comparable to our data:  $\tau_c$  of the PMMA increases by a factor somewhat below  $10^4$ , while  $\tau_c$  of the PC increases by factor close to  $10^5$ . The corresponding increase in  $a_T(T)$  in ref 2 is  $\sim 10^5$ - $10^6$  and the slope 3 line vs.  $T_g/(T - 0.77T_g)$  in ref 2 gives a factor  $10^{4,3}$ .

Slightly different  $T_g$  values (within the uncertainty) will not cause significant changes in Figure 1 or a similar plot for  $\tau_c$ . If we disregard the VFT extrapolations to temperatures below the actual measurements (both due to the uncertain validity of the extrapolation and the experimental uncertainty in  $J_s(T)$  near  $T_g$ ), and allow for the data of different polymers to be shifted vertically independently of each other, there will still be distinct differences between the curvatures.

In Figure 1 the viscosities are normalised by  $\eta_0(T_{g,dyn})$ . The  $\eta_0(T_{g,dyn})$  values differ somewhat between the four materials, in the range  $\sim 10^{10}$ - $10^{11}$  Pa·s. Alternatively,  $T_g$  can be defined by the viscosity level, and  $\eta_0(T_{g,visc}) = 10^{12}$  Pa·s is sometimes used<sup>10</sup>. This definition is used in the insert in Figure 1. The trends remain the same, but the curves of PMMA and COP are now separated in the entire temperature range.

Liu et al.<sup>2</sup> showed that their  $\log a_T(T)$  data could be linearized in a plot vs.  $T_g/(T - 0.77T_g)$ , and their data followed a slope close to 3. Fig 2 shows a similar plot for our data set, when allowing data for different polymers to be shifted vertically independently of each other (disregarding the VFT extrapolation down to  $T_g$ ). PMMA data fall on the line with slope 3, while COP data seem to follow a slightly different slope. PC and COC data are not linearized. Still, the line with slope 3 represents the main trend in our data for these four polymers.

Finally, a few comments regarding the segmental relaxation fragility indices; the  $m_s$  values in Table 1. Kumal et al.<sup>11</sup> gave a qualitative picture of segmental fragility in polymers as influenced by the flexibility of the backbone and the sidegroups. However, there is considerable spread in experimentally determined fragility indices for a given polymer type<sup>1, 5, 10, 11</sup>, and this is probably partly due to different methods being used. Still, the PC (with a rigid backbone) having a higher  $m_s$  than the PMMA (Table 1) is in line with the literature<sup>5, 10</sup>. Furthermore, our  $m_s$  value

for the COC is close to a value published for a COC with the same norbornene content ( $m_s \sim 110$ )<sup>8</sup>. The relatively high  $m_s$  value of the COP compared to its  $m_c$  value was unexpected. Note that the COP has higher  $m_s$  than the COC, but lower  $T_g$ . For polymers there is often a positive correlation between  $T_g$  and  $m_s$ <sup>10, 11</sup>. However, Kunal et al.<sup>11</sup> suggested some separate factors controlling  $T_g$  and  $m_s$ , respectively.

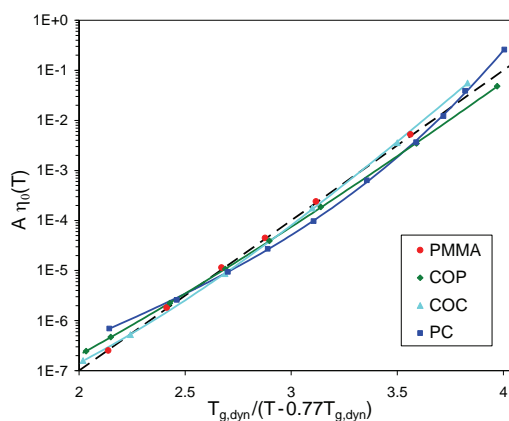


**Figure 2.** This figure is based on the same data as Figure 1, but the data points are shifted vertically on the log scale with different factors  $A$  for each material. The abscissa and the dashed line with slope 3 are mentioned in the main text. Solid lines are guides for the eye.

For a given material, the  $m_s$  value is larger than the  $m_c$  value, as reported earlier<sup>1, 5</sup>. The differences between the four polymers regarding the decoupling of segmental and chain dynamics (different temperature dependencies) near  $T_g$ , is represented by the ratio  $m_s/m_c$ . It has been reported that the decoupling is stronger in more fragile polymers<sup>1</sup>. However, this is not observed in our study. For instance, the most fragile polymer (PC) has a rather low  $m_s/m_c$  ratio.

In conclusion, we observe a clear effect of chemical structure on the temperature dependence of the chain relaxation time in the temperature interval  $T_g/T$  from 0.8 to 1. For the four polymers in this study, there is a positive correlation between  $T_g$  and the temperature sensitivity of the chain relaxation time near  $T_g$ . Hence, these four polymers do not display the universality proposed in ref 1, at least not with a strict definition. Furthermore, the effect of chemical structure is similar for segmental relaxation fragility and chain relaxation fragility.

**Acknowledgement.** This study was funded by the Research Council of Norway.

## References and Notes

- (1) Ding, Y. F.; Sokolov, A. P., *Macromolecules* **2006**, *39*, 3322-3326.
- (2) Liu, C. Y.; He, J. S.; Keunings, R.; Bailly, C., *Macromolecules* **2006**, *39*, 8867-8869.

- (3) Ngai, K. L.; Plazek, D. J.; Roland, C. M., *Macromolecules* **2008**, *41*, 3925-3929.

(4) With the frequency intervals in typical dynamic rheometry measurements, the segmental relaxation is only probed at the lowest temperatures, while the chain relaxation is only probed at the highest temperatures. Hence, if the entire data set, spanning from the terminal flow zone to the glass transition, is subjected to a time-temperature superposition, the temperature dependence of the resulting shift factor,  $a_T(T)$ , will be dominated by the segmental relaxation at low temperatures and by the chain relaxation at high temperatures. This is why superposition of the entire data set may still yield reasonable estimates for the fragility index  $m_s$ . Also, the resulting master curve may appear OK, but thermorheological complexity is indirectly circumvented.

- (5) Sokolov, A. P.; Schweizer, K. S., *Phys. Rev. Lett.* **2009**, *102*, 248301.

- (6) Yang, F. Q., *Polym. Eng. Sci.* **1997**, *37*, 101-104.

- (7) Shin, J. Y.; Park, J. Y.; Liu, C. Y.; He, J. S.; Kim, S. C., *Pure Appl. Chem.* **2005**, *77*, 801-814.

- (8) Blochowiak, M.; Pakula, T.; Butt, H. J.; Bruch, M.; Floudas, G., *J. Chem. Phys.* **2006**, *124*, 134903.

(9) The relaxation time was taken as the high-frequency cross-over between  $G'$  and  $G''$  (the storage and loss moduli) This time was extrapolated with the WLF parameters obtained by superposition of dynamic rheology data encompassing the segmental relaxation. The 30 s criterion was chosen to obtain  $T_g$  values similar to those from DSC. If, instead, the relaxation time was defined by the  $\tan\delta$  peak ( $\tan\delta = G''/G'$ ), a criterion of 100 s was more appropriate. A criterion of 100 s is often used for  $T_g$ <sup>3, 10</sup>. However, in some dynamic rheometry studies a relaxation time as short as 1 s is used<sup>8</sup>. This may be due to the fact that the WLF factors are based on the whole master curve (including the terminal flow zone), thereby underpredicting the temperature dependence of the segmental relaxation when approaching  $T_g$ . Hence, to obtain a reasonable  $T_g$  value, the  $T_g$  criterion must be based on a rather short relaxation time.

- (10) Qin, Q.; McKenna, G. B., *J. Non-Cryst. Solids* **2006**, *352*, 2977-2985.

- (11) Kunal, K.; Robertson, C. G.; Pawlus, S.; Hahn, S. F.; Sokolov, A. P., *Macromolecules* **2008**, *41*, 7232-7238.

---

# PAPER F

Terje R. Tofteberg, Hélène Amédéo, Frode Grytten and Erik Andreassen

## **Effects of injection molding holding pressure on the replication of surface microfeatures**

Accepted for publication in International Polymer Processing (2010)



# Effects of injection molding holding pressure on the replication of surface microfeatures

Terje R. Tofteberg, H el ene Am edro, Frode Grytten, Erik Andreassen  
*SINTEF Materials and Chemistry, Oslo Norway*

The injection molding of an optical grating was studied using two different polycarbonates. The grating has period 10  $\mu\text{m}$  and peak-to-valley distance  $\sim 1 \mu\text{m}$ . Parts were molded using different holding pressures and mold temperatures. After production, the parts were annealed at 100  $^\circ\text{C}$ . The replication was investigated using white light interferometry (WLI) before and after annealing. WLI was performed using high definition vertical-scanning interferometry (HDVSI) to resolve the details of the molded gratings with a noise level below 2 nm.

It was observed that an increasing holding pressure had both positive and negative effects on the replication. When the microfeatures were not fully filled, an increased holding pressure improved the definition of the features. However, for both polymers, it was observed that the replication as a function of holding pressure started to drop when the holding pressure was increased above an optimal value. It is believed that this was due to elastic recoil occurring after the holding pressure was released.

The peak-to-valley distance of the grating was reduced after annealing. This effect was larger for parts molded using a low mold temperature. This is probably due to a higher cooling rate giving higher internal stresses, which will relax during annealing.

## INTRODUCTION

The optical functionality of polymer parts can be tailored by modifying the surface structure on the microscale. This has been used in commercial applications such as optical storage media and light guide plates for LCD displays. Emerging commercial applications include among others sensors based on diffractive optics.

Injection molding is seen as a viable fabrication method for producing diffractive optics and other microfeatured components. As such components are finding increased usage, it becomes important to know how well the microfeatures are replicated and for how long the features will stay well defined.

Several studies have investigated how the injection molding processing settings influence the replication of microfeatures. A high mold temperature is generally

considered to be an essential factor positively influencing the replication [1-5]. However, keeping a high mold temperature will usually increase the cooling time, giving an increased cycle time and cost per unit [2]. A too high mold temperature may also in some cases damage the microfeatures [6]. To avoid the increase in cooling time, much effort has been made to develop methods which ensure a high mold surface temperature during the injection phase and a low mold surface temperature during the cooling phase. A summary of these methods for rapid thermal cycling can be found in a review by Yao et al. [7].

A high injection velocity is also found to be beneficial for the replication of microfeatures [1, 3, 8]. It has been shown that increasing the injection speed far above what is common in conventional injection molding has a positive effect on the replication [4]. However, in many cases, the maximum injection velocity will be limited by the maximum injection pressure or the maximum clamping force of the injection molding machine.

The effect of the holding pressure on replication of microfeatures is more mixed. Some studies report a positive effect on replication [9, 10]. Han et al. [8] observed improved filling of a surface grating with increased holding pressure, but the effect of the holding pressure decreased when the thickness of the main geometry decreased. This is in line with the effect of holding pressure for injection molding in general: As the part thickness is reduced, there is less need for holding pressure to reduce sink marks etc. Yoshii et al. [11] also reported a positive effect, but noted that backflow through the gate could cause a reduction in replication. The reduction was explained by recovering elasticity and thermal shrinkage.

Other studies report that the effect of holding pressure can be either positive or negative depending on the material used. Sha et al. [2], found that the achievable microfeature aspect ratio for parts molded in POM<sup>†</sup> increased with holding pressure, whereas it decreased for parts molded in PP<sup>†</sup> and ABS<sup>†</sup>. They did not provide an explanation for this and inquired further research on the matter. Kalima et al. [12] reported that applying a high holding pressure had a negative effect

---

<sup>†</sup> POM = polyoxymethylene, PP = polypropylene, ABS = acrylonitrile butadiene styrene, PC = polycarbonate, SAN = styrene acrylonitrile, COP = cyclic olefin polymer, PS = polystyrene

on the replication of a surface grating with three of the materials investigated (PC<sup>†</sup>, SAN<sup>†</sup> and COP<sup>†</sup>), but it had a positive effect with the last material, a fluoropolymer. Murakami et al. [13] investigated the filling of microscale V-grooves in PCs with different molecular weights and processing settings. They observed both positive and negative effects of increasing the holding pressure.

Some studies report a maximum in the replication as function of holding pressure. Xu et al. [5] observed a maximum in the achieved microfeature filling length as a function of holding pressure for parts molded in PP<sup>†</sup>. For parts molded in PS<sup>†</sup>, Arlø and Kjær [14] found, to their surprise, that the replication of surface roughness passed through a maximum as a function of holding pressure.

As far as we have found, none of these studies provide an explanation as to how an increased holding pressure could reduce the replication of microfeatures. In this study we investigate in detail how the shape of the molded microfeatures changes when the holding pressure is varied. We also suggest an explanation for the drop in replication when applying a high holding pressure.

Finally, note that for injection molding in general the holding pressure and its optimized profile versus time are key parameters for part quality [15], but a high holding pressure can also have adverse effects such as high residual stresses, which can for example cause high optical birefringence and premature fracture.

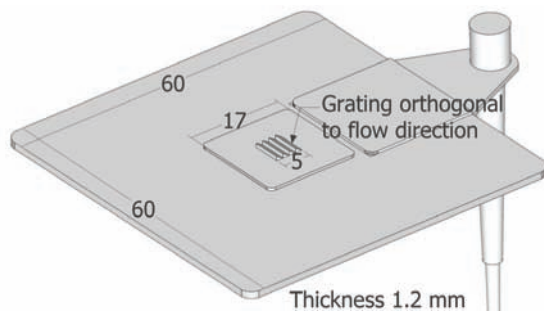


Fig. 1 Injection molded part with dimensions [mm]. The optical grating has a period 10  $\mu\text{m}$  and peak-to-valley distance  $\sim 1 \mu\text{m}$ . The grating is indicated (but not to scale) at the center of the part.

## EXPERIMENTAL

### Part geometry

A model of the injection molded part is shown in Fig. 1. It is a macroscopic part with a microscale optical grating. The grating has a period of 10  $\mu\text{m}$  and peak-to-valley distance  $\sim 1 \mu\text{m}$ . The nickel mould insert for this grating was made by electron beam lithography, followed by electroplating with nickel. The 0.3 mm thick mold insert (shim) was fixed in a modular mold with the grating orthogonal to the flow direction as indicated in Fig. 1.

### Polymers

Two different bisphenol A polycarbonates were used in this study; one grade designed for use in car headlight systems (LEXAN LS2 from Sabic Innovative Plastics, Europe) and one low molecular weight DVD grade (LEXAN OQ1026 from Sabic Innovative Plastics, Europe). The two polymers will be referred to as PC-H and PC-L respectively in the remainder of the text. Some properties and production settings for the two polymers are given in Table 1.

### Injection molding

The injection molding was performed on a servoelectric Battenfeld EM 50/120 machine with maximum clamping force 500 kN and screw diameter 25 mm. The parts were injection molded using a constant nominal volume flow. The flow front velocity given in Table 1 is this volume flow divided by the cross-sectional area of the part. The mold was tempered using circulating hot water and the mold temperature  $T_{\text{mold}}$  refers to the set water temperature. A combined pressure and temperature sensor (Kistler 6190BA) located in the mold surface opposite the microfeatures confirmed that this temperature was close ( $\pm 1 \text{ }^\circ\text{C}$ ) to the surface temperature when the melt was injected, and that the surface temperature at the start of filling was highly repeatable from shot to shot. After the end of filling, a constant holding pressure,  $p_{\text{hold}}$ , was applied. The value of this constant pressure (as measured in the barrel end-cap) was first chosen to approximately match the pressure at the end of the filling. Parts were then molded with different values for the holding pressure, both above and below this value. The holding pressure was held constant for three seconds and then linearly ramped down to zero over one second.

Table 1 Properties and molding conditions for the two polycarbonate materials.

Material	$T_g^1$ [ $^\circ\text{C}$ ]	$M_w^2$ [ kg/mol ]	$M_w/M_n^2$	Melt temperature [ $^\circ\text{C}$ ]	Flow front velocity <sup>3</sup> [ m/s ]	Melt pressure at switch-over <sup>4</sup> [ MPa ]
PC-H	144.5	26	2.3	310	0.5	$\sim 70$
PC-L	140.7	18	2.3	310	1.0	$\sim 140$

<sup>1</sup>The glass transition temperature, as obtained by differential scanning calorimetry; determined from the inflection point of the second heating at 10 K/min. <sup>2</sup>Data from the manufacturer.  $M_w$  is the weight average molecular weight and  $M_n$  is the number average molecular weight. <sup>3</sup>Nominal volume flow divided by cross sectional area at the location of the microfeatures <sup>4</sup>Measured melt pressure in the barrel end-cap at the switch-over from the filling stage to the holding stage.

At startup or when changing the mold temperature, the process cycle was allowed to stabilize for more than 50 cycles after the set water temperature had been reached for the water returning from the mold. After changing the holding pressure, five parts were produced to allow the process to stabilize, before taking the next four parts out for characterization.

### *Annealing*

After production, the injection molded parts were annealed at 100 °C in an oven with circulating air. The parts were characterized before annealing (approximately 2 hours after production, stored at room temperature) and also after 1 hour, 24 hours and 168 hours of annealing.

### *Characterization*

The parts were characterized using a white light interferometer (NT9800 from Veeco instruments) using high definition vertical-scanning interferometry (HDVSI) [16].

Given the phase information from an interferometry measurement, there is an ambiguity as to whether the vertical position of a point is located at a given  $z$  or at  $z + \frac{1}{2}n\lambda$  where  $n$  is an integer and  $\lambda$  is the wavelength of the light source. The instrument software tries to automatically reconstruct the surface by shifting the  $z$  values by  $\frac{1}{2}n\lambda$  with help from the best contrast location. However, the software did sometimes fail to reconstruct the surface resulting in artificial jumps of  $\frac{1}{2}n\lambda$ . These jumps were recognizable and corrected for by manually shifting data by an integer number of  $\frac{1}{2}\lambda$  (303.4 nm).

The total measurement time was approximately one minute per sample, and most of this was spent on aligning the sample and manual focusing.

It was difficult to distinguish the sample roughness from the measurement noise, but the noise level seemed to be below 2 nm for measurements on the molded samples. According to the manufacturer, the noise level should be approximately 0.3 nm. The low reflectivity of the two highly transparent polymers might have influenced the noise level negatively.

Images spanning 45  $\mu\text{m}$  by 60  $\mu\text{m}$  were taken at the same place on the grating for all the molded parts. A line from this image was used to investigate the replication quality. The peak-to-valley distance on four consecutive peaks were measured and used to quantify the replication quality.

When comparing the molded parts with the mold insert, all  $z$  values on the mold insert were inverted. The  $x$  and  $z$  values of the molded parts were shifted to best overlap with the mold insert. The molded parts were also tilted to ensure that the  $z$  coordinates of the valley locations were as equal as possible. In addition, to compensate for the shrinkage of the molded parts, all dimensions of the mold insert were scaled by a factor

0.994 when comparing with parts molded in PC-H and by a factor 0.990 for parts molded in PC-L. These factors were chosen in order to match the period of the molded gratings with the period of the grating on the mold insert.

## **RESULTS**

Surface topographies of parts molded at different conditions are shown in Fig. 2. Fig. 2a gives an indication of the combined repeatability of the molding process and the topography measurement. Fig. 2b shows how the replication is reduced by the annealing. In Fig. 2c an increased holding pressure has a mostly positive effect on the replication, whereas in Fig. 2d the effect is negative.

For all the parts molded in this study, profiles similar to those in Fig. 2 were extracted. The peak-to-valley distance was measured for each peak and the result before and after annealing is summarized in Fig. 3.

### *Planarity of the parts*

The area with microfeatures spanned 5 mm by 5 mm. The planarity over this area was characterized using WLI. It was found that the waviness over this area was similar in size to the peak-to-valley distance of the optical grating. The largest part of the waviness seemed to be caused by some thickness variations in the mold insert on the order of 1  $\mu\text{m}$ . We were not able to extract a curvature from the measurements, as any possible curvature was smaller than both the waviness and the peak height of the optical grating.

## **DISCUSSION**

### *Positive effect of increased holding pressure*

As reported in several other studies, a positive effect on replication was observed when increasing the holding pressure in some cases. This is best seen for PC-L at low temperatures as shown in Fig. 2c and Fig. 3b. Up to 75 MPa, an increased holding pressure leads to a better defined peak, caused by better filling of the microfeatures. When further increasing the pressure, the radius at the peak in the molded topography is decreased (the peak becomes sharper), but the overall peak height does not change. This can be seen in Fig. 2c, by comparing the topography of parts molded using a holding pressure of 75 MPa and 100 MPa.

### *Negative effect of increased holding pressure*

In some cases an increased holding pressure leads to a loss in replication as best seen in Fig. 2d. A maximum in the peak-to-valley height as a function of holding pressure was found for both polymers at all the mold temperatures in this study as shown Fig. 3. This observation is somewhat counterintuitive, as an increased holding pressure will push the polymer into the microfeatures with a greater force. Nevertheless, as mentioned in the introduction, several similar observations have been reported in the literature.

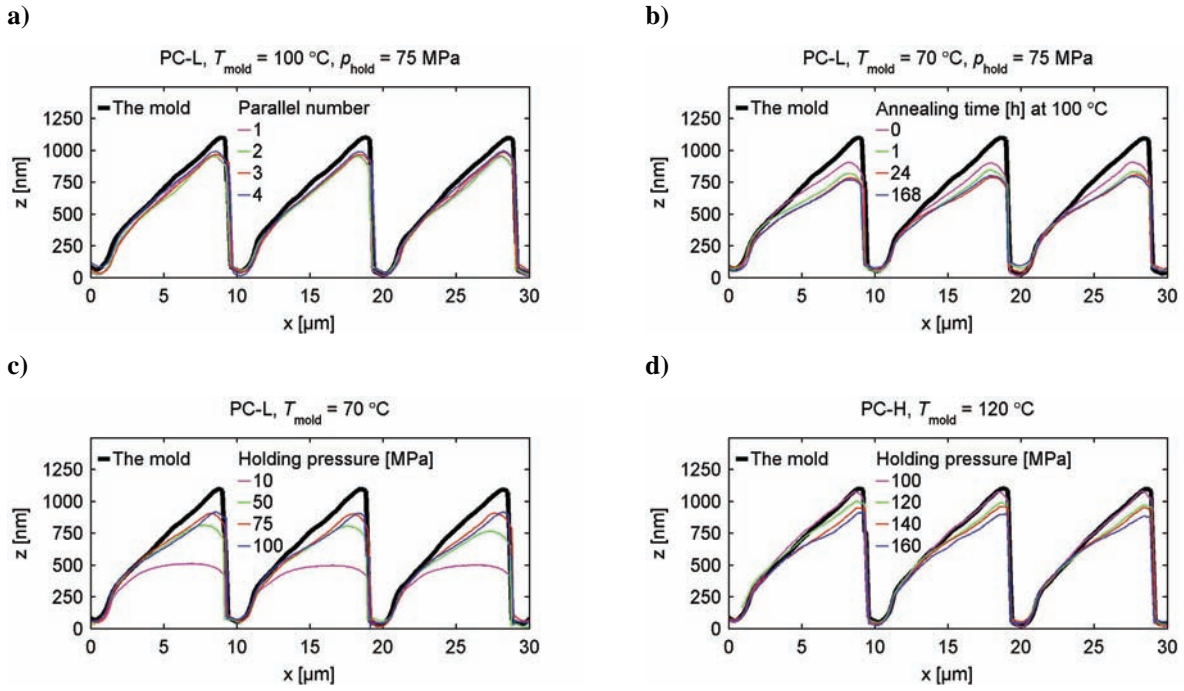


Fig. 2 Comparing the surface topography of molded parts with the mold. a.) Repeatability of molding process and measurement. Four parallel samples molded in PC-L using a mold temperature of 100 °C and holding pressure 75 MPa. b) Annealing of samples molded in PC-L with mold temperature 70 °C and holding pressure 75 MPa. c) Samples molded in PC-L with mold temperature 70 °C and different holding pressures. d) Samples molded in PC-H with mold temperature 120 °C and different holding pressures.

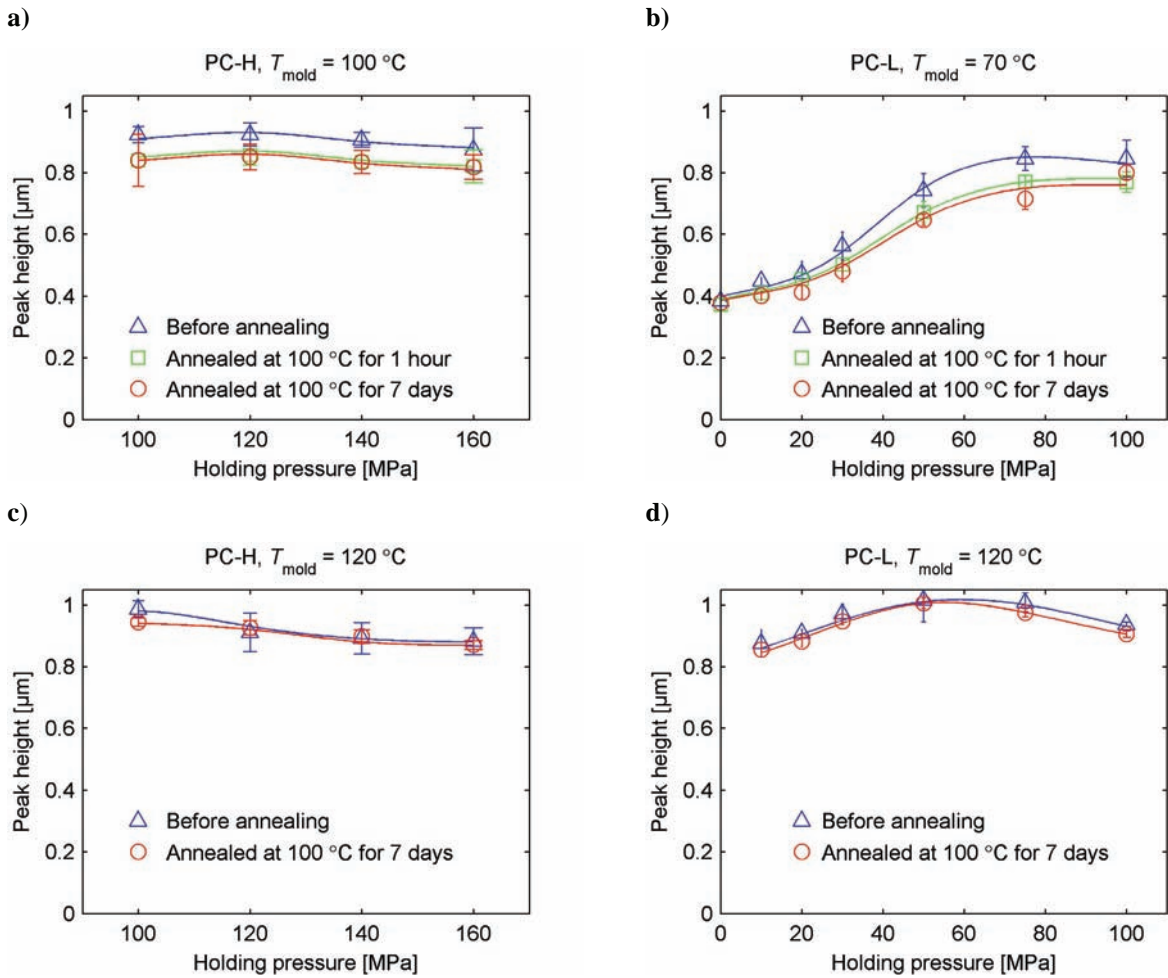


Fig. 3 Measured peak height as function of holding pressure. Four consecutive peaks were measured for each molded part, and the symbols show the mean value. The error bars show  $\pm 2$  standard deviations within the same group. The lines are added as guides for the eyes.

To explain this negative effect of an increased holding pressure, we start by observing how the shape of the molded grating deviates from the grating on the mold insert. For the parts shown in Fig. 2c, where an increased holding pressure improved the replication, the shape of the molded grating is in agreement with what we would expect if the polymer solidified before completely filling the mold insert. The peaks of the molded grating are less sharp than those of the mold insert. As the holding pressure is increased, the peak height increases and the peaks become sharper.

This is not the case for the topographies in Fig. 2d., except perhaps for the lowest holding pressure, the topography peaks are almost as sharp as in the mold insert, but the peak heights differ. This indicates that the polymer, at one point during the injection molding process, did fill the feature completely, but later lost some of its definition. We believe that most of this loss could be due to elastic recoil when the holding pressure was removed.

A quantitative description of this process would need to include both viscous and elastic effects. In addition, the polymer is cooled from a temperature close to 300 °C to a temperature close to 100 °C during the injection and holding stages of the injection molding process. This means that the material properties of the polymer entering the microfeatures will be very different from the material properties of the polymer recoiling from the microfeature.

Non-isothermal flow has been simulated with viscoelastic models, predicting high molecular orientation at the wall [17], and tensile stresses at the surface induced by pressure during solidification [18]. Residual stresses in injection molded PC, and conditions leading to tension at the surface have also been studied experimentally [19-21].

We can not yet provide a quantitative description, but propose two ways in which a higher holding pressure can lead to a stronger elastic spring back.

1.) A higher holding pressure will deform the material faster into the shape of the mold insert. If this deformation is faster, the temperature drop will also be faster, since good thermal contact is obtained at an earlier time. The thermal contact will also be better because of the high pressure, further accelerating the cooling. The elastic stresses thus have less time to relax at a high temperature and the stresses will be higher at the time the holding pressure is released. This could then lead to a larger elastic recoil and thus reduction in peak-to-valley distance.

2.) A higher holding pressure will deform the material at a higher strain rate. This will lead to higher stresses at the time the microfeature is completely filled.

#### *Mold deformation*

Because of the high pressures involved, there will

always be some mold deformation during injection molding. This is especially important to consider when molding parts with high tolerances where mold deformations might lead to significant variation in part thickness [22]. For small parts with thin walls this can be especially important since the pressure required to fill the thin cavity must be very high [23].

It could be suspected that some of the negative effect of a high holding pressure was linked to mold deformation. With the highest holding pressures, some mold deflection occurred and it was observed that the cavity pressure did not fall to zero after the melt pressure was removed (after the gate had solidified). Although the cavity pressure would force the polymer into the microfeatures of the mold insert, one could speculate that a fast mold deflection could produce some local gaps between the mold insert grating and the polymer grating (replicated prior to the holding stage), maybe because of the only partial replication, and the low surface roughness of the mold insert compared to the rest of the steel mold. The polymer would then need to fill this gap before proceeding with the replication of the grating. However, the peak profiles discussed above do not agree with such a hypothesis.

Furthermore, some finite element simulations were performed to assess the effect of cavity pressure on the grating on the nickel mold insert. Simulations were performed with a pressure load of 160 MPa applied at different locations (a higher local loading than a hydrostatic pressure). It was not possible to deform the mold insert so that the relative location of two points within one period of the grating moved by more than 2 nm. This is far from the observed shape deviation showed in Fig. 2d and it was concluded that local mold deformations could not be the reason for the observed effects.

#### *Effect of annealing*

After annealing, it was observed that some parts showed a reduction in peak height. After 1 hour at 100 °C, it seemed like this process ended. Most notable is the fact that parts molded at a high mold temperature showed a much smaller drop in replication after annealing than parts molded at a low mold temperature. This was true for both PC-H (comparing Fig. 3a and c) and PC-L (comparing Fig. 3b and d). The drop in replication after annealing is probably due to relaxation of tensile stresses frozen into the material during the rapid cooling during the molding process.

The cooling rate as the material passes through the glass transition will be higher for parts molded with a lower mold temperature. This will give less time for the stresses to relax during the molding process, and more relaxation will occur in the annealing process.

When investigating the series in Fig. 3b, it can be seen that the parts molded with the lowest holding pressures show the smallest drop in replication after annealing.

This indicates that it is tensile stresses introduced during the holding pressure phase that are relaxed during annealing.

Note that the annealing in this study was performed ~40 °C below the glass transition temperature of the polymers. If annealed at a temperature above or close to the glass transition temperature, the molded microfeatures will retract at a faster rate, and they will also be smoothed out even if no residual stresses are present. The surface tension will in such cases be the main contributing factor to the retraction [24]. Since most of the loss in peak height occurs during the first hour of annealing for then later to stop, it is concluded that it is not due to surface tension.

The timescale of the drop in replication in the annealing process matches the timescale of the stress relaxation in these polymers at 100 °C. The stress relaxation was measured in torsion using rectangular test bars (60 mm x 10 mm x 1.2 mm) machined from injection molded specimens. A small torsion angle was applied and the relaxation modulus was monitored. At 100 °C the stress had relaxed by 50% after 7 hours for PC-H and after 1.3 hours for PC-L.

## CONCLUSION

Both the polymers used in this study seem to be well suited for replication of microfeatures given the right processing conditions. In the present study it has been shown that an increased holding pressure can have both a positive and a negative influence on the replication of microfeatures.

A higher pressure will force the polymer to protrude further into the microfeatures. The deformation will be partly viscous and partly elastic. For low to moderate pressures, increasing the pressure will lead to improved definition of the features.

As the holding pressure is released, part of the elastic deformation will recoil. The experimental results in this work indicate that if the holding pressure is set at a higher value, this recoil will be larger. When the holding pressure is increased above a certain threshold value, the negative effect of larger recoil will outweigh the positive effect of improved filling and the net effect of increasing the holding pressure will be negative.

It is observed that the microfeatures on parts molded using a high mold temperature tend to have a smaller drop in peak height after annealing than parts molded with a low mold temperature.

## ACKNOWLEDGEMENTS

This study was funded by the Research Council of Norway.

## REFERENCES

1. T. Tofteberg, H. Amédéo and E. Andreassen, *Polym. Eng. Sci.*, **48**, 2134 (2008).
2. B. Sha, S. Dimov, C. Griffiths and M.S. Packianather, *J. Mater. Process. Tech.*, **183**, 284 (2007).
3. X. Han and H. Yokoi, *Polym. Eng. Sci.*, **46**, 1590 (2006).
4. H. Yokoi, X. Han, T. Takahashi and W.K. Kim, *Polym. Eng. Sci.*, **46**, 1140 (2006).
5. G. Xu, L. Yu, L.J. Lee and K.W. Koelling, *Polym. Eng. Sci.*, **45**, 866 (2005).
6. M.J. Madou, *Fundamentals of Microfabrication: The Science of Miniaturization, 2nd Edition*, CRC Press, (2002).
7. D. Yao, S.-C. Chen and B.H. Kim, *Adv. Polym. Technol.*, **27**, 233 (2008).
8. X. Han, H. Yokoi and T. Takahashi, *Int. Polym. Proc.*, **21**, 473 (2006).
9. K. Mönkkönen, J. Hietala, P. Paakkonen, E.J. Paakkonen, T. Kaikuranta, T.T. Pakkanen and T. Jaaskelainen, *Polym. Eng. Sci.*, **42**, 1600 (2002).
10. U. Theilade and H. Hansen, *Int. J. Adv. Manuf. Tech.*, **33**, 157 (2007).
11. M. Yoshii, H. Kuramoto and K. Kato, *Polym. Eng. Sci.*, **34**, 1211 (1994).
12. V. Kalima, J. Pietarinen, S. Siitonen, J. Immonen, M. Suvanto, M. Kuittinen, K. Mönkkönen and T.T. Pakkanen, *Opt. Mater.*, **30**, 285 (2007).
13. O. Murakami, M. Kotaki and H. Hamada, *Polym. Eng. Sci.*, **48**, 697 (2008).
14. U.R. Arlø and E.M. Kjær, "Transcription of small surface structures in injection molding - An experimental study" in *Specialized molding techniques*, Ed. H.-P. Heim and H. Potente, Plastics Design Library, (2001).
15. S. Aasetre and E. Andreassen, *Plast. Rubber Compos.*, **31**, 20 (2002).
16. D. Chen, U.S. Patent 7605925-B1, (2009).
17. T. Nguyen-Chung and G. Mennig, *Plast. Rubber Compos.*, **35**, 418 (2006).
18. W.F. Zoetelief, L.F.A. Douven and A.J.I. Housz, *Polym. Eng. Sci.*, **36**, 1886 (1996).
19. H.T. Pham, C.P. Bosnyak and K. Sehanobish, *Polym. Eng. Sci.*, **33**, 1634 (1993).
20. R.P. Kambour, J.C. Caraher, R.C. Schnoor, M.L. Todt, H.P. Wang and S.J. Willey, *Polym. Eng. Sci.*, **36**, 2863 (1996).
21. K.M.B. Jansen, J.J.W. Orij, C.Z. Meijer and D.J. Van Dijk, *Polym. Eng. Sci.*, **39**, 2030 (1999).
22. B. Carpenter, S. Patil, R. Hoffman, B. Lilly and J. Castro, *Polym. Eng. Sci.*, **46**, 844 (2006).
23. J.H. Li and W.B. Young, *Int. Polym. Proc.*, **24**, 421 (2009).
24. Y. Ding, H.W. Ro, T.A. Germer, J.F. Douglas, B.C. Okerberg, A. Karim and C.L. Soles, *ACS Nano*, **1**, 84 (2007).